EBN SCAN Rotliegend Legacy Core Study

SUMMARY REPORT

Project: 2200158-01

January 2025

EBN SCAN Rotliegend Legacy Core Study – Summary Report

Authors

Frans de Reuver
Saturnina Henares Ladron de Guevara
Andrea Sorci
Dallyn Rodrigues
Erich Funk

Reviewed by

Erich Funk

Release authorised by: Marcel Zwaan

Manager Subsurface and Engineering

Prepared for:

EBN BV
Daalsesingel 1
3511 SV Utrecht
The Netherlands

Prepared by:

PanTerra Geoconsultants B.V.
Weversbaan 1-3
2352 BZ Leiderdorp
The Netherlands
T +31 (0)71 581 35 05
info@panterra.nl

Executive Summary

This report describes the work performed by PanTerra Geoconsultants B.V. for the EBN Rotliegend Legacy Core Study (contract no. GTO 22-T35-DR10), which is executed as part of the broader SCAN Geothermal Research Project. The SCAN Project, undertaken by EBN and financed by the Dutch Ministry of Climate and Green Growth, aims to enhance the understanding of geothermal potential in the Netherlands. SCAN's areas of interest include 'blank' zones with limited subsurface data where exploration for hydrocarbons has been minimal.

Cores are analysed from 34 onshore legacy wells drilled between 1950 and 2012 in the central part of The Netherlands. Approximately 900 meters of cores with individual core lengths ranging from 3m to 167m recovered from the Slochteren Formation (Upper Rotliegend Group) were analysed. The cores were sedimentologically described and sampled for petrographic analysis at the core storage facilities of TNO (Zeist) and the Nederlandse Aardolie Maatschappij (NAM, Assen). For each well, the core descriptions, petrographic analyses and legacy routine core analysis data (RCA) were integrated to determine the controls of sedimentary facies and detrital mineralogy and diagenesis on the reservoir quality of the Slochteren sandstone reservoir. The results were documented in 34 individual well reports available through the TNO NLOG website.

This summary report provides a detailed description of the data inventory and methodologies, and discusses the main observations and general conclusions compiled from the individual well studies. It does not provide a full, comprehensive regional integration of all findings.

The main findings of the project can be summarised as follows:

The cores predominantly comprise continuous sandstone sections mostly reflecting "dry" aeolian settings such as Dry Aeolian Sandflat/Interdune, Aeolian Dune Base and Aeolian Dune Slip Face depositional sub-environments. These are rarely intercalated with thin Damp Aeolian Sandflat deposits. Fluvial deposits are generally rare and have been encountered mostly at the base of the Slochteren Formation directly overlying the Base Permian Unconformity. The maximum observed thickness in core is ca. 15m, although in one case, a thickness of ca. 40m thick is reported (composite log in well DSP-02).

Thin-section analysis shows that detrital mineralogy is dominated by quartz and minor to moderate amounts of sedimentary, metamorphic, and plutonic rock fragments. Potassium feldspar and plagioclase are less common, in part due to alteration and/or dissolution. Most samples are classified as sublitharenites.

Diagenesis involved a variable suite of grain alteration/dissolution. Cementation by blocky cements (quartz, dolomite, anhydrite, siderite) and clay minerals (kaolinite and various habits of illite), was driven by complex burial histories with several phases of subsidence and uplift that varied between different structural provinces that covers the study area. The Slochteren formation was buried deepest (in the order of 3000m TVD) in the West Netherlands Basin (5 wells), resulting in strong compaction and cementation, followed by Late Cretaceous inversion and uplift. Reservoir quality is low in wells from this area. The Central Netherlands Basin containing the majority of wells (25 out of 34) may have shown more variation in burial depths as reservoir quality is variable. The northern edge of the Central Netherlands Basin, platform areas such as the North Holland, Friesland and Groningen Platforms and the Texel IJsselmeer High likely experienced the least amount of burial, with many wells currently at their deepest burial at 2000m TVD or less. Highest reservoir quality can be found in these areas with mean core porosities of 15-27% and mean permeabilities in the range of 10mD to 1Darcy.

Index of Figures

Index of Tables

Contents

1 Introduction

1.1 General

This summary report is part of the deliverables related to the execution of the Rotliegend Legacy Core Study performed under contract GTO 22-T35-DR10 – Provision of Core Analysis Services as part of the EBN SCAN Geothermal Project. The summary report describes in detail the data inventory, the applied methods, and some general conclusions about the results of individual well studies. Separate reports are written for each of the 34 wells, describing the results of the various analyses performed and including an assessment of the controls on reservoir quality. These individual well reports can be found on the NLOG Datacenter/Gegevenstypen/Boringen web page[1] of the TNO NLOG website under the tab "Documenten".

The SCAN program, executed by EBN and funded by the Dutch Ministry of Climate and Green Growth, aims to collect new subsurface data and reprocess existing data to stimulate and accelerate the use of geothermal energy in the Netherlands. The SCAN program focuses on areas where no hydrocarbons have been found and, because of this, were less and less attractive for oil and gas companies to drill exploration wells. As a result, limited well data is available in these parts of The Netherlands. This lack of well data hampers the development of geothermal projects, making developing such projects more risky.

Reservoir cores are an important source of descriptive and quantitative information in estimating areas and volumes of geothermal potential. In general, porosity and permeability data are available from released legacy wells; however, good geological descriptions and diagenetic studies are rarely available from wells in the SCAN areas on the NLOG data repository.

To improve the use of the existing legacy cores and to make this resource better accessible, EBN initiated a project to study the Rotliegend sandstone reservoir (Slochteren Formation) in the central part of the Netherlands. In this area, 34 legacy wells were selected, all having a cored section of the Rotliegend reservoir. These wells were drilled between 1950 and 2012 and have a total cored section of approximately 900m in the Rotliegend. The main objective of this study was to assess the depositional and diagenetic controls on reservoir quality, which varies quite strongly throughout the study area. This study will support efforts to develop geothermal resources for and with parties involved in those areas.

[1] https://www.nlog.nl/datacenter/brh-overview

1.2 Geological Setting

The Slochteren Formation is of Permian age and was deposited on the southern edge of the Southern Permian Basin, which was an elongate, E - W trending basin. It extended from the UK well into eastern Poland (see Figure 1-1, A). In the study area, it unconformably overlies deposits of the Carboniferous Limburg Group. It is conformably overlain by a thin dark shale named the Copper Shale (Kupferschiefer), forming the base of a locally thick succession of Permian Zechstein deposits. This shale was deposited after a rapid transgression that flooded the Southern Permian Basin, which had subsided well below global sea level.

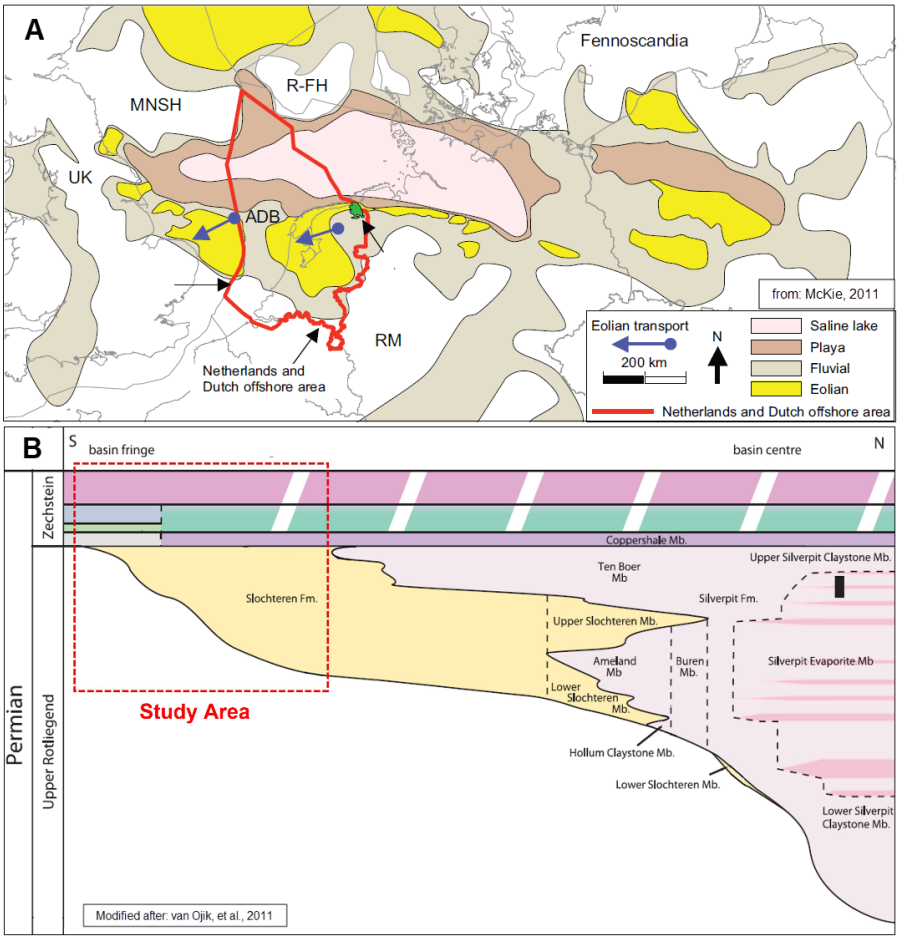

Figure 1-1 **A. Generalised map of the Southern Permian Basin. The red outline represents the acreage of The Netherlands. The yellow and tan colours indicate areas where deposits are predominantly aeolian (yellow) or fluvial. B. Schematic south-to-north cross-section of the Slochteren Formation, with sandstone-dominated deposits in the south becoming intercalated with mudstone-dominated intervals going northward. The basin's centre (and deepest) part comprises evaporitic mudstones intercalated with halite beds (Silverpit Formation).**

In the study area (red dashed rectangle in Figure 1-1, B), the Slochteren Formation predominantly consists of a generally thick, continuous sandstone sequence that is present in a large part of the Dutch onshore and offshore subsurface. After the discovery of the giant Groningen gas field in 1959, it became a target of extensive exploration for and development of natural gas. However, most wells included in this study did not find commercial quantities of gas (the locations of study wells are shown in Figure 1-2).

The thickness of the Slochteren Formation in the study wells ranges from a few meters to well over 200m. It may locally be thinning to absent due to pinch-out against basin highs or Late-Jurassic/Early Cretaceous erosion (e.g., Texel-IJsselmeer High). While highly variable, mean porosities and permeabilities in the study wells may reach up to 27% and 1032mD, respectively, making it an interesting target for geothermal heat extraction.

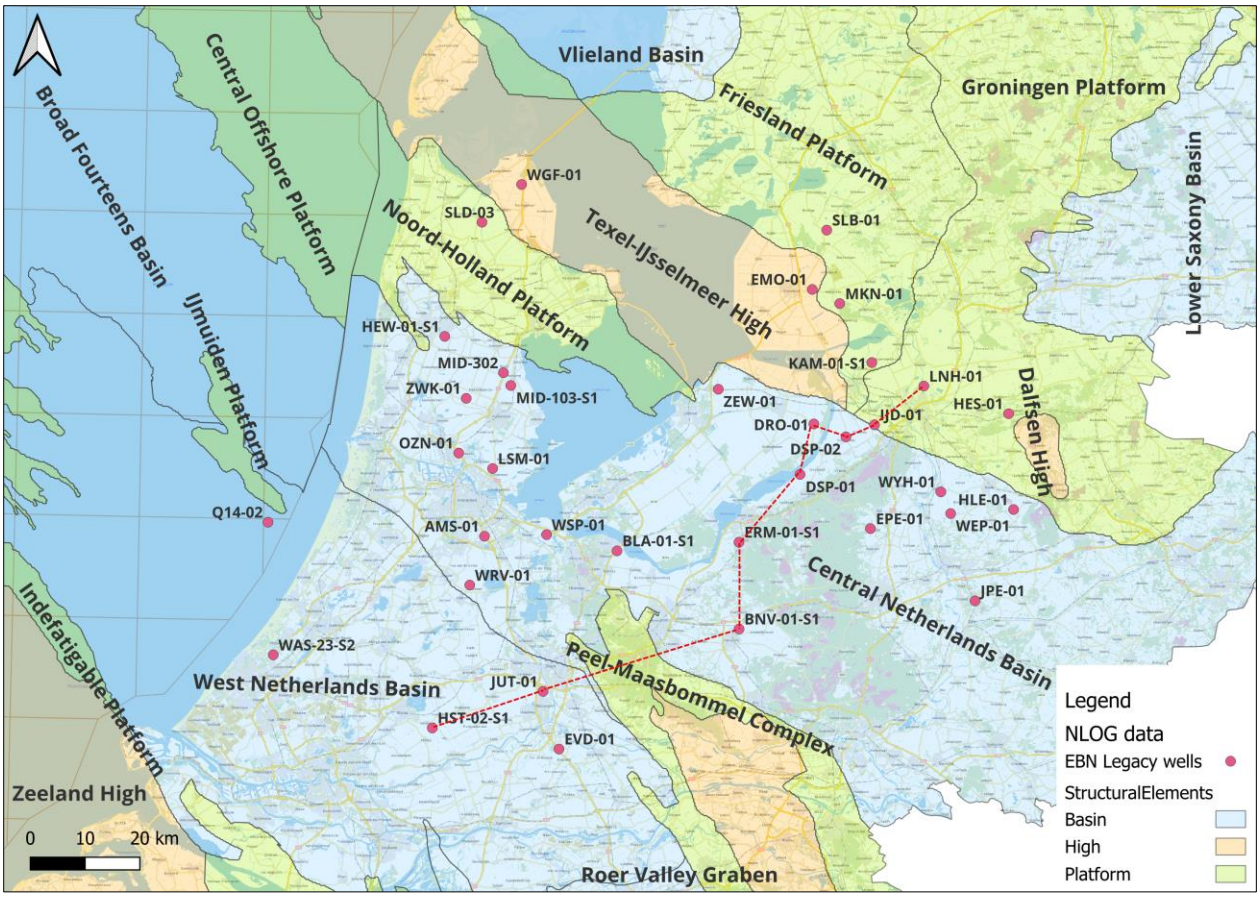

Figure 1-2 **Map showing the study wells (red dots) with structural elements in the Dutch subsurface. The dashed red line represents the cross-section shown in Figure 1-3, created with the DGMdeep v.5.0 subsurface model[2] of TNO. Map modified from (Kombrink et al., 2012). The 2023 SCAN research well AMS-01 is shown on the map for reference but is not part of this study.**

The structural development of the Dutch subsurface is complex. Several phases of rifting and compression have strongly faulted the Slochteren Formation. An Alpine phase of compression caused the inversion (uplift) of the West Netherlands and Central Netherlands Basins (light blue coloured areas in Figure 1-2) while other areas (platforms – light green areas) experienced more limited subsidence and uplift.

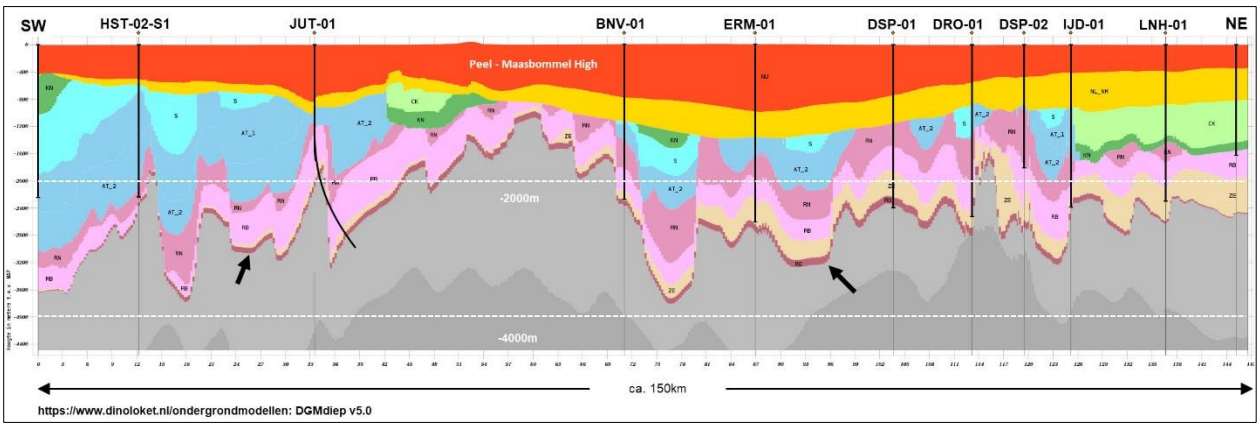

Figure 1-3 **SW – NE cross-section generated with the DGMdeep v5.0 subsurface model of TNO incorporating several Legacy Core Study wells, showing the complex structure of the subsurface in the study area. Black arrows point to the Slochteren Formation (in dark red).**

[2] https://www.dinoloket.nl/ondergrondmodellen: DGMdiep v5.0

Figure 1-3 illustrates the complex structural development that affected the Slochteren Formation, indicating that its burial history must have varied significantly from area to area. This undoubtedly impacted the diagenetic development and the resulting reservoir properties (porosity and permeability). Figure 1-4 shows examples of burial curves from 3 wells in different structural provinces. The first two curves (Friesland Platform and Texel-IJsselmeer High) show that significant uplift occurred towards the end of the Jurassic (blue-coloured interval on Figure 1-4), while Late Cretaceous uplift was relatively insignificant. In contrast, well WGF-01, located on the Texel IJsselmeer High, shows that the Slochteren Formation is partially eroded at the time of the major uplift as it is directly overlain by the Vlieland Claystone Formation. The diagram for Well PKP-01 (bottom) indicates that inversion at the end of the Cretaceous is strong in the West Netherlands Basin, whereas the Late Jurassic Uplift is barely noticeable.

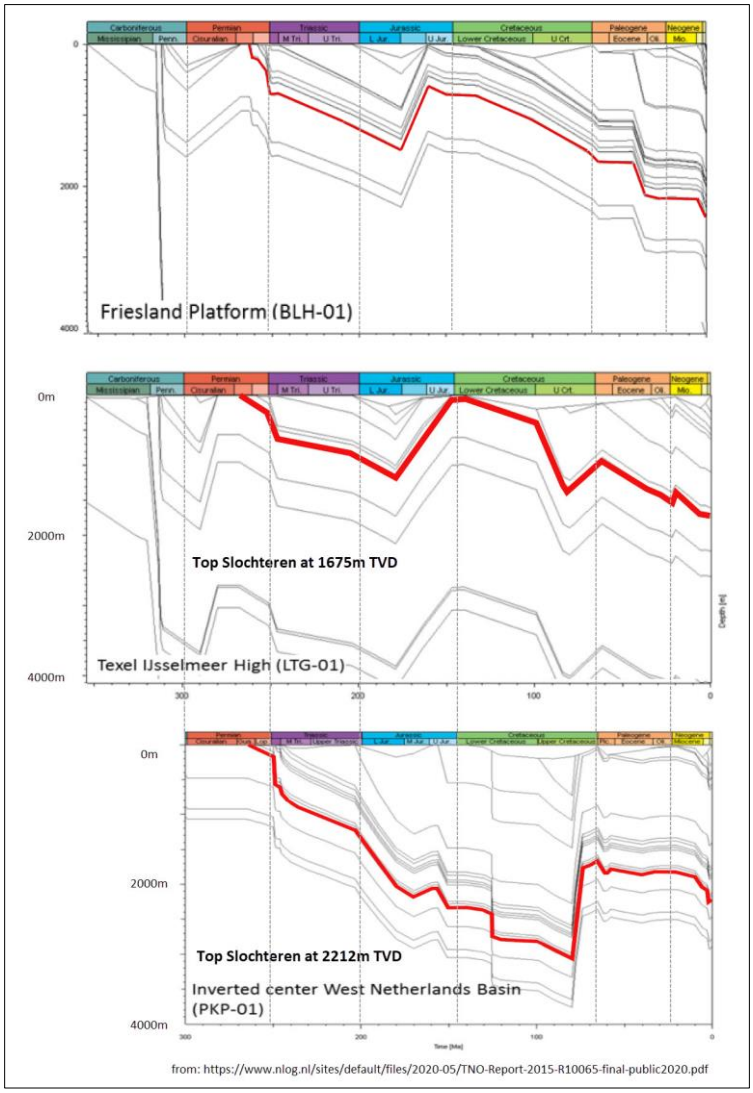

Figure 1-4 **Burial history curves[3] for the Slochteren Formation (red lines) for three different structural provinces (from TNO, 2015). The top image shows the burial path for well BLH-01 (not included in the study) on the Friesland Platform. The second curve is from well LTG-01 located on the Texel-IJsselmeer High (in nearly the same location as study well EMO-01). The lower image shows the burial path at the location of well PKP-01 (Papekop). This curve may be representative for study well HST-02 and the upthrown section of Slochteren Formation in JUT 01 (see also Figure 1-3)**

[3] https://www.nlog.nl/sites/default/files/2020-05/TNO-Report-2015-R10065-final-public2020.pdf

1.3 Data

Cores of the Upper Rotliegend Slochteren Formation from 34 wells drilled in onshore concessions between 1950 and 2012 were analysed. Approximately 900m of core was sedimentologically described, photographed, and sampled. These descriptions were conducted at TNO's core storage facilities in Zeist and the Nederlandse Aardolie Maatschappij (NAM) in Assen. The core description was followed by a petrographic analysis of 163 thin sections, an SEM and BSEM analysis of 65 samples, and an X-ray diffraction analysis (whole rock and clay fraction) of 59 samples. Lastly, 2200 pre-existing legacy routine core analysis (RCA) measurements were integrated to assess reservoir quality. Individual well reports were produced containing data, descriptions and interpretations, focusing on the controls on reservoir quality. These reports are available on the Data Center webpage on the TNO NLOG website (Home / Datacenter / Gegevenstypen / Boringen) under the respective well web pages. A detailed summary of core lengths and the number of samples per well is presented in Table 1-1.

No.	Well	Described Core Length (m)	Number of Samples					
			Thin sections		Electron Microscopy		XRD	RCA
			Photo-micrographs	Point Count	SEM	BSEM		
1	ZEW-01	18.0	4	4	-	1	-	59
2	BLA-01-S1	9.0	3	3	-	1	-	37
3	WEP-01	7.6	4	4	1	1	1	20
4	JPE-01	14.4	5	5	1	1	2	4
5	WSP-01	8.1	1	1	-	1	-	-
6	WRV-01	3.0	1	1	1	1	1	-
7	DRO-01	44.9	9	9	1	1	2	142
8	EMO-01	24.4	7	7	1	1	2	-
9	WGF-01	14.3	6	6	1	1	2	50
10	KAM-01-S1	16.4	5	5	1	1	2	54
11	EPE-01	3.8	1	1	1	1	1	9
12	SLD-03	22.7	3	3	1	1	2	90
13	IJD-01	17.9	6	6	1	1	2	72
14	BNV-01-S1	3.3	1	1	-	1	-	-
15	LSM-01	15.6	2	2	1	1	1	54
16	OZN-01	13.6	5	5	1	1	2	14
17	EVD-01	61.4	11	11	3	2	6	116
18	JUT-01	18.0	5	5	1	1	3	60
19	ZWK-01	26.3	5	5	1	-	1	106
20	HEW-01-S1	155.6	10	10	1	1	3	280
21	MID-302	28	4	4	1	1	1	87
22	MID-103-S1	72.8	8	8	2	1	2	173
23	HES-01	2.6	1	1	1	1	1	-
24	WYH-01	41.8	13	13	2	1	5	150
25	LNH-01	5.0	3	3	1	1	2	17
26	HLE-01	21.6	6	6	1	1	3	75
27	MKN-01	11.6	3	3	1	1	2	39
28	SLB-01	12.3	4	4	1	1	2	41
29	ERM-01-S1	7.0	2	2	1	1	1	24
30	DSP-02	4.3	-	-	-	-	-	-
31	Q14-02	33.1	3	3	1	1	2	146
32	HST-02-S1	13.0	4	4	-	1	1	44
33	WAS-23-S2	37.9	7	7	1	1	1	126
34	DSP-01	115.1	11	11	1	1	3	111
	Total:	904.4	163	163	32	33	59	2200

Table 1-1: Overview of the different data types used in the study per well detailing described core lengths and number of samples utilized by each analytical method.

Additionally, Figure 1-5 provides a graphical representation of the true vertical thickness (TVT) of the Slochteren Formation intersected by the wells as grey bars and the positions of the described cores as

yellow bars. Due to the limited coverage in many wells, the cores may not be fully representative of the full Slochteren Formation interval in each well.

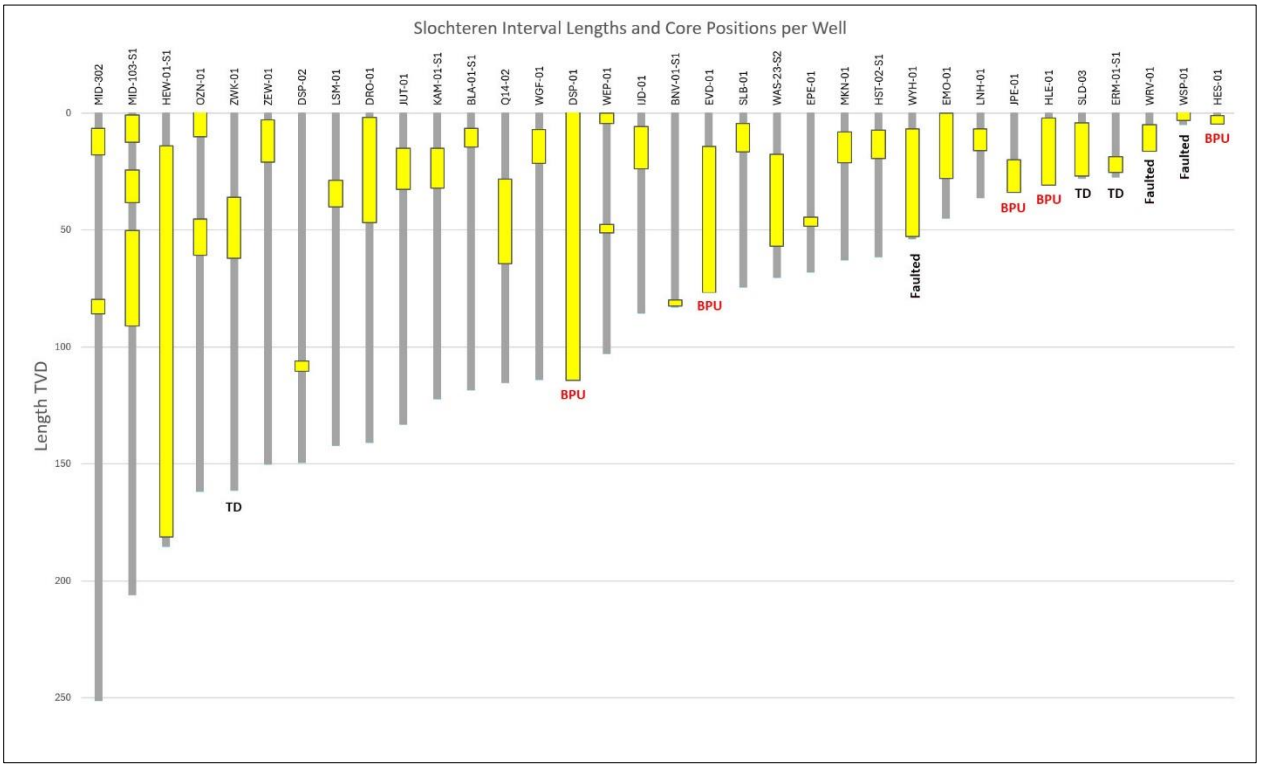

Figure 1-5: **Graphical representation of the thickness of the Slochteren Formation intersected in each well in true vertical thickness (grey bars) and the positions of cored intervals (yellow bars) available to this study. The wells are arranged from left to right in order of decreasing formation thickness. Wells that do not fully penetrate the Slochteren Fm. are marked with "TD" below the respective well. Wells with cores that penetrated the Base Permian Unconformity (BPU) are labelled "BPU." Lastly, wells with cores intersecting faults within the Slochteren interval are identified with "Faulted" below the well.**

1.4 Summary Table

A summary table was compiled for comparison of the main attributes of the Slochteren Formation in the analysed wells. Extractions of the full table are presented in Table 1-3, Table 1-4; the table itself is a separate deliverable in Excel format. The table reflects well-information, core- and formation-specific information combined with averaged values of petrographic attributes and routine core analysis data. The sources include publicly available datasets (e.g., nlog.nl) alongside data from the individual well reports in this project. Figure 1-6 shows a breakdown of attributes included in the summary table. A few items need to be described in more detail:

- TD within Slochteren Formation: TD of the well in case it occurs within the Slochteren Formation
- Described core length (m excl. core gaps): The net length of core described excluding gaps within the cores due to missing sections (e.g., due to missing whole core preserved samples or rubbly sections not preserved as resinated core slabs)
- Base Permian Unconformity occurrence in core: depth (AH) of the BPU if present in the core
- Horizontal permeability St. Dev.: ±1 standard deviation calculated on log 2 permeabilities and raised to the power of 2.

Well	Numeric order in study
	Name
	Studied cored succession(s)
	Coordinates (surface location, WGS84 format)
	Structural basin
	Close proximity to fault
	Well deviation at cored Interval

Formation	Name
	Top (along hole & true vertical depth)
	Base (along hole & true vertical depth)
	Thickness (along hole & true vertical depth)
	TD within the Slochteren Fm.
	Formation above the Slochteren Fm.
	Group directly underlying the Slochteren Fm.
	Reservoir fluid
	Gas-Water contact (TVD, if observed)

Core	Core storage location
	Condition of described core material
	Described core length (m, excl. gaps)
	Core depth top (along hole & true vertical depth)
	Core Depth Bottom (along hole & true vertical depth)
	Thickness (along hole & true vertical depth)
	Core gaps in described core
	Core-to-Log shift (m)
	Base Permian Unconformity occurrence in core

Routine Core Analysis	Total plug no of studied succession
	He-porosity mean
	He-porosity st. dev.
	Hor. permeability mean incl +/- st. dev.
	Hor. permeability st. dev.
	Grain density

RQ – Petrography	No. of samples
	Degree of Compaction (expressed via grain contacts)
	Compaction porosity loss
	Primary Intergranular Pores
	Oversized pores
	Secondary intragranular pores
	Total point-counted porosity
	Micro-porosity (He-porosity - Point counted porosity)
	Total pore-filling cements
	Dominant pore-filling cements type
	Content of the dominant pore-filling cements
	Detrimental diagenetic processes or minerals
	Beneficial diagenetic processes or minerals

Fractures Score Card (1-5)	Small-scale faults
	Deformation bands
	Fractures cemented
	Fractures partially cemented
	Conjugate cemented fractures

Figure 1-6: Pictorial representation of attributes captured in the Summary Table.

Abbreviation Legend	
ROSL	Slochteren Formation
AH	Along Hole Depth
TVD	True Vertical Depth
GWC	Gas-Water Contact
TNO	Nederlandse Organisatie voor Toegepast Natuurwetenschappelijk Onderzoek - Dutch Organization for Applied Scientific Research
NAM	Nederlandse Aardolie Maatschappij
BPU	Base Permian Unconformity
n	Number of Samples measured/analysed
St. Dev.	Standard Deviation
n.m.	Not Measured
N/A	Not Applicable
Grain contacts	P = Point, L = Long, CC = Concavo-convex, S = Sutured, Sty = Stylolised
COPL	Compactional Porosity Loss

Table 1-2 Legend of the abbreviations used in the Summary Table.

Well Related Information				Formation data							Core Sampling						Routine Core Analysis							Fractures Score Card				
Report No.	Well Name[1]	Well Deviation at Cored Interval	Close Proximity to Fault	Top AH (m)	Bottom AH (m)	Thickness AH (m)	TD (m AH) within ROSL	Formation above ROSL	Reservoir fluid	GWC (TVD)	Described Core length (m, excl. gaps)	Core-to-Log shift (m) (+ = down)	Core Depth AH (m)			BPU present in Core	n	He-Porosity (%)		Horizontal Permeability (mD)			Grain Density (g/cc)	SF	DB	FC	FPC	CCF
													top	bottom	Thickness (inc. gaps)			Mean	st. dev.	Mean	-1 st. dev.	+1 st. dev.	Mean					
1	ZEW-01	Vertical		1617.0	1768.0	151.0		Kupferschiefer	Brine		18.00		1620.0	1638.0	18.00		59	25.2	3.3	679	190	2427	2.65	1	1	2	-	-
2	BLA-01-S1	28°/112°		1503.0	1642.0	139.0		Z1 Lower Claystone, Faulted	Gas shows		9.00		1511.0	1520.0	9.00		37	19.0	0.8	119	68.5	206	2.72	-	-	-	-	-
3.1	WEP-01.1	1.8°/164°		1544.0	1647.0	103.0		Kupferschiefer	Brine		4.40		1544.0	1548.4	4.40		12	14.9	1.7	25.6	7.24	90.4	2.64	1	-	2	-	-
3.2	WEP-01.2	a/a									3.20		1592.0	1595.2	3.20		8	21.9	2.7	121	10.3	1409	2.63	-	-	-	-	-
4	JPE-01	16.7°/127.4°		880.0	914.0	34.0		Kupferschiefer			14.30	-1.4	901.0	915.4	14.40	BPU	4	14.6	N/A	0.32	N/A	N/A	2.66	-	-	1	-	-
5	WSP-01	3.7°/ 308°	Yes, SCAN-line 25	2192.0	2197.0	5.0		Z1 Lower Claystone, Faulted	Brine		8.10	+2.3	2187.0	2195.1	8.10		n.m.							5	-	3	-	-
6	WRV-01	7°/50°	Yes	2340.5	2351.5	11.0		Z1 Lower Claystone, Faulted	Brine		3.00		2345.5	2357.0	3.00		n.m.							2	-	-	-	-
7	DRO-01	Vertical	Yes	2189.0	2330.0	141.0		Kupferschiefer	Brine		44.90		2191.0	2235.9	44.90		142	11.9	3.3	1.39	0.24	8.02	2.67	2	-	1	2	2
8	EMO-01	Vertical		1679.5	1724.5	45.0		Upper Holland Marl[2]	Brine		28.00		1679.5	1707.5	28.00		n.m.							-	4	-	2	-
9	WGF-01	Vertical		2260.0	2374.0	114.0		Vlieland Claystone[2]	Brine		14.35		2267.0	2281.4	14.35		50	20.6	2.7	46.0	5.21	406	2.63	-	-	1	2	-
10	KAM-01-S1	Vertical		1795.0	1917.5	122.5		Kupferschiefer	Gas shows		16.40		1810.9	1827.3	16.40		54	16.0	2.1	6.55	2.44	17.6	n.m.	3	2	3	-	-
11	EPE-01	Vertical		1768.5	1837.0	68.5		Kupferschiefer	Brine		3.80		1813.0	1816.8	3.80		9	10.7	N/A	1.64	N/A	N/A	n.m.	-	-	1	-	-
12	SLD-03	4.1°/029°		2016.0	2044.0	28.0	2044.0	Kupferschiefer	Brine		22.40		2020.0	2042.7	22.70		90	26.7	3.7	99.3	24.4	404	2.71	-	1	2	-	-
13	IJD-01	5.25°/272°		2262.0	2348.0	86.0		Kupferschiefer	Brine		17.90		2268.0	2285.9	17.90		72	14.7	2.6	31.0	5.52	174	2.65	2	3	2	-	1
14	BNV-01-S1	34.7°/ 275°		2942.0	3043.0	101.0		Kupferschiefer	Brine		3.30	-1.6	3039.0	3042.3	3.30		n.m.							3	2	1	-	-
15	LSM-01	43°/286°		1454.0	1650.0	196.0		Kupferschiefer	Brine		15.30	-2.9	1494.0	1509.6	15.60		54	17.4	3.4	0.67	0.31	1.42	2.67	-	-	1	1	-
16	OZN-01	Vertical		1310.0	1472.0	162.0		Kupferschiefer	Brine		13.60		1307.1	1370.7	63.60		14	12.9	2.9	2.57	0.56	11.8	2.68	1	1	1	3	-
17	EVD-01	9°/010°		1788.0	1866.0	78.0		Z1 Fringe Carbonate	Brine		61.40		1802.4	1863.8	61.44	BPU	116	11.0	3.3	3.18	1.70	36.1	2.67	2	-	2	4	-
18	JUT-01	17°/007°	Yes; no fractures in core	3240.0	3378.0	138.0		Z1 Fringe Carbonate	Brine		18.00	+3.9	3256.0	3274.0	18.00		60	10.2	2.5	0.43	0.15	1.20	2.68	1	-	1	2	-
19	ZWK-01	4°/151°		3139.0	3300.0	161.0	3300.0	Zechstein Group	Gas		26.30	+0.7	3174.0	3200.3	26.25		106	4.2	3.0	0.05	0.04	0.08	2.72	5	4	3	-	2
20	HEW-01-S1	5°/045°		1994.0	2180.0	186.0		Kupferschiefer	Brine		155.60		2008.0	2175.6	167.60		280	16.4	4.0	13.7	4.34	185	2.67	5	5	4	5	2
21.1	MID-302.1	51°/286°		3484.0	3871.0	387.0		Kupferschiefer	Gas	-2435.0	18.00		3494.0	3512.0	17.98		60	13.1	2.3	0.33	0.13	0.86	2.67	3	3	3	-	2
21.2	MID-302.2	a/a									9.90		3608.0	3617.9	10.00		27	20.9	3.4	8.52	2.40	30.2	2.67	-	-	-	-	-
22.1	MID-103-S1.1	25°/113°		2568.0	2796.0	228.0		Kupferschiefer	Gas	-2500.0	12.60		2569.0	2581.6	12.60		43	15.6	2.6	19.3	3.37	110	2.65	2	1	2	1	-
22.2	MID-103-S1.2	a/a									9.90		2595.0	2610.1	15.10		41	19.7	2.1	158	67.2	370	2.66	-	-	-	-	-
22.3	MID-103-S1.3	a/a									21.00		2623.0	2668.1	45.10		89	22.1	4.1	602	194	1869	2.66	-	-	-	-	-
23	HES-01	Vertical		2101.0	2104.0	3.0		Kupferschiefer	Brine		2.27		2102.2	2105.8	3.60	BPU	n.m.							3	-	1	-	-
24	WYH-01	Vertical		1713.0	1767.0	54.0		Z1 Lower Anhydrite	Brine		41.80		1720.0	1765.9	45.90		150	14.3	3.9	36.2	5.79	226	2.66	4	4	4	3	4
25	LNH-01	28°/358°		2288.0	2329.0	41.0		Kupferschiefer	Brine		4.95		2295.5	2306.2	10.65		17	18.8	1.9	1032	504	2114	2.66	-	-	1	-	-
26	HLE-01	4.5°/012°		1420.0	1451.0	31.0		Kupferschiefer	Brine		22.80	+3.1	1422.5	1451.4	28.90	BPU	75	22.3	3.6	464	162	1289	2.66	3	4	3	2	-
27	MKN-01	Vertical		1686.0	1749.0	63.0		Kupferschiefer	Gas		11.60		1695.0	1708.0	13.00		39	23.8	1.9	395	149	1050	2.65	2	-	2	-	-
28	SLB-01	1.4°/016°		2005.0	2080.0	75.0		Kupferschiefer	Gas		12.28		2010.0	2022.3	12.28		41	18.1	4.7	139	42.5	453	2.65	-	2	2	-	-
29	ERM-01-S1	15°/128°		2621.0	2649.5	28.5	2649.5	Kupferschiefer	Brine		7.00		2640.5	2647.5	7.00		24	3.4	0.7	0.01	N/A	N/A	2.68	-	1	1	-	-
30	DSP-02	10°/224°		1660.0	1812.0	152.0		Kupferschiefer	Brine		4.30		1768.0	1772.3	4.30		n.m.							-	-	-	1	-
31	Q14-02	1.4°/110°		2889.0	3004.5	115.5		Kupferschiefer (edge)	Gas shows		33.12		2917.0	2953.3	36.28		146	8.8	1.0	0.50	0.23	1.09	2.66	-	1	2	-	1
32	HST-02-S1	23°/048°		2384.0	2450.0	66.0		ZE Upper Claystone	Gas		13.00		2392.0	2405.0	12.96		44	8.0	1.0	1.12	0.94	1.33	2.69	-	-	-	2	-
33	WAS-23-S2	12°/211°		2993.0	3065.0	72.0		ZE Upper Claystone	Gas		37.90		3011.0	3051.1	40.13		126	8.8	2.2	0.66	0.11	3.91	2.66	1	-	1	-	-
34	DSP-01	1°/224°		2262.0	2376.0	114.0		Kupferschiefer	Brine		111.70		2260.5	2376.3	114.50	BPU	111	9.0	3.5	1.18	0.48	2.90	2.66	5	2	3	-	-

[1] wells WEP-01, MID-302, MID-103 subdivided. Reservoir quality is significantly different per zone

= top of core just below top Slochteren Fm

= Slochteren very thin; Faulted-out

[2] top Slochteren Fm. eroded

SF = Small Fracture, DB = Deformation Band
FC = Cemented Fractures
FPC = Partially-cemented Fractures
CCF = Conjugate Cemented Fractures

Table 1-3 **Extraction of selected columns of the Summary Table continued in Table 1-4. The Summary Table is provided as a separate deliverable (Excel file). This table comprises more extensive information on Well-related Data, Formation Data, Core Sampling and Petrography & Reservoir Quality. See also Table 1-4Table 2-4 for a summary of reservoir quality data, quantities of main intergranular pore-filling cements and pore types from point-counting.**

Well Related Information		Formation Data		Core Sampling			Routine Core Analysis				Reservoir Quality- Petrography												
Report No.	Well Name[1]	Top AH (m)	Thickness AH (m)	Described Core length (m, excl. gaps)	Core Depth AH (m)		n	Mean He-Porosity (%)	Mean Hor. Permeability (mD)	Mean Grain Density (g/cc)	No. of samples	Compaction (Grain contacts)	COPL (%)	Intergranular Primary Pores (%)	Oversized Pores (%)	Intragranular Secondary Pores (%)	Sum Point-counted Porosity (%)	He-Porosity (%)	Micro-Porosity %	Total Pore-Filling Cements (%)	Dominant Pore-Filling Cement(s)	Content of the Dominant Pore-Filling Cement(s) (%)	Dominant Control(s) on Permeablity	
					top	Length (inc. gaps)																	Detrimental	Beneficial
1	ZEW-01	1617.0	151.0	18.00	1620.0	18.0	59	25.2	679	2.65	4	P-L	26.5	9.5	1.7	4.6	15.7	26.7	11.0	15.6	Fe-dolomite	7.0	Grain-rimming Fe-dolomite	Grain-dissolution
2	BLA-01-S1	1503.0	139.0	9.00	1511.0	9.0	37	19.0	119	2.72	3	P-L	28.4	9.9	0.9	2.3	13.1	18.8	5.7	12.3	Quartz	5.3		Primary pore preservation
3	WEP-01.1	1544.0	103.0	4.40	1544.0	4.4	12	14.9	25.6	2.64	2	L-CC	28.0	6.2	0.5	5.8	12.5	14.6	2.1	17.4	Fe-dolomite, quartz	10.0, 4.7	Fe-dolomite	**Grain dissolution**
3	WEP-01.2	1544.0	103.0	3.20	1592.0	3.2	8	21.9	121	2.63	2	L-CC	30.4	6.7	1.8	9.5	18.0	21.8	3.8	14.3	Grain-rimming illite, anhydrite, quartz	4.8, 3.7, 3.3	Pore-filling cements, (Illite?)	**Grain dissolution**
4	JPE-01	880.0	34.0	14.30	901.0	14.4	4	14.6	0.32	2.66	5	L-CC, (S)	31.0	5.7	0.1	3.9	9.7	14.5	4.8	14.5	Pore-filling & grain-rimming illite, Fe-dolomite	6.1, 3.4	Compaction, **pore-filling & grain-rimm. illite**	(Grain dissolution)
5	WSP-01	2192.0	5.0	8.10	2187.0	8.1	n.m.	0.0	0.00	0.00	1	fault	35.0	1.1	-	2.5	3.5	n.m.	n/a	14.4	Grain-rimming illite, quartz	6.7, 5.6	**Cataclasis, grain-rimming illite**, quartz cement	
6	WRV-01	2340.5	11.0	3.00	2345.5	3.0	n.m.	0.0	0.00	0.00	1	L-Sty	34.3	2.0	-	-	2.0	n.m.	n/a	14.3	Fe-dolomite, grain-rimming illite	6.0, 4.7	**Compaction**, grain-rimming illite	
7	DRO-01	2189.0	141.0	44.90	2191.0	44.9	142	11.9	1.39	2.67	9	L-(CC)	30.0	3.6	-	3.5	7.0	11.0	4.0	15.5	Quartz, kaolinite, Fe-dolomite	5.7, 4.7, 3.6	**Compaction**, pore-filling cements	(Grain dissolution)
8	EMO-01	1679.5	45.0	28.00	1679.5	28.0	n.m.	0.0	0.00	0.00	7	P-L/L-CC	28.6	8.2	-	4.3	12.6	n.m.	-	10.6	Fe-dolomite	7.8	(Compaction), Fe-dolomite cmt.	Primary pore preservation, **grain dissol'n**
9	WGF-01	2260.0	114.0	14.35	2267.0	14.3	50	20.6	46.0	2.63	6	P-L	33.7	6.7	0.1	6.7	13.6	20.1	6.6	10.3	Kaolinite	5.2	Kaolinite	**Grain dissolution**
10	KAM-01-S1	1795.0	122.5	16.40	1810.9	16.4	54	16.0	6.55	n.m.	5	P	29.6	3.0	-	6.3	9.3	16.1	6.8	15.7	Fe-dolomite, Anhydrite, Kaolinite	5.5, 4.3, 3.5	Pore-filling cements	**Grain dissolution**
11	EPE-01	1768.5	68.5	3.80	1813.0	3.8	9	10.7	1.64	n.m.	1	L-Sty	32.4	3.0	-	2.7	5.7	n.m.	n/a	15.7	Grain-rimming illite	12.0	Compaction, **grain-rimming illite**	
12	SLD-03	2016.0	28.0	22.40	2020.0	22.7	90	26.7	99.3	2.71	3	P-L	30.6	7.2	-	6.0	13.2	20.5	7.3	12.0	Fe-dolomite	8.8	Grain-rimming Fe-dolomite	**Grain dissolution**
13	IJD-01	2262.0	86.0	17.90	2268.0	17.9	72	14.7	31.0	2.65	6	CC	32.8	5.9	0.3	4.4	10.7	12.7	2.1	12.3	Fe-dolomite, quartz	3.6, 3.2	Compaction & pore-filling cements	**Grain dissolution**
14	BNV-01-S1	2942.0	101.0	3.30	3039.0	3.3	n.m.	0.0	0.00	0.00	1	L-CC	28.6	1.5	-	0.8	2.3	n.m.	n/a	14.3	Anhydrite, Fe-dolomite	7.9, 4.5	Compaction, **anhydrite**, Fe-dolomite cmt.	
15	LSM-01	1454.0	196.0	15.30	1494.0	15.6	54	17.4	0.67	2.67	2	P-L	9.3	8.5	-	2.8	11.3	24.7	13.3	26.7	Pore-filling & grain-rimming illite	7.3, 4.3	**Pore-filling & grain-rimming illite**	
16	OZN-01	1310.0	162.0	13.60	1307.1	63.6	14	12.9	2.57	2.68	5	L-CC	29.0	4.5	-	2.6	7.1	13.1	6.0	17.4	Quartz, Fe-dolomite	8.5, 4.3	Compaction, quartz, Fe-dolomite cement	
17	EVD-01	1788.0	78.0	61.40	1802.4	61.4	116	11.0	3.18	2.67	11	CC, (S, Sty)	27.7	4.1	-	1.2	5.3	12.2	7.0	19.5	Pore-filling illite, quartz	4.8, 4.2	**Compaction, pore-filling illite**/kaolinite	
18	JUT-01	3240.0	138.0	18.00	3256.0	18.0	60	10.2	0.43	2.68	5	CC, S, (Sty)	24.4	5.0	0.1	1.4	6.5	8.9	2.4	15.5	Total illite, Fe-dolomite, quartz	5.2, 4.3, 4.3	**Compaction**, Fe-dolomite, quartz cement	
19	ZWK-01	3139.0	161.0	26.30	3174.0	26.3	106	4.2	0.05	2.72	5	L-CC	30.1	2.4	0.1	1.3	3.8	6.5	2.7	18.8	Anhydrite, grain-rimming illite	12.3, 5.2	(Compaction), anhydrite	
20	HEW-01-S1	1994.0	186.0	155.60	2008.0	167.6	280	16.4	13.7	2.67	10	CC	33.9	6.0	1.5	5.5	12.9	19.4	6.5	9.7	Quartz	2.3	**Compaction**	**Grain dissolution**
21	MID-302.1	3484.0	387.0	18.00	3494.0	18.0	60	13.1	0.33	2.67	1	P-L	24.3	2.7	-	2.7	5.3	9.2	3.9	24.7	Fe-dolomite., Quartz	11.7, 7.7	**Fe-dolomite**, quartz cement	
21	MID-302.2	3484.0	387.0	9.90	3608.0	10.0	27	20.9	8.52	2.67	3	P-L	26.1	13.3	0.1	4.0	17.4	20.1	2.7	10.8	Grain-rimming illite	5.3	Grain-rimming illite	
22	MID-103-S1.1	2568.0	228.0	12.60	2569.0	12.6	43	15.6	19.3	2.65	1	P-L	26.0	7.0	0.3	5.3	12.7	16.7	4.0	18.7	Quartz, Fe-dolomite	10.0, 3.0	Quartz overgrowths, Fe-dolomite	**Grain dissolution**
22	MID-103-S1.2	2568.0	228.0	9.90	2595.0	15.1	41	19.7	158	2.66	1	L	22.5	13.0	0.7	4.3	18.0	23.3	5.3	16.0	Quartz, grain-rimming illite, Fe-dolomite	5.7, 5.0, 3.7	Pore-filling cements	Grain-dissol'n, primary pore preservation
22	MID-103-S1.3	2568.0	228.0	21.00	2623.0	45.1	89	22.1	602	2.66	6	L	26.9	10.2	0.9	5.8	16.8	20.6	3.8	14.7	Grain-rimming illite, Fe-dolomite, quartz	5.2, 4.6, 4.2	Pore-filling cements	Grain-dissol'n, primary pore preservation
23	HES-01	2101.0	3.0	2.27	2102.2	3.6	n.m.	0.0	0.00	0.00	1	CC	37.3	4.7	-	0.3	5.0	n.m.	n/a	7.7	Quartz, squashed claystone rock frag's	5.7, 19.2	**Compaction** (ductile claystone rock fragments)	
24	WYH-01	1713.0	54.0	41.80	1720.0	45.9	150	14.3	36.2	2.66	13	P-L	32.6	6.7	0.5	2.4	9.6	14.9	5.2	9.4	Anhydrite, Fe-dolomite	2.5, 2.8	Compaction (from COPL)	
25	LNH-01	2288.0	41.0	4.95	2295.5	10.7	17	18.8	1032	2.66	3	P-L	32.1	8.3	1.8	2.4	12.5	17.0	4.5	8.0	Anhydrite	3.0		Low compaction and cementation
26	HLE-01	1420.0	31.0	22.80	1422.5	28.9	75	22.3	464	2.66	6	P-L	27.7	9.5	2.6	3.5	15.6	24.8	9.2	15.8	Fe-dolomite, Dawsonite	4.2, 3.2	Pore-filling cements	Grain dissolution
27	MKN-01	1686.0	63.0	11.60	1695.0	13.0	39	23.8	395	2.65	3	P-L	30.8	5.7	3.3	6.0	15.0	21.9	6.9	14.9	Fe-dolomite, Kaolinite	5.3, 5.4		**Grain dissolution**
28	SLB-01	2005.0	75.0	12.28	2010.0	12.3	41	18.1	139	2.65	4	P-L	28.1	6.5	0.6	2.9	10.0	16.6	6.6	17.0	Fe-dolomite, Anhydrite	7.8, 6.7	Pore-filling cements	
29	ERM-01-S1	2621.0	28.5	7.00	2640.5	7.0	24	3.4	0.01	2.68	2	L-S	35.5	0.3	-	1.0	1.3	3.8	2.5	16.0	Quartz, pore-filling illite, Fe-dolomite	6.7, 3.8, 3.7	**Compaction, quartz, pore-filling illite**	
30	DSP-02	1660.0	152.0	4.30	1768.0	4.3	n.m.	0.0	0.00	0.00	n.m	n/a	n/a	n/a	n/a	n/a	n/a	n.m.	n/a	n/a	n/a	n/a	n/a	n/a
31	Q14-02	2889.0	115.5	33.12	2917.0	36.3	146	8.8	0.50	2.66	3	L-CC	36.4	3.7	-	1.1	4.8	9.1	4.3	9.8	Quartz, Fe-dolomite, grain-rimming illite	2.7, 2.5, 2.3	**Compaction (COPL)**, illite	
32	HST-02-S1	2384.0	66.0	13.00	2392.0	13.0	44	8.0	1.12	2.69	4	L, CC, S	34.7	1.8	-	0.4	2.2	8.3	6.1	15.2	Fe-dolomite	9.2	**Compaction**, pore-filling Fe-dolomite	
33	WAS-23-S2	2993.0	72.0	37.90	3011.0	40.1	126	8.8	0.66	2.66	7	L, CC, S, (P)	33.5	3.9	0.1	2.5	6.5	9.0	2.4	12.9	Quartz, kaolinite	6.3, 3.8	**Compaction**, quartz & kaolinite cement	
34	DSP-01	2262.0	114.0	111.70	2260.5	114.5	111	9.0	1.18	2.66	11	L, CC, S	35.4	1.8	0.2	1.9	3.9	10.3	6.4	12.0	Quartz, pore-filling illite	5.8, 1.8	**Compaction**, quartz, pore-filling illite	

[1] wells WEP-01, MID-302, MID-103 subdivided. Reservoir quality is significantly different per zone

= top of core just below top Slochteren Fm

= Slochteren very thin; Faulted-out

F = Floating, P = Point, L = Long, CC = Concavo-Convex

S = Sutured, Sty = Stylolised

bold = relatively strong impact

() = relatively minor impact

bold = relatively strong impact

() = relatively minor impact

Table 1-4 Continuation of Table 1-3 - Extraction of selected columns of the Summary Table.

2 Analytical Results

2.1 Sedimentology

A description of the core description workflow and methods, as well as a definition of the applied lithofacies and depositional sub-environment classification schemes, can be found in Chapter 6.1 - Core Description.

The cores from the wells described in this study have very similar depositional characteristics. They are generally dominated by sandstones deposited in an aeolian setting except for relatively short intervals near the base of the Slochteren Formation. Cores from five wells contain fluvial deposits: HES-01 (3m), HLE-01 (0.4m), DSP-01 (15m), BNV-01 (1.5m), and DSP-02 (4.3m). The lengths in brackets refer to the thicknesses of the fluvial sections.

The first three wells penetrated the Base Permian Unconformity (BPU). They encountered fluvial deposits directly overlying the BPU, while in well BNV-01 an approximately 1.5m thick interval of fluvial deposits overlies a 1.2m thick interval of aeolian sandstone at the base of the core. The BPU is approximately 0.8m below the base of the core (ignoring an unknown core-to-log shift). Well HES-01 is located on a paleogeographical high (Dalfsen High, see Figure 1-2) with just 3m of Slochteren Formation deposited that is fully developed in a fluvial facies. Well HLE-01 comprises just 0.4m of fluvial (pebbly sandstone) overlying the BPU, followed by aeolian deposits. In contrast, wells DSP-01 and DSP-02 contain relatively thick successions of fluvial deposits. The wells are located at a distance of approximately 11km from each other. DSP-01 contains 15m fluvial conglomerates and (pebbly) sandstones directly overlying the BPU (c.f., Figure 2-1). Well DSP-02 recovered 4.3m of core, which consists mostly of conglomerate. The top of the core is listed in NLOG at 1772.3 (1752m TVD), while the BPU occurs at a depth of 1812m (1795.5m TVD). The lithology column in a composite log[4] of the well shows that the lower part of the Slochteren Formation contains pebbles down to the BPU. Based on the top depth of the core, the fluvial section in well DSP-02 is at least 43.2m thick.

In wells EVD-01 (central Netherlands) and JPE-01 (east Netherlands) that penetrated the BPU, the nature of the Base Slochteren cannot be determined with certainty. The transition from the Carboniferous to the Slochteren Formation in well EVD-01 is marked by a 0.9m thick interval of poorly sorted sandstone that can neither be identified as fluvial nor aeolian. In well JPE-01, well-laminated light grey sandstones of the Carboniferous are overlain by aeolian sandstone with well-developed bimodal grain-size lamination separated by a thin (2-3cm) sandstone layer with granule- to small pebble sized clasts.

However, most of the described cores consist of aeolian sandstones deposited in Dry Aeolian Sandflat/Interdune, Aeolian Dune Base and Aeolian Dune Slip Face environments. The main characteristics are described in Table 2-1. The Damp Aeolian Sandflat environment is a subordinate facies that occurs only in short intervals in a few wells. This sub-environment is characterised by wavy laminated sandstones with a slightly increased clay content.

Aeolian Dune Base deposits are often transitional into Aeolian Dune Slip Face deposits, with primary dip angles of lamination gradually increasing in an upward direction from horizontal and low-angle cross-lamination to high-angle cross-laminated, often representing single dune bedforms with (preserved) heights of several decimetres up to 6 meters. No regional or vertical trends were noted in dune bedform heights.

[4]File: NLOG_GS_PUB_1234_DSP-02.tif

Sub-Environment	Code	Main Characteristics	Process	Wells
Damp Aeolian Sandflat	Psah	Non-parallel, silty/very fine-grained to coarse-grained, wavy-laminated sandstone, often poorly sorted and containing minor to moderate amounts of detrital clays	Wind-blown deposits in areas with a groundwater table at or near the sediment surface. Salt crusts will form on the surface in arid settings, trapping windblown sand, silt and clay. Subsequent shallow burial (a few meters) leads to reflux of the salt crusts to the surface by evaporitic pumping, resulting in an irregular, chaotic texture (haloturbation). This sub-environment is uncommon in the study wells.	WGF-01 WYH-01
Dry Aeolian Sandflat/Dry Interdune	Psay	Distinct horizontal (pin-stripe) lamination with discrete grain-size variations on a lamina-scale (bimodal grain-size lamination). Often with very low-angle cross-laminae in cm-thick. It may occasionally contain coarse to very coarse-grained laminae	Produced by wind-ripple migration. Wind ripples have a very high length-to-width ratio and often climb at very low angles, resulting in migrating ripple trains only leaving behind thin veneers of sand. At higher accumulation rates, low-angle wind-ripple foreset laminae may be preserved.	Most wells
Aeolian Dune Base	Adb	Fine- to medium- and occasionally coarse-grained horizontal to low-angle cross-laminated sandstones, often showing steepening-up primary dip angles and distinct bimodal grain-size lamination.	Forming the lower part of aeolian dune bedforms. It may be transitional to the Dry Interdune sub-environment. Sand may be deposited from subaerial suspension on the lee side of aeolian dunes, often modified by wind-ripple migration.	Most wells
Aeolian Dune Slip Face	Ads	High-angle cross-laminated sandstones with dm-scale to m-scale cross-bed sets, that may be stacked or underlain by horizontally- to low-angle cross-laminated sandstone. Often show distinct mm- to cm-scale grain size variations. Cross-bed sets often exhibit sharply truncated upper bed boundaries and may be overlain by deposits of the three previously described sub-environments overlain by subsequent migrating dunes	Representing the steeply dipping slip face of aeolian dunes. Grain-fall processes often deposit sand on the lee side of aeolian dunes that avalanches in thin grain-flow tongues along the front of aeolian dunes. These may be recognised by somewhat thicker (cm-scale) homogeneous layers that often pinch out towards the base of the core. The dominance of grain-fall processes somewhat further away from the dune slip-face causes the lamination to approach the base of the dune tangentially	Most wells
Low-sinuosity Braided Channel	Cfb	Highly variable in grain-size and sedimentary structures. Sandstones are often pebbly or may contain mudstone (rip-up) clasts. May be planar laminated to tabular or through cross-bedded and occasionally ripple laminated. Often intercalated with conglomerate and less frequently with thin mudstone beds. Occasional occurrence of relatively thin, wavy laminated sandstones and sandy/silty mudstones.	Typically exhibit characteristics of deposition by flowing water. Grain-size variations (from mudstones to conglomerates) and varied sedimentary structures (from ripple lamination to upper flow-regime planar lamination) suggest variable hydraulic energy conditions. Cross-bedding is indicative of confined (channelised) flow. Wavy lamination likely reflects deformation by evaporitic processes (haloturbation) during periods of low fluvial activity with the groundwater table in close proximity to the sediment surface	DSP-01 DSP-02 (JUT-01) BNV-01 HLE-01
Pond	Bp	Thin structureless to faintly laminated mudstones with occasional sandy streaks or thin interbeds. Can be ripple-laminated. Generally associated with fluvial sandstone facies.	The association with fluvial facies suggests that mudstone interbeds reflect the temporary abandonment of braid channels or decelerated flow during low run-off.	DSP-01 (BNV-01)

Table 2-1 Overview of description and interpretation of sub-environments based on lithofacies encountered in the cores of the Rotliegend Legacy Core Study. Refer to Figure 2-1 for a visual representation of the depositional sub-environments.

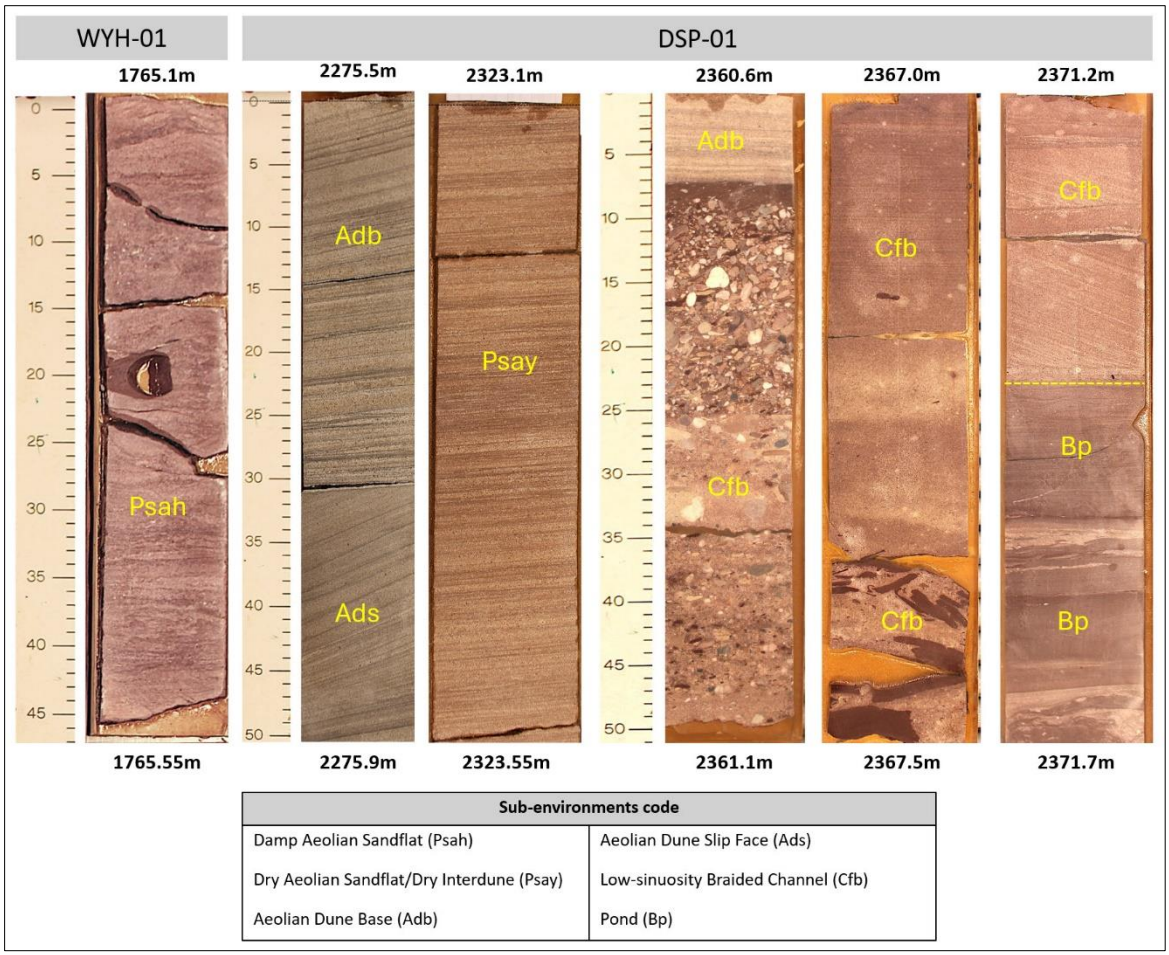

Figure 2-1: Examples of depositional sub-environments encountered in cores from the Rotliegend Legacy Core Study.

2.2 Fractures

The occurrence of naturally fractured sections varies between the study wells in terms of fracture types and their relative abundance. The following core-scale deformation features were encountered as the most prevalent categories within the Slochteren Formation: small-scale faults (SF), deformation bands (DB), cemented fractures (FC), partially-cemented fractures (FPC) and conjugate cemented fractures (CCF). In order to comply with an standardized terminology, the applied descriptors for the fracture categories in this study follow the fracture network glossary introduced by (Peacock et al., 2016):

***Deformation Bands**: a mm-scale tabular zone of localised but non-discrete strain (Friedman and Logan, 1973; Engelder, 1974), typically involving grain reorganisation (grain sliding and rolling), cataclasis (grain flaking, fracturing and crushing) and/or dissolution or precipitation (e.g., Aydin and Johnson, 1978; Knott, 1994). They typically occur in porous granular rock types.*

Deformation bands in the Legacy Core wells occur both in porous sections as well as tight matrix units. The combination of Table 2.4 and Table 2.2 does showcase this overall weak relationship between mean porosity ranges and deformation band occurrence. Note that there are a wide range of terms related to deformation bands, including compactional shear band (Fossen et al., 2007).

***Fault**: defined by the Oxford English Dictionary (1989) as being "a dislocation or break in continuity of the strata or vein", with first usage being attributed to Bakewell (1813). Price (1966) defines a fault as "a plane of fracture which exhibits obvious signs of differential movement of the rock mass on either side of the plane. Faults are therefore planes of shear failure", i.e., they are planes along which there has been movement parallel to the plane. More recent work has shown that faults are usually zones, having a*

volume that includes interacting and linked segments, breccias and fault rocks (e.g., Davatzes and Aydin, 2003; Childs et al., 2009).

***Cemented/Closed Fracture**: used to describe fractures in the subsurface which have zero porosity (e.g., Wu and Pollard, 2002), e.g., because they are sealed by minerals.*

***Conjugate Fractures:** Relationship between two intersecting sets of faults (or joints) that each formed under the same stress field (Daubree, 1878; cited by Dennis, 1967). Two conjugate faults have the opposite shear sense and the same angle (generally ~ 30°) to the maximum principal stress direction (Anderson, 1951).*

The estimated relative occurrence per fracture category across the cored section in each well is listed in Table 2-2. Since the length of cored intervals can vary substantially among the study wells, the allocated values between 1 to 5 are representative for each of the individual core lengths. Examples for each fracture type are summarized in Figure 2-2.

			Fracture Type vs Estimated Relative Occurrence				
No.	Well Name	Described Core Length (m, excl. core gaps)	SF (Small-scale Faults)	DB (Deformation Bands)	FC (Fractures Cemented)	FPC (Fractures Partially-Cemented)	CCF (Conjugate Cemented Fractures)
1	ZEW-01	18.0	1	1	2		
2	BLA-01-S1	9.0					
3	WEP-01	7.6	1		2		
4	JPE-01	14.3			1		
5	WSP-01	8.1	5		3		
6	WRV-01	3.0	2				
7	DRO-01	44.9	2		1	2	2
8	EMO-01	28.0		4		2	
9	WGF-01	14.3			1	2	
10	KAM-01-S1	16.4	3	2	3		
11	EPE-01	3.8			1		
12	SLD-03	24.0		1	2		
13	IJD-01	17.9	2	3	2		1
14	BNV-01-S1	3.3	3	2	1		
15	LSM-01	15.3			1	1	
16	OZN-01	13.6	1	1	1	3	
17	EVD-01	61.4	2		2	4	
18	JUT-01	18.0	1		1	2	
19	ZWK-01	26.3	5	4	3		2
20	HEW-01-S1	155.6	5	5	4	5	2
21	MID-302	28.0	3	3	3		2
22	MID-103-S1	43.3	2	1	2	1	
23	HES-01	2.3	3		1		
24	WYH-01	49.5	4	4	4	3	4
25	LNH-01	5.0			1		
26	HLE-01	22.8	3	4	3	2	
27	MKN-01	13.1	2		2		
28	SLB-01	12.3		2	2		
29	ERM-01-S1	7.0		1	1		
30	DSP-02	4.3				1	
31	Q14-02	33.1		1	2		1
32	HST-02-S1	13.0				2	
33	WAS-23-S2	37.9	1		1		
34	DSP-01	3.6	5	2	3		
		Key	1	2	3	4	5
			Rare	Minor	Common	Very common	Abundant

Table 2-2: Overview of natural fracture types observed in the described core sections. The relative abundance of each deformation feature is expressed as a function of values between 1 (orange fill, rare - not widespread) and 5 (green fill, abundantly present). Note the range in available core length among the study wells.

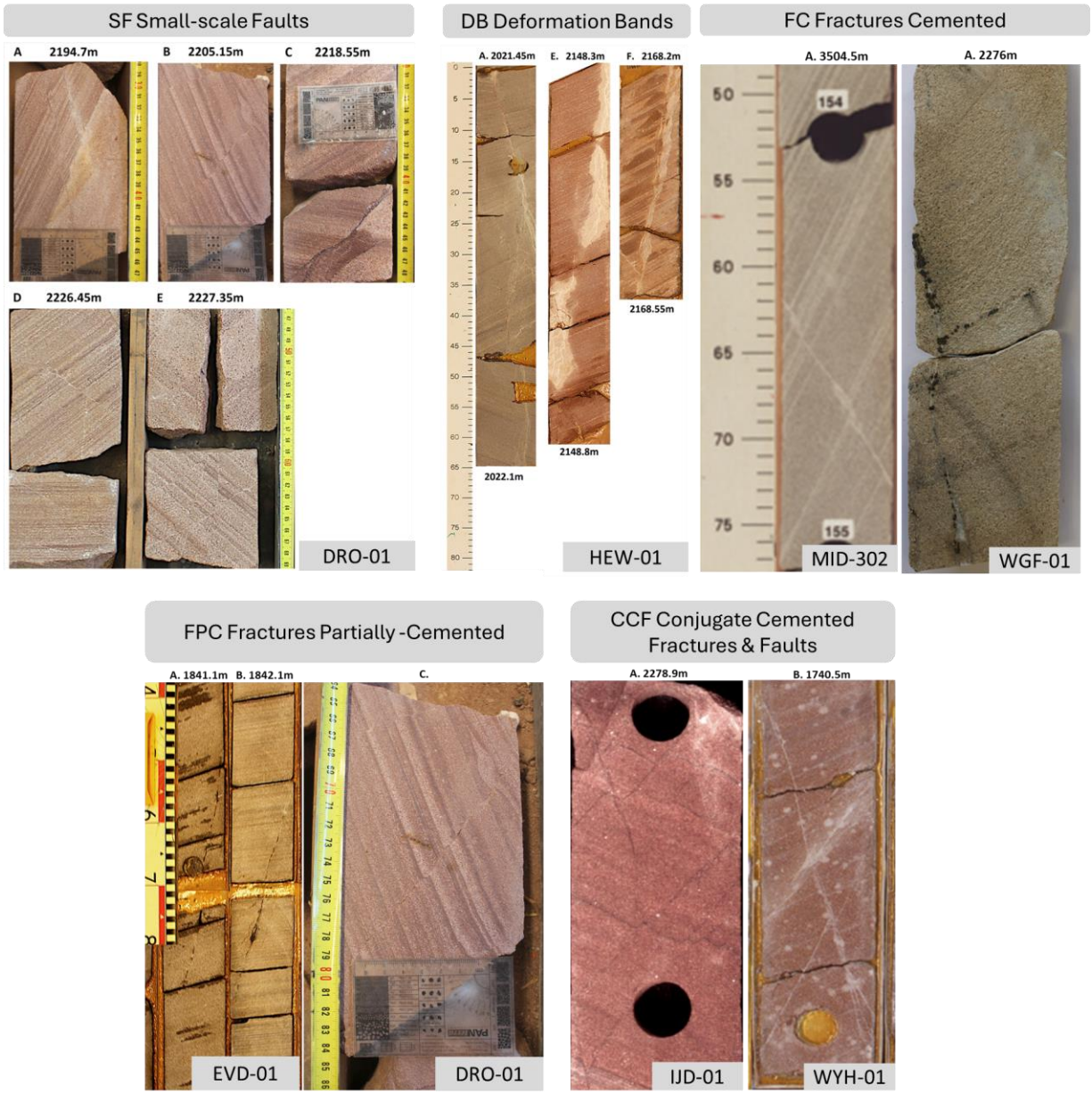

Figure 2-2: Examples of fracture categories encountered in the cored sections of the Rotliegend Legacy Core Study.

No preferential association between fracture type and depositional facies were observed.

Note that wells with the widest variety and highest occurrence of fractures, such as e.g. HEW-01-S1, ZWK-01 and WYH-01, are likely to represent core-scale deformation to what could be part of (sub)-seismic scale fault damage zones. Since seismic cross sections were limited to very few wells in this study, it is possible and highly likely that more wells cover fracture characteristics that are representative for m-scale to dm-scale faulted successions with seismic scale expression. Wells that have reportedly intersected a seismic-scale fault are WYH-01 and WRV-01 and WSP-01 and the location of increased fracture density in the core exhibits the zone of (sub-)seismic scale fault interception or has led to an reduced core lengths.

Among all deformation features observed in the Rotliegend Legacy cores, deformation bands comprise the widest spectrum with respect to geometry, width, orientation and distribution. They can be composite structures with numerous anastomising, mm to cm-scale discrete zones of disaggregation and grain-crushing (e.g. HEW-01-S1, WYH-01) and can also occur in different superimposed directions, varying in dips from shallow to steep relative to bedding (e.g. WYH-01).

Exotic mineralization of fracture planes containing pyrite are developed in EVD-01, WGF-01 and LSM-01. Bleaching around cemented, dilational shear fracture planes is commonly developed in wells KAM-01-S1, HEW-01-S1, indicating paleo-pathways for ascending fluids.

Overall, the fractures in the studied core intervals are dominantly cemented and can cause spatially disconnected matrix pore volumes within the Slochteren Formation.

2.3 Petrography

Petrography was performed on 163 thin-section samples. Additionally, a subset of the petrographic samples was investigated with SEM/BSEM and XRD analysis (see Table 1-1). Petrographic observations indicate that compaction during burial and cementation negatively influenced reservoir quality in the Slochteren sandstone. These key diagenetic processes and cements are described in detail below.

2.3.1 Detrital Mineralogy

The analysed Slochteren sandstones are generally classified as sublitharenites with occasional occurrences of litharenites and subarkoses based on the rock classification scheme of Pettijohn (1975). Detrital quartz is the dominant framework component, with the monocrystalline type being more prevalent than the polycrystalline variety. Sedimentary and metamorphic rock fragments variably occur in subordinate amounts across wells. Sedimentary rock fragments include chert, sandstone/siltstone and claystone clasts. Feldspars (K-feldspar and plagioclase) are not widely recognized, likely due to leaching or replacement of the original grains. They may initially have more commonly been present, as evidenced by observed grain moulds (e.g. Figure 2-3, F) with or without feldspar remnants.

2.3.2 Compaction

Compaction is one of the primary post-depositional processes impacting reservoir quality. The effects of compaction are evidenced by various types of rigid grain-to-grain contacts. Compaction may evolve from mechanical compaction into chemical compaction during progressive burial. Mechanical compaction involves pore space reduction by detrital grain rearrangement without changes in grain shape, and is characterized by point-to-long rigid grain-to-grain contacts. Chemical compaction involves pressure solution at grain boundaries. In the Slochteren Fm., pressure solution resulted in the formation of concavo-convex and sutured rigid grain-to-grain contacts and, in some samples, micro-stylolites. While mechanical compaction is the dominant mechanism noted in this study, chemical compaction is also evident (e.g., HES-01, ERM-01-S1, and WAS-23-S2). The degree of compaction as determined by this method is highly variable throughout the study area. The impact of compaction on reservoir quality is discussed in Chapter 2.4.1.2.

The degree of compaction may also be determined by the COPL-CEPL method, i.e. Compactional Porosity Loss (COPL) versus Cementational Porosity Loss (Lundegard, 1992). This method calculates the relative importance of each of these processes by comparing an assumed value for the initial (depositional) pore volume with the sum of remaining intergranular pore volume and pore-filling cements (known as the “minus-cement porosity”). This method is described in more detail in Chapter 6.5.1Compactional Porosity Loss (COPL) versus Cementational Porosity Loss.

2.3.3 Cementation

Multiple types of authigenic minerals are present in varying amounts, the most common of which are quartz overgrowths, non-ferroan and ferroan dolomite, siderite, anhydrite, kaolinite and illite.

Mineral Phase	Dominant Mineral Morphologies and Occurrences	Plate in Figure 2-3
Quartz	Syntaxial, euhedral overgrowths locally occlude the pore space and pore throats.	**A, B**
Dolomite	Ferroan and non-ferroan compositions. Pore-filling & replacive. Fine to medium-crystalline zoned euhedral and rhombohedral morphologies locally obstruct the pore space. The rhombs may exhibit non-ferroan dolomite cores grading into Fe-richer rims, sometimes exhibiting a more complex compositional pattern (notably in BSEM). Grain-rimming crystalline dolomite rhombs are often present in samples from the top of the Slochteren Formation (e.g., wells ZEW-01, WEP-01, SLD-01, MID-302).	**H, I**
Kaolinite	Pore-filling & replacive. In some wells, up to two generations: (1) tightly packed, crystalline booklets that can completely occlude the intergranular pore space; (2) relatively loose, coarse-crystalline, which tend to be more replacive than pore-filling. In certain wells, kaolinite appears to be recrystallized to its polymorph dickite (e.g., well EVD-01).	**A, B, I**
Illite	Pore-filling and replacive. Multiple habits: (1) inherited detrital coatings tangential to the grain surfaces (likely smectitic in origin and illitised during diagenesis), often brownish, hematite-stained; (2) grain-rimming illite that forms perpendicular to the grain surface, and (3) pore-filling – meshwork – to replacive illite, displaying wispy and pore-bridging habits (e.g., well HES-01).	**J/K, L**
Anhydrite	Pore-filling and replacive. Often occurs as spotty, poikilotopic crystals. It also occurs as a fracture-filling cement.	**C**
Siderite	Pore filling and replacive. It occasionally exhibits corroded brownish to blackish rims (e.g., well WGF-01). Siderite may be common, although not occurring in significant amounts.	**B**
Barite	Not very widespread. Often precipitates in secondary pores or replaces other grains. It has a lath-shaped habit and high relief.	**-**
Pyrite	It is usually replacive. However, it may occur in some wells as a patchy, pore-filling cement (e.g., wells LSM-01, JUT-01, ZWK-01). It is also observed as a fracture-filling cement (e.g., wells LSM-01 and WGF-01).	**E**
Calcite	Ferroan and non-ferroan compositions occur as pore-filling poikilotopic patches and as fracture-filling cement (e.g., well WGF-01).	**E**
Dawsonite $NaAlCO_3(OH)_2$	Generally absent but conspicuous in well HLE-01 and rare in wells MID-103 and WEP-01. Consists of very thin, lath-like crystals with a radial pattern resulting in a chrysanthemum-like shape. It may have evolved outward into thicker, more tabular crystals. (common in well HLE-01, rare in MID-103, and WEP-01). See also Chapter 3.1 - Dawsonite.	**D, G**

Table 2-3: Overview of the main authigenic cements and their occurrence type. The third column indicates the plates of Figure 2-3 that show examples of the described cements.

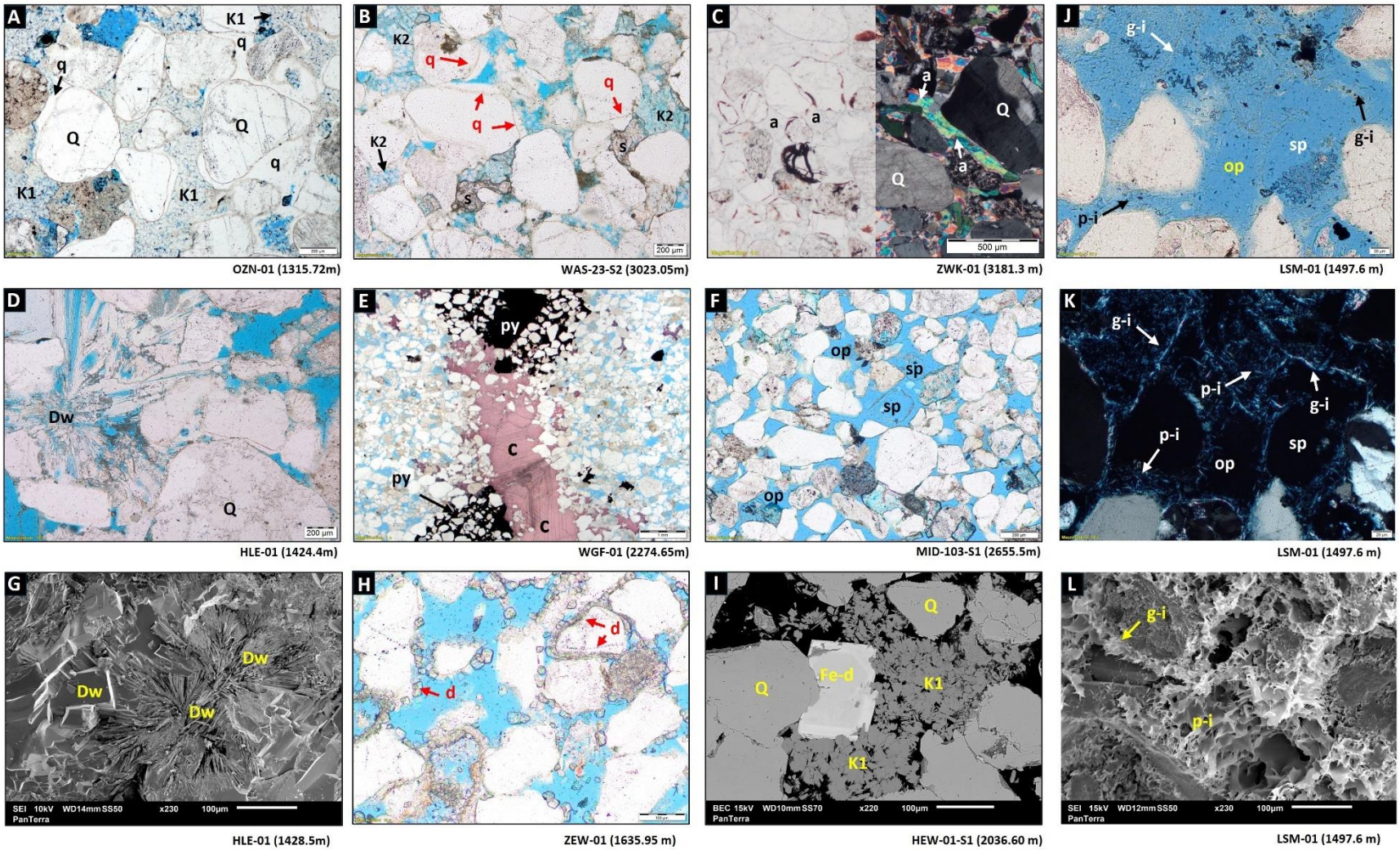

Code	feature
Q	Detrital quartz
q	Pore filling and quartz overgrowths
K1	Densely packed kaolinite
K2	Loosely packed kaolinite
a	Pore occluding anhydrite
Dw	Dawsonite
c	Fracture filling calcite (stained red)
py	Pore filling pyrite
d	Non-ferroan dolomite
Fe-d	Ferroan dolomite
s	Pore occluding siderite
op	Oversized pores
sp	Secondary pores
g-i	Grain-rimming illite
p-i	Pore-filling illite

Figure 2-3 Overview of the main diagenetic features impacting reservoir porosity and permeability. Plates A - K, H: Optical photomicrographs. Plates G & L: SEM images. Plate I: BSEM image.

2.3.4 Paragenetic sequence

Some general statements can be made on paragenetic relations observed in petrographic samples from the EBN Rotliegend Legacy Core Study. Compared with Gaupp and Okkerman (2011), who conducted an extensive study through the Netherlands, Germany, and the North Sea some similarities and differences have been encountered (see Figure 2-4 for a generalised paragenetic sequence as constructed for the Legacy Core Study). However, a comparison with the generalised paragenetic sequence in Fig. 2 of Gaupp and Okkerman (2011) is complicated by the fact that their diagram covers data from a range of burial and thermal histories.

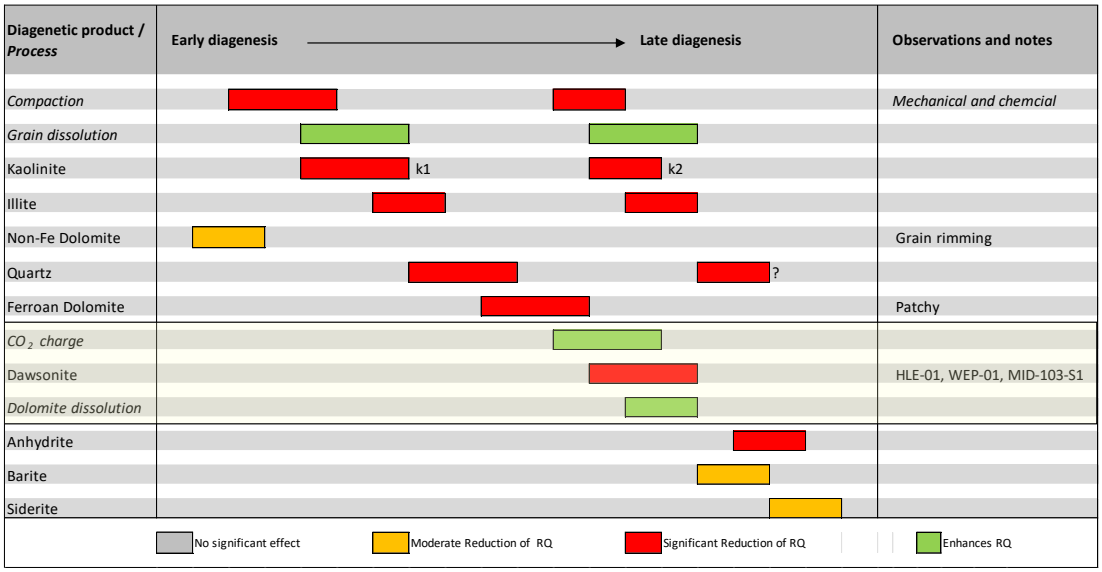

Figure 2-4 **Generalised paragenetic sequence for the EBN Rotliegend Legacy Core Study. Note: Not all phases/processes have occurred in each well. They are dependent on burial and thermal histories. The yellow-shaded portion of the diagram applies only to wells HLE-01, WEP-01 and MID-103-S1, which contain the diagenetic mineral dawsonite, which is an indicator of high CO2 content and extensive dissolution.**

Two habits of kaolinite were observed; one is densely packed (no visible micropores), and the other one is more loosely packed with visible micropores, similar to Gaupp and Okkerman (2011). The densely packed habit is inferred to represent an early phase subjected to compaction, whereas the loosely packed habit is a later phase. The paragenetic sequence in Gaupp and Okkerman (2011) comprises an early burial phase progressing through eodiagenesis into the mesodiagenetic realm. Uplift (Late Jurassic) or inversion (Late Cretaceous - depending on the structural province) with associated telodiagenesis (invasion of meteoric fluids) in specific areas was followed by second phase of burial and mesodiagenesis. The first generation of kaolinite was likely preceded by early dissolution of feldspars as this would have sourced the aluminium for its formation. Although this specific subdivision into different diagenetic realms/phases was not made in the current study, the paragenetic sequences observed in the different wells generally follow this trend, but with different expressions depending on the structural provinces. For instance, the two kaolinite habits were likely pre- and post-uplift (inversion) mesodiagenetic phases. In the diagram of Gaupp and Okkerman (2011), most of the mineral precipitation is inferred to occur in the first burial phase and the telodiagenesis. Although no evidence is presented in the current study, it is likely, however, that significant diagenesis may have occurred in the second deep burial phase, especially in areas that are presently at their maximum burial depth and temperature (e.g., NE Netherlands).

2.4 Reservoir Quality

Legacy routine core analysis (RCA) data were available for 28 wells. Helium porosity, horizontal permeability and, in most cases, grain density measurements on 2200 core plug samples were

incorporated into the study. Porosity and permeability values vary significantly between the study wells, and within individual well data sets. Figure 2-5 shows a cross-plot of mean RCA porosity and geometric mean RCA permeability[5] per well. Horizontal and vertical bars indicate the confidence levels of each data point (+/- 1 standard deviation). The length of these bars is a measure of the internal variability of each well data set. They show a considerable overlap of porosity and permeability values between individual well data sets.

The mean values exhibit a moderately good correlation between porosity and permeability. Based on the correlation (e.g., MID-302, LSM-01 and SLD-03), data points below the trendline exhibit lower permeabilities than expected. Likewise, data points well above the trendline have higher permeabilities than expected for the associated mean porosities (e.g., IJD-01, WYH-01, SLB-01, HLE-01, LNH-01 in Figure 2-5). The reservoir quality data are included in the summary table (see extractions of the summary table in Table 1-3 and Table 1-4; the full summary table is a separate deliverable in Excel format).

It should be noted that in three wells, the cores were subdivided for reservoir quality assessment into two segments (WEP-01 and MID-302) or three (MID-103-S1). This subdivision was made because a significant depth gap separates the core intervals in the first two wells. The cored interval for well MID-103-S1 spans a depth interval of approximately 100m AH divided over 10 cores and shows substantial differences in reservoir quality with depth. The data labels for these wells are colour-coded in Figure 2-5 (green, blue and magenta).

[5] Mean permeability is the geometric mean. Chapter 6.7 - Analysis of Reservoir Quality from Legacy Routine Core Analysis Data explains the applied method to calculate the geometric mean and standard deviation for permeability.

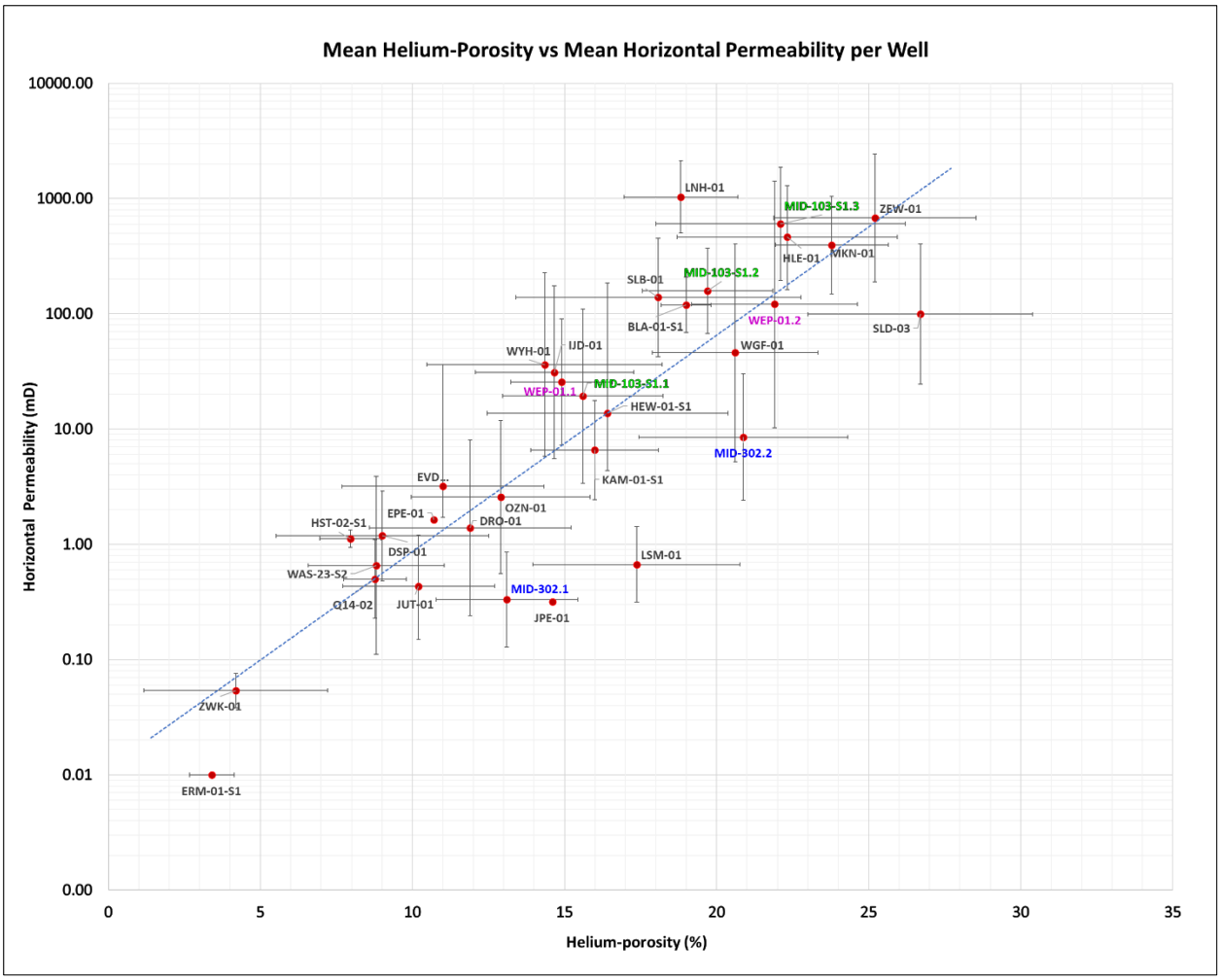

Figure 2-5 **A cross-plot of mean RCA porosity versus (geometric) mean RCA permeability per well with confidence limits (+1/-1 standard deviation) showing the variability in reservoir quality.**

2.4.1 Factors Controlling Porosity & Permeability

2.4.1.1 Facies

There appears to be a limited control of facies on reservoir quality. This is related to the fact that the facies are relatively uniform and mostly consist of sandstones that were deposited in “dry” aeolian settings (Dry Aeolian Sandflat/Interdune, Aeolian Dune Base and Aeolian Dune Slip Face sub-environments). The textural properties of sandstones from these sub-environments are comparable. They comprise moderate well-sorted sandstones horizontally laminated and low- to high-angle cross-laminated sandstone that often exhibit bimodal grain-size lamination. The influence of grain-size or the presence/absence of bimodal grain-size lamination on reservoir quality was not investigated, however. These properties may vary on a centimetre-to-decimetre scale within intervals logged as discrete beds. Grain-size within individual beds is, therefore, not a very well-constrained property in the core descriptions (see also Chapter 6.1.5, Limitations of the Grain-size Descriptive Attribute).

Well WGF-01 is the only well where reservoir quality appears to be controlled by depositional facies. The cross-plot of porosity versus permeability in Figure 2-6 shows a clear differentiation by depositional sub-environment. Core plugs from the Aeolian Dune Slip Face sub-environment exhibit the highest porosity and permeability values, followed by samples from the Aeolian Dune Base sub-environment. The lowest reservoir quality is found in samples from the wavy laminated (and slightly argillaceous) Damp Aeolian Sandflat environment (Psah).

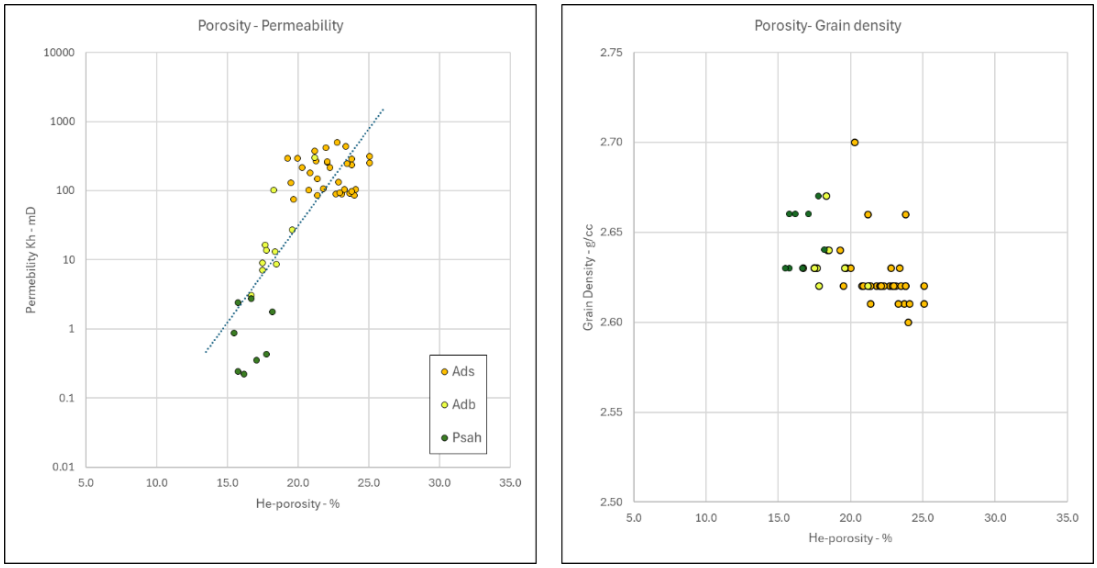

Figure 2-6 **Cross-plots of Helium Porosity versus Horizontal Permeability and Helium Porosity versus Grain Density in well WGF-01. The first plot shows a clear differentiation in reservoir quality between samples from different sub-environments (Ads = Aeolian Dune Slip Face, Adb = Aeolian Dune Base, Psah = Damp Aeolian Sandflat). The second plot shows a slight tendency for samples from the Damp Sandflat (Psah) to have the highest grain densities.**

Differences in reservoir quality between aeolian and fluvial facies could not be investigated. Of the five wells with fluvial deposits, DSP-01 (15m), HLE-01 (0.4m), HES-01 (3m), BNV-01 (1.5m) and DSP-02 (4.3m), only DSP-01 has RCA samples in both aeolian and fluvial facies (lengths refer to the thickness of fluvial facies only). Eight RCA samples were obtained from fluvial deposits occurring at the base of the core in well DSP-01. Permeabilities were too low to measure for all eight samples, which is also the case for 77 out of 103 RCA samples from aeolian sandstones. Porosities of the 8 fluvial RCA samples appear to be somewhat lower than those of the samples from the aeolian section (mean values of 4.4% and 9.4%, respectively). Any differences in textural properties that might have led to contrasting reservoir quality were largely overprinted by diagenesis. The very short fluvial section in HLE-01 (0.4m) was not sampled for RCA, while no RCA measurements were performed in the other three wells. Because fluvial deposits form a minor depositional facies in the cores from the study well, any conclusions on differences in reservoir quality may be irrelevant.

2.4.1.2 Diagenetic Overprints: Compaction, Cementation, Secondary Porosity Generation

Diagenesis plays a key role in shaping the reservoir quality in the Slochteren Formation in general and in the studied area. It likely is strongly influenced by the different burial histories in the respective structural domains in the Dutch subsurface (see Figure 1-2 to Figure 1-4). Diagenetic evolution may have been complex due to several phases of subsidence and uplift, with different timings depending on structural domains. Compaction, authigenesis and grain dissolution have controlled the present-day distribution of reservoir quality. A number of mechanisms have been proposed for the formation of authigenic cements and grain dissolution in the Rotliegend. Lateral migration of brines from the Zechstein Formation in fault juxtaposition with the Slochteren Formation may have introduced sulphate- and carbonate-saturated fluids and led to dolomite and anhydrite cementation (Goldberg, T. et al., 2017). The precipitation of ferroan dolomite may be associated with Fe-rich fluids that were expulsed from the Carboniferous and mixed with carbonate-saturated fluids (Vincent et al., 2018). Acidic fluids associated with hydrocarbon generation in Carboniferous source rocks may also have had a significant impact by dissolving unstable detrital grains and precipitating kaolinite (Gaupp and Okkerman, 2011). Quartz and illite may have precipitated at higher temperatures during advanced burial.

No.	Well	Structural province	Structural Type	Legacy Routine Core Analysis (Mean values)				Compaction				Pore-filling cements (%)							Porosity %				Total Cements (%)			Main factors impacting on reservoir quality	
				No. of core plugs	Helium Porosity (%)	Horizontal Permeability (mD)	Total visible porosity	Rigid grain-to-grain contacts	Grain cont. graded 1-9 (1 = low compaction)	COPL	No. of TS Samples	Ferroan Dolomite	Anhydrite	Quartz	Kaolinite	Pore-filling Illite	Grain-Rimming Illite	Total illite (grain-rimming +pore-filling)	Intergranular	Oversized pore	Intragranular	Total visible porosity	Total hard cements	Total clay cements	Total pore-filling cements	Detrimental	Beneficial
25	LNH-01	GP	Platform	17	18.8	1032.0	12.5	P-L	1.0	32.0	3	2.0	3.2	0.6	0.7	0.1	1.1	1.2	8.3	1.8	2.4	12.5	6.1	1.9	8.0		Low compaction and cementation
1	ZEW-01	CNB	Basin	59	25.2	678.9	15.7	P-L	1.0	27.0	4	7.4	2.3	2.3	2.7	-	0.9	0.9	9.5	1.7	4.6	15.7	12.0	3.7	15.6	Grain-rimming Fe-dolomite	Grain-dissolution
22.3	MID-103-S3.3	CNB	Basin	89	22.1	602.4	16.8	L	2.0	27.0	6	4.6	-	4.2	0.2	0.2	5.2	5.4	10.2	0.9	5.8	16.8	9.1	5.6	14.7	Pore-filling cements	Grain-dissol'n, primary pore preservation
26	HLE-01	CNB	Basin	75	22.3	463.8	15.6	P-L	1.0	28.0	6	4.2	1.6	2.1	2.1	0.6	0.7	1.3	9.5	2.6	3.5	15.6	12.5	3.3	15.8	Pore-filling cements	Grain dissolution
27	MKN-01	FP	Platform	39	23.8	395.3	15.0	L-CC	4.0	31.0	3	5.3	-	2.0	5.4	-	-	-	5.7	3.3	6.0	15.0	9.4	5.4	14.9		**Grain dissolution**
22.2	MID-103-S2.2	CNB	Basin	41	19.7	157.8	18.0	L	2.0	22.5	1	3.7	-	5.7	1.3	0.3	5.0	5.3	13.0	0.7	4.3	18.0	9.4	6.7	16.0	Pore-filling cements	Grain-dissol'n, primary pore preservation
28	SLB-01	FP	Platform	41	18.1	138.9	10.0	P-L	1.0	28.0	4	7.3	6.7	0.4	1.6	-	1.0	1.0	6.5	0.6	2.9	10.0	14.4	2.6	17.0	Pore-filling cements	
3.2	WEP-01.2	CNB	Basin	8	21.9	121.0	18.0	L-CC	4.0	28.0	2	-	3.7	3.3	2.0	-	4.8	4.8	6.7	1.8	9.5	18.0	7.0	7.3	14.3	Pore-filling cements, grain-rimming illite	Grain dissolution
2	BLA-01-S1	CNB	Basin	37	19.0	119.0	13.1	P-L	1.0	28.0	3	1.6	-	5.3	2.6	-	1.8	1.8	9.9	0.9	2.3	13.1	7.9	4.4	12.3		Primary pore preservation
12	SLD-03	NHP	Platform	90	26.7	99.3	13.2	P-L	1.0	31.0	3	8.8	-	0.8	1.8	-	0.4	0.4	7.2	-	6.0	13.2	9.7	2.3	12.0	Grain-rimming Fe-dolomite	Grain dissolution
9	WGF-01	TIJH	High	50	20.6	46.0	13.6	P-L	1.0	34.0	6	0.1	-	1.1	5.2	-	1.2	1.2	6.7	0.1	6.7	13.6	3.8	6.5	10.3	Compaction (from COPL), Kaolinite	**Grain dissolution**
24	WYH-01	CNB	Basin	150	14.3	36.2	9.6	P-L	1.0	33.0	13	2.5	2.8	0.9	1.4	0.1	0.6	0.7	6.7	0.5	2.4	9.6	7.4	2.1	9.4	Compaction (from COPL)	
13	IJD-01	CNB	Basin	72	14.7	31.0	10.7	CC	6.0	33.0	6	3.6	2.5	3.2	2.8	-	0.1	0.1	5.9	0.3	4.4	10.7	9.4	2.9	12.3	Compaction & pore-filling cements	Grain dissolution
3.1	WEP-01.1	CNB	Basin	12	14.9	25.6	12.5	L-CC	4.0	30.0	2	10.0	-	4.7	2.7	-	-	-	6.2	0.5	5.8	12.5	14.7	2.7	17.4	Fe-dolomite	**Grain dissolution**
22.1	MID-103-S1.1	CNB	Basin	43	15.6	19.3	12.7	P-L	1.0	26.0	1	3.0	-	10.0	1.0	-	4.7	4.7	7.0	0.3	5.3	12.7	13.0	5.7	18.7	Quartz overgrowths, Fe-dolomite	**Grain dissolution**
20	HEW-01-S1	CNB	Basin	280	16.4	13.7	12.9	CC	6.0	34.0	10	1.6	-	2.3	5.3	0.1	0.5	0.5	6.0	1.5	5.5	12.9	3.8	5.8	9.7	**Compaction**	**Grain dissolution**
21.2	MID-302.2	CNB	Basin	27	20.9	8.5	17.4	P-L	1.0	26.0	3	2.8	-	0.7	0.2	1.0	5.3	6.3	13.3	0.1	4.0	17.4	3.7	7.1	10.8	Grain-rimming illite	
10	KAM-01-S1	FP	Platform	54	16.0	6.6	9.3	P-L	1.0	30.0	5	5.5	4.3	1.6	3.5	-	-	-	3.0	-	6.3	9.3	11.4	3.5	15.7	Pore-filling cements	Grain dissolution
17	EVD-01	WNB	Basin	116	11.0	3.2	5.3	CC, (S, Sty)	9.0	28.0	11	3.1	0.4	4.2	4.0	4.8	-	4.8	4.1	-	1.2	5.3	10.7	8.8	19.5	**Compaction**, **pore-filling illite**/kaolinite, quartz	
16	OZN-01	CNB	Basin	14	12.9	2.6	7.1	L-CC	4.0	29.0	5	4.5	-	8.5	3.9	0.1	0.3	0.5	4.5	-	2.6	7.1	13.0	4.4	17.4	Compaction, quartz, Fe-dolomite cmt.	
11	EPE-01	CNB	Basin	9	10.7	1.6	5.7	L-Sty	7.0	32.4	1	3.3	-	0.3	-	-	12.0	12.0	3.0	-	2.7	5.7	3.7	12.0	15.7	Compaction, **grain-rimming illite**	
7	DRO-01	CNB	Basin	142	11.9	1.4	7.0	L-(CC)	3.0	30.0	9	3.6	1.1	5.7	4.7	0.0	0.1	0.1	3.6	-	3.5	7.0	10.7	4.8	15.5	**Compaction**, pore-filling cements	(Grain dissolution)
34	DSP-01	CNB	Basin	111	9.0	1.2	3.5	L, CC, S	8.0	36.0	11	1.4	0.2	5.8	1.6	1.8	1.1	2.8	1.5	0.2	1.8	3.5	7.5	4.5	12.0	**Compaction**, quartz, pore-filling illite	
32	HST-02-S1	WNB	Basin	44	8.0	1.1	2.2	L, CC, S	8.0	35.0	4	9.2	0.3	3.0	1.2	0.7	0.8	1.5	1.8	-	0.4	2.2	12.5	2.7	15.2	**Compaction**, pore-filling Fe-dolomite	
15	LSM-01	CNB	Basin	54	17.4	0.7	11.8	P-L	1.0	15.0	2	1.3	-	3.8	3.8	7.7	5.3	13.0	8.7	-	3.2	11.8	14.2	16.8	31.0	**pore-filling & grain-rimming illite**	
33	WAS-23-S2	WNB	Basin	126	8.8	0.7	6.5	L, CC, S, (P)	8.0	33.0	7	0.8	0.1	6.3	3.8	1.3	-	1.3	3.9	0.1	2.5	6.5	7.8	5.1	12.9	**Compaction**, quartz & kaolinite cmt.	
31	Q14-02	WNB	Basin	146	8.8	0.5	4.8	L-CC	4.0	36.0	3	2.3	-	2.7	2.2	0.3	2.2	2.5	3.7	-	1.1	4.8	5.0	4.8	9.8	**Compaction (COPL)**, illite	
18	JUT-01	WNB	Basin	60	10.2	0.4	6.5	CC, S, (Sty)	9.0	24.0	5	4.3	1.1	4.3	0.1	2.5	2.7	5.2	5.0	0.1	1.4	6.5	10.2	5.3	15.5	**Compaction**, illite, Fe-dolomite, quartz cmt.	
21.1	MID-302.1	CNB	Basin	60	13.1	0.3	5.3	P-L	1.0	24.0	1	11.7	-	7.7	1.7	-	2.7	2.7	2.7	-	2.7	5.3	19.3	5.3	24.7	**Fe-dolomite**, quartz cement, grain-rimming illite	
4	JPE-01	CNB	Basin	4	14.6	0.3	9.7	L-CC, (S)	5.0	31.0	5	3.4	0.1	2.5	0.1	-	6.1	6.1	5.7	0.1	3.9	9.7	8.3	6.2	14.5	Compaction, **pore-filling & grain-rimm. illite**	(Grain dissolution)
19	ZWK-01	CNB	Basin	106	4.2	0.1	3.8	L-CC	4.0	31.0	5	0.2	12.3	1.1	-	2.0	3.2	5.2	2.4	0.1	1.3	3.8	13.6	5.2	18.8	(Compaction), anhydrite	
29	ERM-01-S1	CNB	Basin	24	3.4	0.0	1.3	L-S	8.0	35.0	2	3.7	-	6.7	1.8	3.3	0.5	3.8	0.3	-	1.0	1.3	10.3	5.6	16.0	**Compaction**, **quartz**, pore-filling illite	
5	WSP-01	CNB	Basin	n.m.			3.5	fault		29.0	1	5.6	0.4	1.4	0.4	-	6.7	6.7	1.1	-	2.5	3.5	7.4	7.0	14.4	**Cataclasis**, **grain-rimming illite**, quartz cement	
6	WRV-01	CNB	Basin	n.m.			2.0	L-Sty	7.0	34.0	1	6.0	-	0.7	3.0	-	4.7	4.7	2.0	-	-	2.0	6.7	7.7	14.3	**Compaction**, grain-rimming illite	
8	EMO-01	TIJH	High	n.m.			12.6	P-L/L-CC	3.0	28.0	7	7.8	-	0.4	2.4	-	-	-	8.2	-	4.3	12.6	8.1	2.4	10.6	(Compaction), Fe-dolomite cement	Primary pore preservation, **grain dissol'n**
14	BNV-01-S1	CNB	Basin	n.m.			2.3	L-CC	4.0	33.2	1	4.5	7.9	1.5	0.4	-	-	-	1.5	-	0.8	2.3	14.0	0.4	14.3	Compaction, **anhydrite**, Fe-dolomite cement	
23	HES-01	GP	Platform	n.m.			5.0	CC	6.0	37.3	1	0.7	-	5.7	-	1.3	-	1.3	4.7	-	0.3	5.0	6.3	1.3	7.7	**Compaction** (ductile claystone rock fragments)	
30	DSP-02	CNB	Basin	n.m.			-				n.m	-	-	-	-	-	-	-	-	-	-	-	-	-	-		

Conditional formatting legend:
Compaction (based on grain contacts): green = weak, red = strong
Porosity, Horizontal. Permeability: green is high, red is low
Point-counted porosity: a/a

bold = relatively strong impact
() = relatively minor impact

bold = relatively strong impact
() = relatively minor impact

Table 2-4 **Table showing reservoir quality data, quantities of main intergranular pore-filling cements and pore types from point-counting. All values are the mean values per well for each entity. The table is sorted in order of decreasing horizontal RCA permeability. Note: core intervals have been subdivided into two or three segments for several wells to honour differences in reservoir quality (MID 103-S1, WEP-01 and MID-302). CNB = Central Netherland Basin; FP = Friesland Platform; TIJH = Texel-IJsselmeer High; GP = Groningen Platform; NHP = Noord Holland Platform; WNB = West Netherlands Basin.**

Table 2-4 summarises the mean RCA values per well of reservoir properties (helium porosity and horizontal permeability) and petrographic data. The last two columns show the interpreted main controls on reservoir quality based on the data listed in the table. Detrimental and/or beneficial factors are shown only when the impact is considered significant. The wells are sorted in order of decreasing (mean) RCA permeability.

Factors detrimental to reservoir quality

Compaction

Compaction is considered the most important process in porosity reduction. Compaction starts shortly after deposition, and as burial depth increases, it progressively reduces the intergranular pore space. The degree of compaction can be inferred from the nature of rigid grain-to-grain contacts or by using the more quantitative approach of the COPL-CEPL method (Lundegard, 1992; see Chapter 6.5.1, Compactional Porosity Loss (COPL) versus Cementational Porosity Loss).

Grain contacts may be classified according to Pettijohn et al., (1987), ranging from floating (only a limited number of grain-to-grain contacts, indicating minimal compaction occurred) to sutured (strong compaction). The intermediate steps between these grades are long contacts and concavo-convex contacts. The most advanced stage of compaction may result in the development of micro-stylolites. The first three grades (up to long contacts) are achieved by grain rearrangement (mechanical compaction). Concavo-convex contacts, sutured contacts, and micro-stylolites are the product of chemical compaction, whereby the stress on contact points between individual rigid grains causes dissolution at the contact areas between grains (pressure solution). The formation of micro-stylolites is generally promoted by the presence of thin clay laminae

Rigid grain-to-grain contacts were classified on a well-by-well basis according to the classes shown in Table 2-4. As contact types were often variable within individual well data sets, ranges may have been applied, e.g. the range “L-CC, (S)” indicates that long to concavo-convex contacts are predominant with subordinate presence of sutured contacts. These classes were assigned rank numbers from 1 – 9 to indicate the relative intensity of this process, with 1 being the weakest compaction and 9 being the most intense. Similar classifications were assigned the same rank number (c.f., rank 8 in Table 2-5.).

Contact Type	Rank	Legend
P-L	1	P = Point
L	2	L = Long
P-L / L-CC	3	CC = Concavo-convex
L-(CC)	3	S = Sutured
L-CC	4	Sty = Stylolised
L-CC, (S)	5	
CC	6	
L - Sty	7	
L, CC, S, (P)	8	
L, CC, S	8	
L - S	8	
CC, (S, Sty)	9	
CC, S, (Sty)	9	

Table 2-5 **Rigid grain-to-grain contact types as determined for individual wells shown in Table 2-4 (summary of reservoir quality data). The rank number represents the degree of compaction that may affect the core samples from the individual wells (1 = weak compaction, 9 = strong compaction).**

The comparison of compaction rank number with the horizontal RCA permeabilities and the quantity of preserved primary intergranular pores presented in Table 2-4, shows a moderately good match between permeability and compaction intensity, i.e. with an increased rank number (equating to the degree of compaction), permeability and the number of primary pores decrease. Exceptions are wells IJD-01 and HEW-01-S1, which both have a compaction rank number of 6 (i.e. moderately strong compaction) and moderately good mean permeabilities (46mD and 13.2mD, respectively). These wells also contain equal quantities of primary and secondary pores, so that grain dissolution appears to have partially reversed the negative impact of compaction on reservoir quality. Samples from Core 1 in well MID-302 (listed in Table 2-4 as MID-302.1) and from the core well LSM-01 have a compaction rank number of 1 (i.e., low compaction). However, permeabilities are low (0.3mD and 0.7mD, respectively). Reservoir quality in these wells was likely impaired by moderate to extensive cementation with grain-rimming dolomite and grain-rimming illite (well MID-302) and pore-filling and grain-rimming illite (e.g., well LSM-01).

Compaction intensity derived from the COPL shows a much less convincing correlation.

Authigenesis

At various stages during progressive burial, precipitation of authigenic minerals may have further obstructed the pore space. An overview of the main cementing mineral phases is shown in Figure 2-3; Table 2-4 shows the mean values per well of the most important cements. Rhombohedral ferroan-dolomite and quartz overgrowths are common pore-filling cements in almost all wells, and in a number of wells, minor to moderate amounts of anhydrite may be present (e.g., well ZWK-01 and SLB-01). These are the most common rigid pore-filling cements that negatively influence porosity and permeability. Other pore-filling cements are: non-ferroan dolomite and siderite. Dawsonite is an exotic mineral, that is common in one well (HLE-01) and has been observed in trace amounts in several other wells (MID-103-S1 and WEP-01). Although in itself reducing pore space, it is associated with extensive grain dissolution, which appears to have significantly improved reservoir quality (see Chapter 3.1 - Dawsonite).

Other common and important cement types that strongly influenced reservoir quality are the authigenic clays kaolinite and illite. Of the two types, illite has the strongest permeability-reducing impact, even when present in relatively minor amounts. Patchily distributed, pore-filling, vermicular kaolinite also reduces primary pore space and does occur in two different habits: a relatively early, densely-packed variety without visible micro-pores (c.f. Figure 2-3, A) and a more loosely packed variety (c.f. Figure 2-3, B), which is thought to have precipitated later in the paragenetic sequence.

Authigenic illite may occur in different habits: tangential, grain-rimming, and pore-filling/bridging. Each habit may impact reservoir quality differently. Illustrations of each type can be seen in Figure 2-3, Plates I, J and K, and Figure 2-7.

Tangential illite is represented by generally incomplete cutans on detrital grain surfaces. They originate from infiltrated clays that may initially have been smectitic in composition and were subsequently illitised during diagenesis. They are often hematite-stained, which gives them a brownish/reddish color. The cutans formed on detrital grains in a different depositional setting and were subsequently transported, and partially abraded. The indication of its inherited character is the thickening of this cutans at grain embayments.

Grain-rimming illite is often detrimental to permeability since it may obstruct pore throats.

Pore-filling illite is particularly detrimental to permeability, even in minor amounts. It effectively blocks pores and pore throats with limited impact on porosity due to the high content on microporosity.

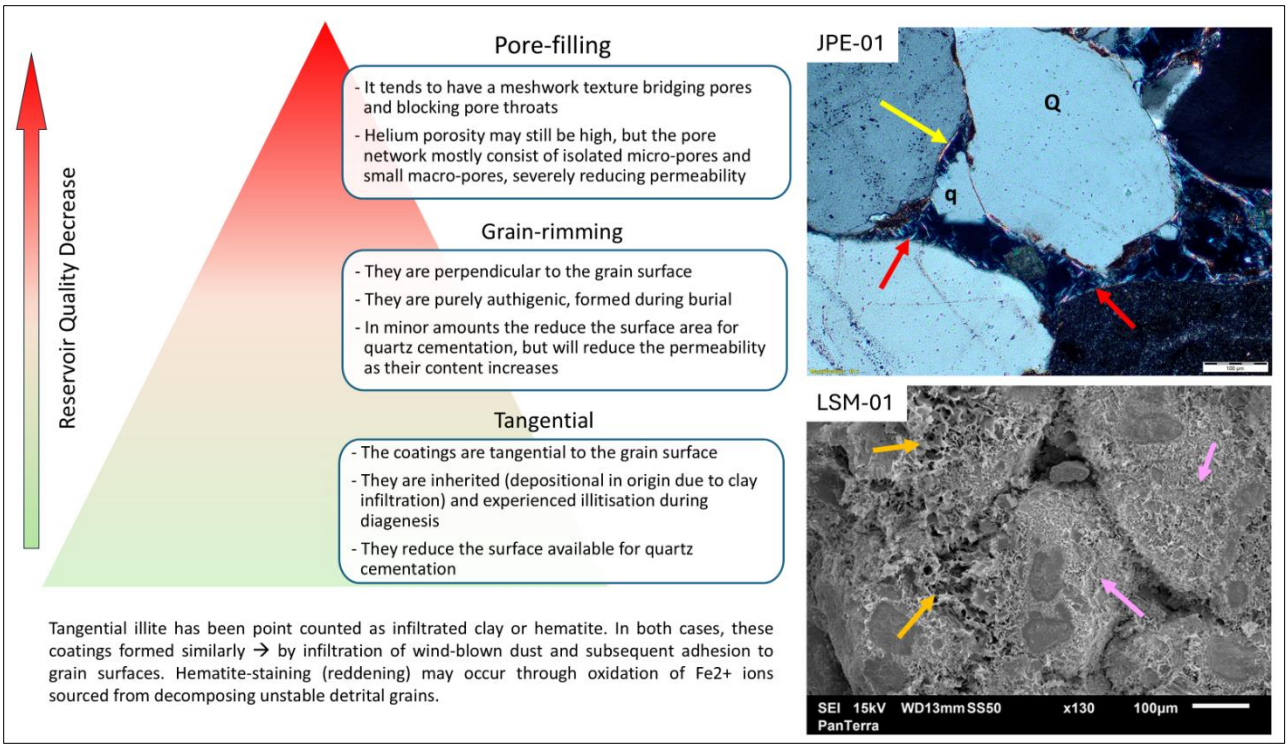

Figure 2-7 **Illustrative description of the different types of illite occurring in the Rotliegend among the studied wells. The colour gradation indicates the degree of negative impact on reservoir quality (greenish = less detrimental *vs*. red = more detrimental). The thin-section photomicrograph is taken in cross-polarized light to identify the high-birefringent illite platelets and fibres more easily. The yellow arrow points to tangential illite, the red arrow points to grain-rimming illite, and the orange arrow indicates the presence of pore-filling (meshwork) illite. Note that tangential illite may act as a nucleation substrate for grain-rimming illite. The SEM image (lower right) shows weakly developed grain-rimming illite (at magenta arrows) that have locally evolved into pore-filling and bridging illite (orange arrows).**

Figure 2-8 shows the relation between helium porosity and permeability for two sets of wells. The orange data points represent RCA data from wells with low illite content, while the dark blue data points are from wells with significantly higher amounts of illite. The chosen wells have relatively high mean helium porosity values, albeit somewhat higher for the wells with low illite content. Wells with relatively high illite content and much lower porosity values were excluded from the comparison. Other factors, such as stronger compaction or more abundant other pore-filling cements, may also have influenced permeability in those wells. From the plot in Figure 2-8, it can be seen that over a range of porosities from approximately 7% to 25%, the permeabilities for the samples from wells with common illite are 1.5 to 3 orders in magnitude

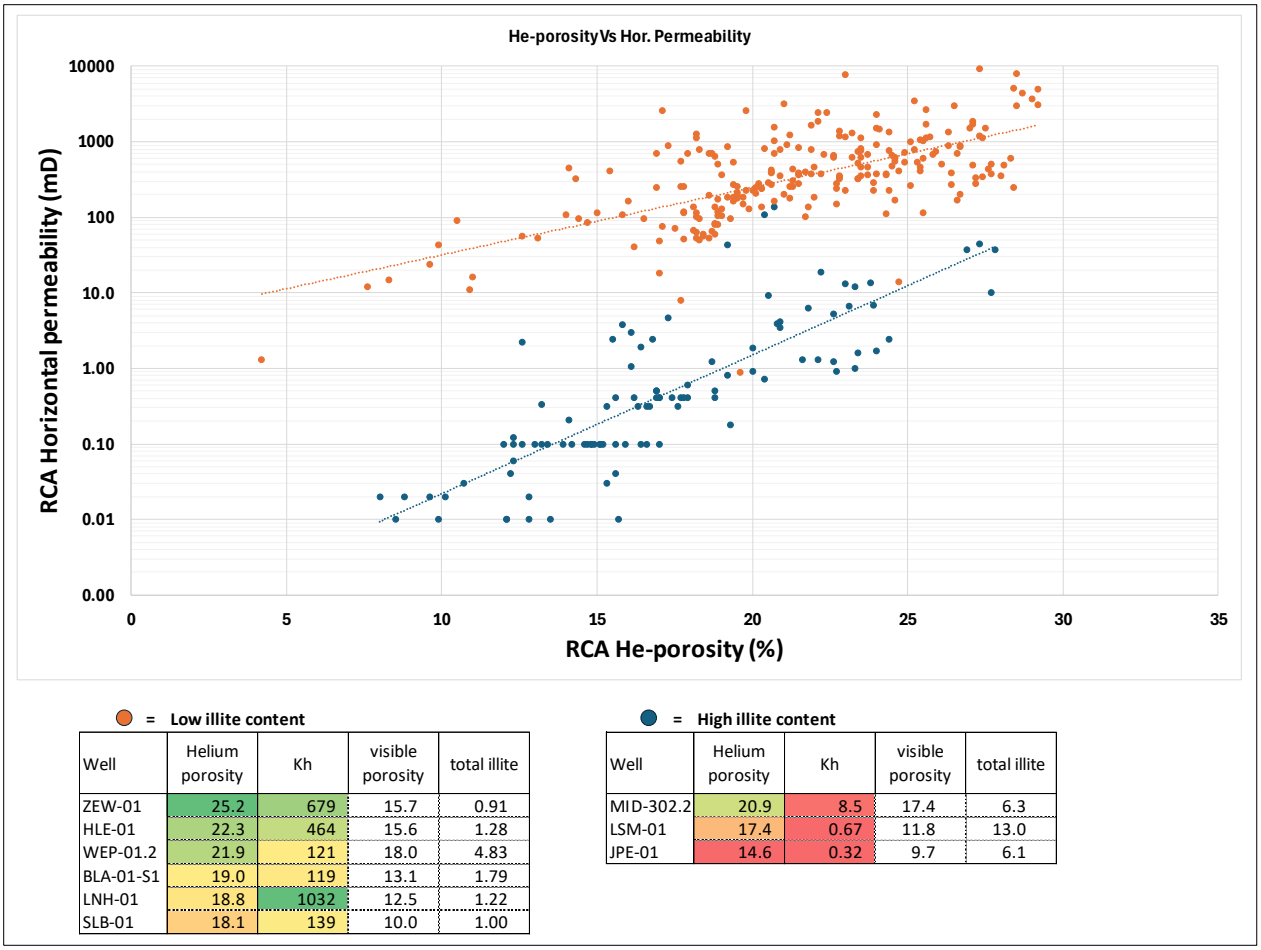

Well	Helium porosity	Kh	visible porosity	total illite
ZEW-01	25.2	679	15.7	0.91
HLE-01	22.3	464	15.6	1.28
WEP-01.2	21.9	121	18.0	4.83
BLA-01-S1	19.0	119	13.1	1.79
LNH-01	18.8	1032	12.5	1.22
SLB-01	18.1	139	10.0	1.00

Well	Helium porosity	Kh	visible porosity	total illite
MID-302.2	20.9	8.5	17.4	6.3
LSM-01	17.4	0.67	11.8	13.0
JPE-01	14.6	0.32	9.7	6.1

Figure 2-8 RCA porosity and permeability of wells with abundant authigenic illite (blue data points) vs. wells with minor amounts of illite (orange data points).

A special case is the Weissliegend facies, known to occur in parts of the onshore and offshore regions of the Dutch subsurface. This term is used in The Netherlands as an informal classification of white to grey, often structureless sandstones at the top of the Rotliegend immediately below the Coppershale (Kupferschiefer). The “Weissliegend” is interpreted to represent reworked and fluidised aeolian dunes caused by the sudden flooding of the Southern Permian Basin at the end of the Permian Rotliegend. Subsequent bleaching of the red desert sediments was caused by reducing bottom water and/or formation water (Ojik et al., 2011) Fryberger et al., 2011).

On the wireline logs, several wells in the Legacy Core Study (ZWK-01, MID-103-S1 and MID-302) exhibit progressive impairment of reservoir quality over intervals of several tens of meters towards the top of the Slochteren Formation (see Figure 2-9 the wireline log expression in well MID-302).

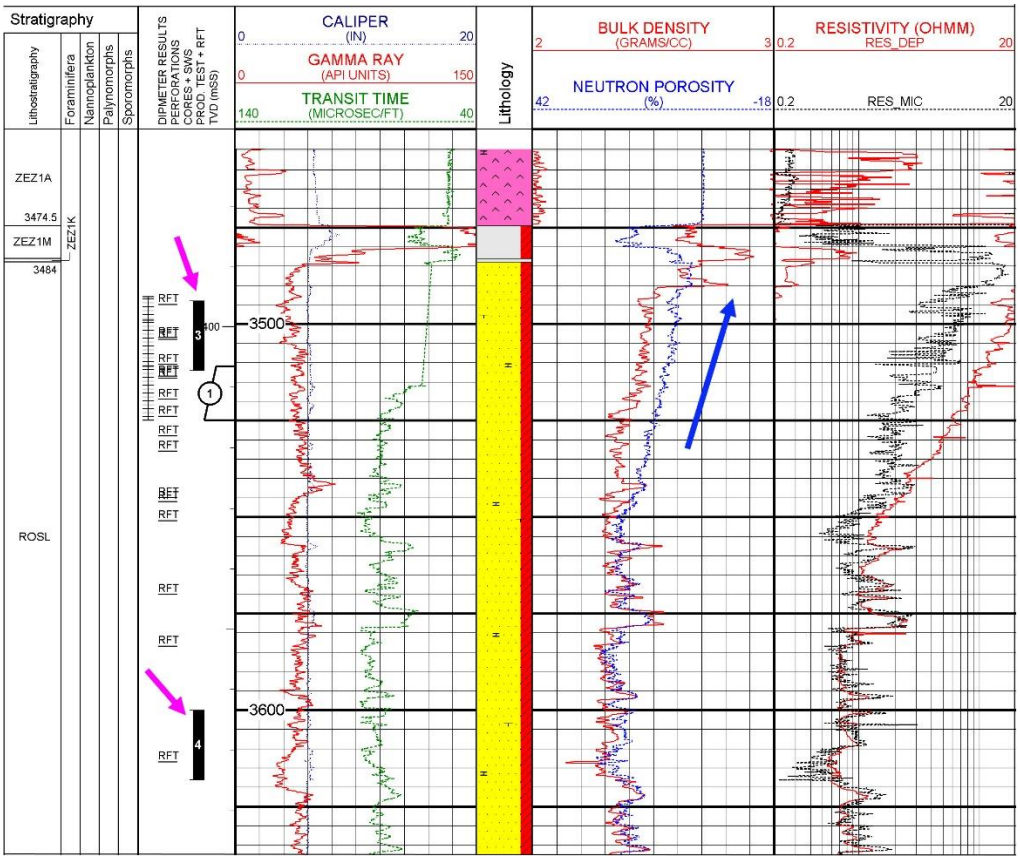

Figure 2-9 **This section of the composite log from well MID-302 shows the decreasing reservoir quality toward the top of the Slochteren formation associated with the Weissliegend facies (the blue arrow indicates the trend of increasing bulk density and decreasing neutron porosity). Magenta arrows point to described and sampled Cores 3 and 4.**

A limited number of petrography samples from this interval were analysed, exhibiting non-unique petrographic expressions. Well ZWK-01 (5 samples) has very low reservoir quality due to the combined effects of pervasive anhydrite cementation and, to a lesser extent, grain-rimming illite, while compaction is moderate. Wells MID-103-S1 and MID-302 have one thin-section sample each from this interval. Reservoir quality in the cored Weissliegend interval of the first well is significantly higher, with mean values of porosity and permeability of 15.6% and 19.3mD, respectively (n = 43). Mean values in MID-302 are 13.1% and 0.33mD (n=60). The thin-section from the latter wells exhibits significant cementation with ferroan dolomite, quartz and grain-rimming illite. The sample from MID-103-S1 is characterized by abundant quartz cement and lesser amounts of grain-rimming illite and Fe-dolomite. Visible (point-counted) porosity is 12.7% in MID-103-S1 and 5.3% in MID-302. The limited sampling in the latter two wells does not permit a more accurate assessment of the causes of reduced reservoir quality in the Weissliegend.

Factors beneficial to reservoir quality

Several factors may have been beneficial for preserving or improving reservoir quality. The most obvious one is limited burial depth. Other factors are late (post-compactional) grain dissolution and the development of thin illite grain coatings.

Limited Burial Depth

Although no in-depth review on maximum burial depths was performed, published burial curves (e.g., see Figure 1-4) show that the Slochteren Formation was probably never buried very deeply (2000m ± ca. 300m and currently at its maximum burial depth) in structural domains known as platform areas (Noord Holland, Friesland and Groningen Platforms). Samples from the Slochteren Formation in wells from these areas

generally have good reservoir quality. A number of wells at the northern edge of the Central Netherlands Basin also exhibit good reservoir quality (HLE-01, MID-103-S1, WEP-01, WYH-01 and ZEW-01). All these wells have present day depths of between ca. 1400m – 1700m TVD, except for well MID-103-S1, which is at a present day depth of ca. 2500m TVD.

Grain Dissolution

Late grain dissolution was an important process in some wells. It partially reversed the detrimental effects of compaction. Partial to complete dissolution of chemically unstable grains, such as feldspars or sedimentary chert, resulted in secondary, intragranular visible pores. In some cases, secondary pores are equally to more abundant than primary pores (e.g., WEP-01, MKN-01, WGF 01, SLD-01, among others – see Table 2 5). They are likely an important contributor to helium porosity. When extensive dissolution occurs, secondary pores (c.f. Figure 2-3, F, J) may amalgamate with the adjacent primary pores, resulting in oversized pores rarely exhibiting any evidence of the precursor grain or cement type. This may lead to a very well-connected pore network and high permeabilities.

In a few places, the occurrence of significant grain dissolution appears to be associated with the presence of the mineral dawsonite (see also Chapter 3.1) as a pore-filling cement. Samples from well HLE-01 contain between 1% and 4.7% dawsonite. Other wells with dawsonite are MID-103-S1 and WEP-01 (in the final report of the last well, it is not described because it was initially not identified). The formation of dawsonite in sedimentary rocks is thought to occur under the presence of high partial CO2 pressure (Hellevang et al., 2004).

Grain-rimming illite

When present in minor amounts, forming thin, continuous rims around detrital grains, illite may inhibit the formation of quartz overgrowths preserving pore space.

2.4.1.3 Regional Variability in Reservoir Quality

Some general patterns can be identified from data in Table 2-4 and Figure 2-10 related to the structural domains in which the legacy wells are located. Wells in the West Netherland Basin (WNB) generally have low porosities and permeabilities. Thin sections from these wells show strong compaction as suggested by the nature of rigid grain-to-grain contacts and the COPL values. The Central Netherland Basin (CNB) shows a wide scatter in porosities and permeabilities (c.f. Table 2-6). This domain contains 25 of the 34 wells and is structurally more differentiated than the generalized map of Figure 1-2 may suggest. The cross-section in Figure 1-3 shows complex structuration between the Peel-Maasbommel High in the southwest and the Friesland/Groningen Platforms in the northeast.

Well	Mean He-Porosity (%)	Mean Hor. Permeability (mD)
ZWK-01	4.2	0.05
MID-103-S1.1	15.6	19.3
DRO-01	11.9	1.39
ZEW-01	25.2	679

Table 2-6 **Two pairs of wells in the Central Netherlands Basin, showing contrasting reservoir quality. The first two wells are located in the province of North Holland some 8.5km apart (both with cores in the top of the Slochteren Formation). The second pair is located in the north of the province of Flevoland (E. of the IJsselmeer) separated by a distance of approximately 18.5km. Note that mean porosities and permeabilities are based on RCA measurements from cores that only sampled part of the Slochteren Formation. They may not be altogether representative of the full Slochteren intervals in these wells**

High to very high porosities and good to very good permeabilities are observed in the cored sections of the Slochteren Formation in the majority of wells located in the Friesland, Groningen, and Noord Holland

Platforms (FP, GP, and NHP, respectively) as well as in a number of wells on the northern flank of the Central Netherlands Basin (see Table 2-7 for ranges in values). These elevated values are in part due to the lack of deep burial. Additionally, grain dissolution may have created significant secondary porosity in several wells, (e.g., wells HLE-01, WEP-01, MKN-01, KAM-01-S1), with evidence of a late CO_2 charge in the first two wells as suggested by the presence of dawsonite.

Well	Structural province	Structural Element Type	Structural Element No.	Helium Porosity (%)	Horizontal Permeability (mD)
LNH-01	GP	Platform	1	18.8	1032.0
ZEW-01	CNB	Basin Flank	2	25.2	678.9
MID-103-S3.3	CNB	Basin Flank	2	22.1	602.4
HLE-01	CNB	Basin Flank	2	22.3	463.8
MKN-01	FP	Platform	1	23.8	395.3
MID-103-S2.2	CNB	Basin Flank	2	19.7	157.8
SLB-01	FP	Platform	1	18.1	138.9
WEP-01.2	CNB	Basin Flank	2	21.9	121.0
BLA-01-S1	CNB	Centre	4	19.0	119.0
SLD-03	NHP	Platform	1	26.7	99.3
WGF-01	TIJH	High	3	20.6	46.0
WYH-01	CNB	Basin Flank	2	14.3	36.2
IJD-01	FP	Platform	1	14.7	31.0
WEP-01.1	CNB	Basin Flank	2	14.9	25.6
MID-103-S1.1	CNB	Basin Flank	2	15.6	19.3
HEW-01-S1	CNB	Centre	4	16.4	13.7
MID-302.2	CNB	Basin Flank	2	20.9	8.5
KAM-01-S1	FP	Platform	1	16.0	6.6
EVD-01	WNB	Centre	4	11.0	3.2
OZN-01	CNB	Centre	4	12.9	2.6
EPE-01	CNB	Centre	4	10.7	1.6
DRO-01	CNB	Basin Flank	2	11.9	1.4
DSP-01	CNB	Basin Flank	2	9.0	1.2
HST-02-S1	WNB	Centre	4	8.0	1.1
LSM-01	CNB	Centre	4	17.4	0.7
WAS-23-S2	WNB	Centre	4	8.8	0.7
Q14-02	WNB	Centre	4	8.8	0.5
JUT-01	WNB	Centre	4	10.2	0.4
MID-302.1*	CNB	Basin Flank	2	13.1	0.3
JPE-01	CNB	Centre	4	14.6	0.3
ZWK-01	CNB	Centre	4	4.2	0.1
ERM-01-S1	CNB	Centre	4	3.4	0.0

Platform	1
Basin Flank	2
High	3
Centre	4

Table 2-7 **Wells ranked by mean RCA permeability (in decreasing order of magnitude) and by structural element type. Wells in the Central Netherlands Basin (CNB) have been subdivided into (northern) Basin Flank and Centre. FP = Friesland Platform; GP = Groningen Platform; NHP = Noord Holland Platform; TIJH = Texel-IJsselmeer High; WNB = West Netherlands Basin. Coloured cells are conditionally formatted; RCA porosity and permeability from green (high) to red (low), structural element type numbered 1 (green) to 4 (red). Note: Core 1 of MID-302 (MID-302.1*) has low reservoir quality caused by extensive grain-rimming dolomite associated with the Weissliegend facies**

Illustrative summaries of the main diagenetic controls on porosity and permeability are shown in Figure 2-10-and Figure 2-11.

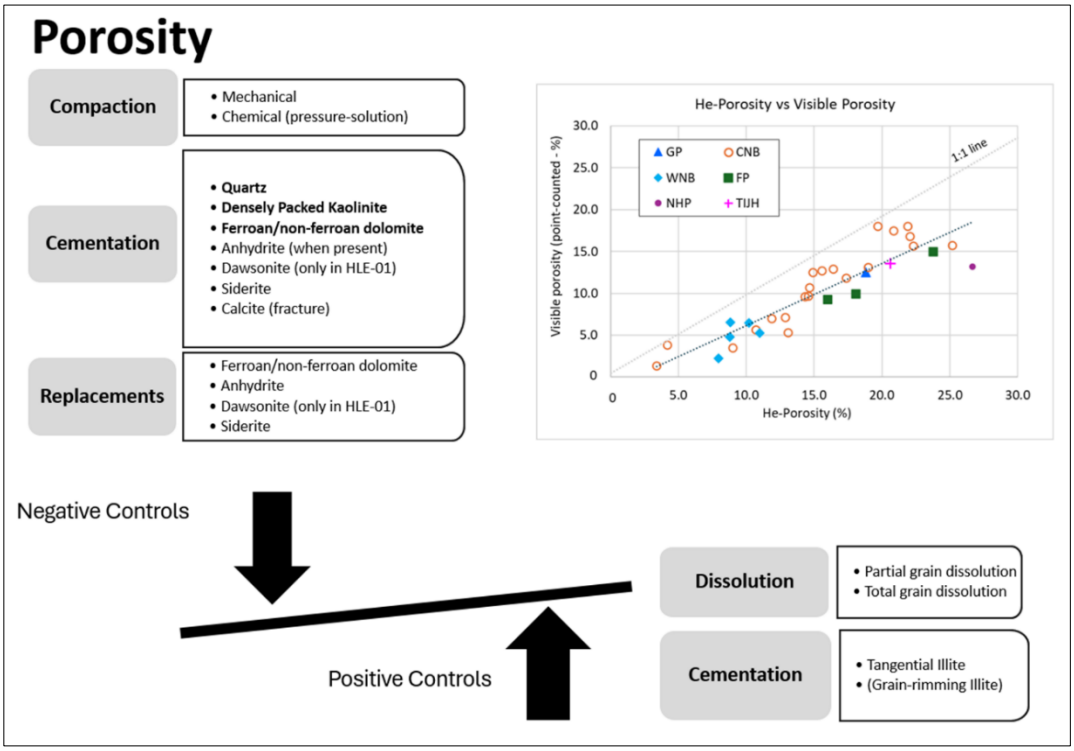

Figure 2-10 **Illustrative summary of the general controls on reservoir porosity during diagenesis (refer to Figure 2-3, A-L for examples of various cement types). The cross-plot of RCA He-porosity vs. visible porosity shows a good agreement between the average values of the two entities per well, with the visible porosity systematically lower (i.e., below the 1:1 line) than the RCA He-porosity, as micro-porosity cannot be distinguished in thin sections. (Color-coding is by structural province. CNB = Central Netherland Basin; FP = Friesland Platform; TIJH = Texel-IJsselmeer High; GP = Groningen Platform; NHP = Noord Holland Platform; WNB = West Netherlands Basin).**

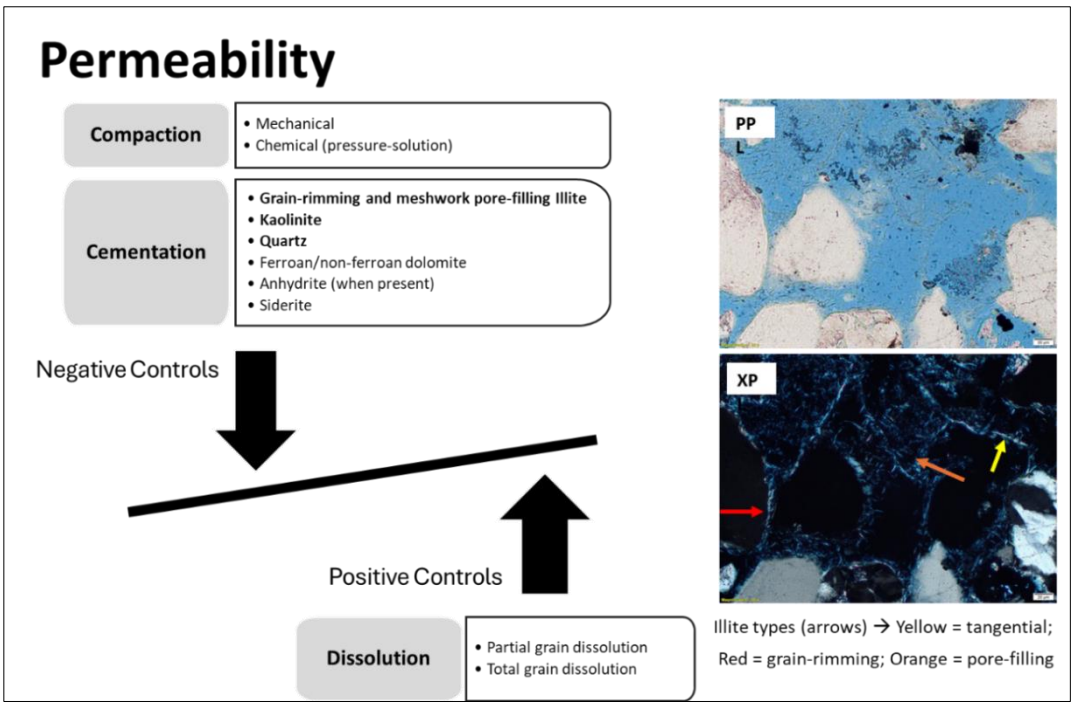

Figure 2-11 **An illustrative summary of the general controls on reservoir permeability during diagenesis (see Figure 2-3, Plates A-I for examples of different authigenic minerals). Note that meshwork illite and thick grain-rimming illite are especially detrimental to permeability. Thin-section photomicrographs from well LSM-01, sample 1497.6m. (PP = plane polarised light, XP = cross-polarised light).**

3 Additional Observations

3.1 Dawsonite

The occurrence of dawsonite is associated with good reservoir quality. Conspicuous in well HLE-01, present in trace amounts in wells WEP-01[6] and MID-103-S1. The characteristics, origin, and semiquantitative chemical composition of dawsonite are summarized in Figure 3-1. An important prerequisite for its formation is high CO_2 partial pressure. The gas in the Middelie field (well MID-103-S1) contains 29% CO_2 (NLOG). The spatial distribution of dawsonite is unpredictable since other wells in the vicinity these wells do not contain dawsonite.

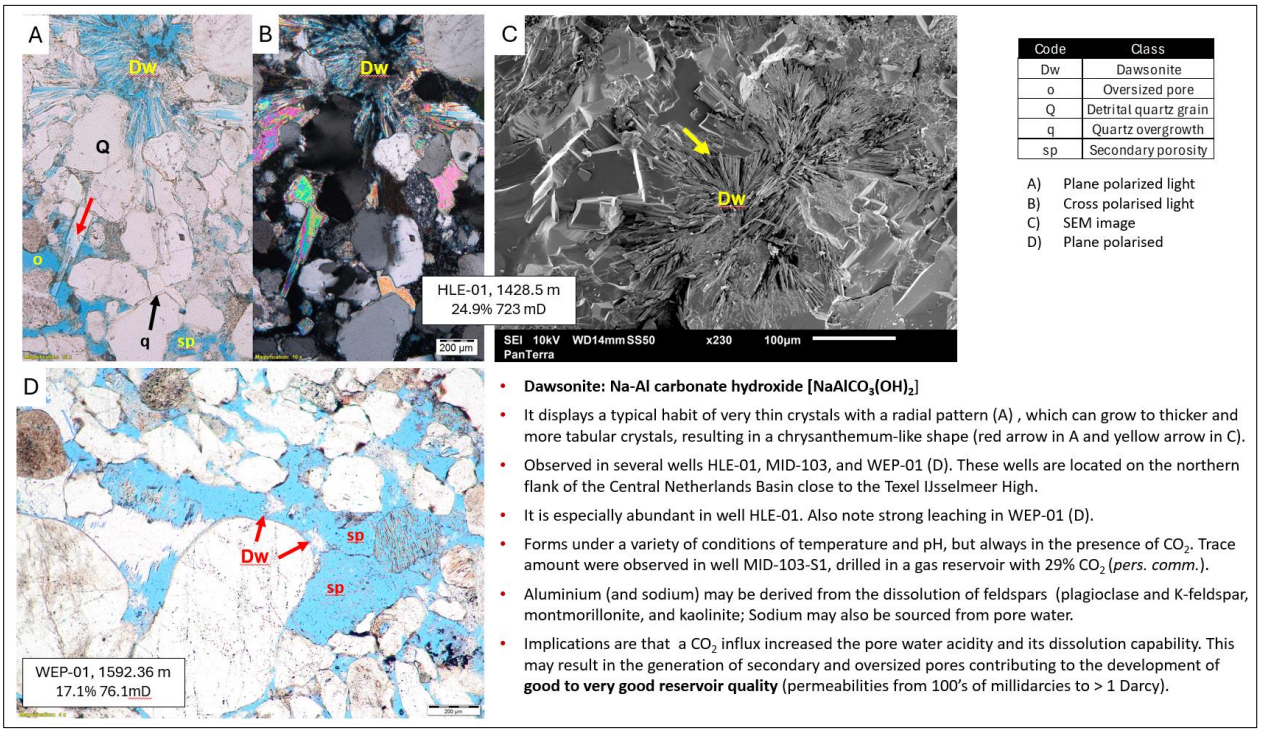

Figure 3-1 **An illustrative summary of the key findings and their impact on reservoir quality of dawsonite occurrences in several of the analysed wells from the Slochteren Formation in The Netherlands. A) Plane polarized light optical image showing the typical habit of the dawsonite. B) Crossed polarized light optical image showing the high birefringence colours of the dawsonite, similar to those of the anhydrite. C) SEM image showing the texture of the dawsonite. D) This micrograph from well WEP-01 exhibits extensive secondary porosity due to leaching. Dawsonite is present as small rosettes (red arrow).**

3.2 Data Discrepancies

Several discrepancies were observed in the studied data sets. They are described as a reference for future studies on legacy data that, due to their age and history, may pose unexpected issues.

Discrepancies exist between the RCA data, observations on thin-section and XRD data in two of the 34 analysed wells (i.e., EVD-01 and WYH-01). Ultimately, it was concluded that the RCA data are likely correct but that at least some of the core plugs used for petrographic analysis were incorrectly depth referenced for archiving at the storage facility and are no longer representative. Descriptions of observations supporting this statement are summarized in Figure 3-2 and Figure 3-3.

[6] Dawsonite was initially not identified in samples from well WEP-01, as it occurs in trace amounts. Only after its occurrence in well HLE-01 was clearly established, it could also be recognised in well WEP-01. Samples from this well share the same characteristic of well HLE-01 in that it has very-well developed secondary porosity due to grain dissolution.

- In well WYH-01, the RCA data of six of the thirteen samples appear not to agree with the porosity characteristics observed in the thin sections (Table 1).
- In the samples highlighted in yellow, the visual porosity (Fig. A, sample 7 – 1748.4m) is higher than the helium porosity, which is highly unlikely to occur. Visible porosity is usually lower than helium porosity since (invisible micro-pores) in detrital and authigenic components also contribute to helium porosity.
- The samples highlighted in green exhibit very low visible porosity (Fig. B sample 5 – 1739.7m) compared to the helium porosity, which implies micropores are the dominant contributor to helium porosity. This contradicts the high measured horizontal permeability values (2083mD and 2400mD). It is assumed that RCA data are correct, as it is likely that the sample mix-up occurred after the routine core analysis measurements were performed.

Table 1

Well	Sample No.	Depth (m)	Porosity (%)			Sum matrix (%)	Core Analysis			Compaction and Cementation (%)				
			Visual porosity	Micro Porosity	Sum intergranular porosity		Helium Porosity (%)	Horizontal Permeability (mD)	Grain Density (g/cm^3)	Pore filling Cement	Minus cement porosity	IGV	COPL	CEPL
WYH-01	1	1723.3	8.7	4.1	5.0	-	12.8	158	2.65	11.3	16.3	16.3	34.3	7.5
WYH-01	2	1724.5	5.7	7.4	3.3	0.7	13.1	4.2	2.65	13.3	16.7	17.3	34.0	8.8
WYH-01	3	1728.1	13.7	-	10.3	-	13.0	222	2.66	7.0	17.3	17.3	33.5	4.7
WYH-01	4	1735.5	11.3	3.6	9.7	2.0	14.9	164	2.66	10.3	20.0	22.0	31.3	7.1
WYH-01	5	1739.7	3.7	20.8	2.0	8.7	24.5	2083	2.64	12.0	14.0	22.7	36.0	7.7
WYH-01	6	1743.6	8.7	15.3	7.0	4.0	24.0	2400	2.65	8.7	15.7	19.7	34.8	5.7
WYH-01	7	1748.4	16.0	-	10.0	2.7	9.1	5.1	2.67	7.0	17.0	19.7	33.7	4.6
WYH-01	8	1752	3.3	9.4	1.7	14.7	12.7	n.m.2	2.68	7.7	9.3	24.0	N.D.	N.D
WYH-01	9	1754.5	11.3	-	9.3	2.7	10.3	1.2	2.66	13.7	23.0	25.7	28.6	9.8
WYH-01	10	1755.9	18.3	-	13.0	-	15.3	18.0	2.66	8.3	21.3	21.3	30.1	5.8
WYH-01	11	1758.9	8.0	4.4	5.3	14.7	12.4	30.0	2.64	13.7	19.0	33.7	N.D.	N.D.
WYH-01	12	1759.7	10.3	2.7	5.7	9.0	13.0	n.m.2	2.66	15.3	21.0	30.0	30.4	10.7
WYH-01	13	1762.4	6.8	8.3	5.1	6.0	15.1	75.0	2.72	13.7	18.8	24.8	32.3	9.2

1) Visual porosity = sum primary and secondary porosity
2) Micro porosity = Helium Porosity minus Macro Porosity

COPL = Compactional porosity loss
CEPL = Cementational porosity loss
IGV = Intergranular Volume

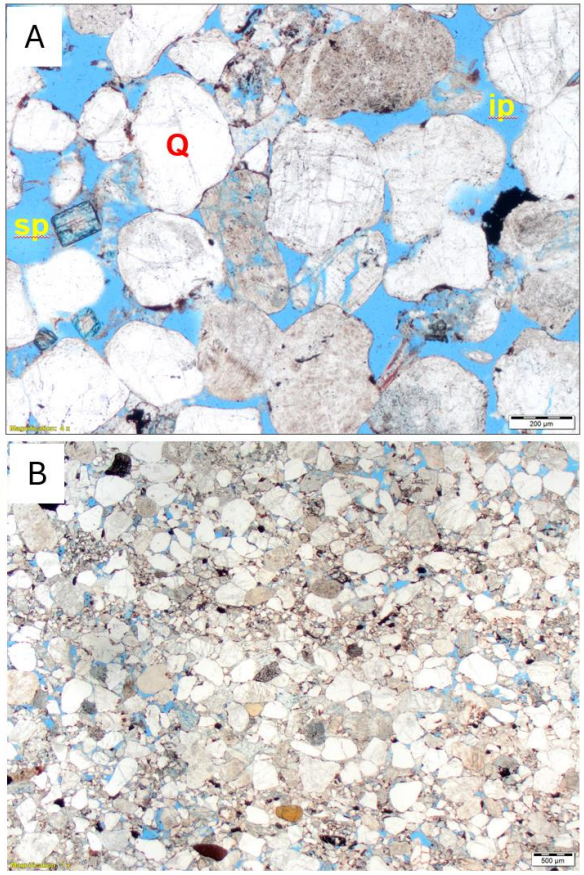

Code	Class
fd	Ferroan Dolomite
ip	Intergranular Primary Pores
o	Oversized pore
Q	Detrital quartz grain
q	Quartz overgrowth
sp	Secondary porosity

A) Plane polarized light image
B) Plane polarized light image

Figure 3-2 **An illustrated summary of the key observations in WYH-01 suggests a mismatch between the RCA data and petrographic data. In Table 1, samples in yellow have a greater visual porosity than the He-porosity, whereas samples in green show too high permeability for the given amount of point-counted visual porosity and calculated microporosity. A) and B) show plan polarized light images illustrating both cases.**

- In EVD-01, the RCA data of some samples do not agree with the thin section observations and XRD data
- The sample with the highest permeability (i.e., at 1841.5m, 189 mD) also has the highest point-counted quantities of detrital clay-rich clasts, muscovite, authigenic illite and kaolinite (red rectangle in Tables 1, 2, and 3 and photomicrograph A). The clay-rich clast (by compactional deformation) and clay minerals have significantly reduced macro-pores, partially substituting these with low permeability micro-pores, thereby strongly reducing porosity and permeability. The XRD whole rock and clay fraction data confirm that the clay- and mica-rich content of the sample. It is unlikely that the sample selected for petrographic analysis could have such high porosity and permeability values.
- In addition, plug samples from below 1843m could not be located in the NAM sample archive (33 samples missing)

Table 1

Sample No.	Depth (m)	Rock Classification (Pettijohn, 1975)	Detrital Components (%)																				
			Quartz		Rock Fragments												Matrix			Accessories			
			Monocrystalline Quartz	Polycrystalline Quartz	K-Feldspar	Plagioclase	Chert	Claystone Intraclast (ductile)	Sandstone/Siltstone	Sedimentary indeterminate	Metamorphic indeterminate	Plutonic	volcanic	Helium Porosity (%)	Horizontal Permeability (mD)		Silt-sized matrix	Dispersed Clay Matrix	Infiltrated Clays	Muscovite	Biotite	Heavy Minerals
1	1802.3	Sublitharenite	55.6	11.6	-	0.41	2.1	0.83	-	-	1.2	-	-	9.8	1.6		-	-	-	-	-	-
2	1809.5	Sublitharenite	56.7	11.7	-	-	1.3	0.67	1.3	0.33	1.3	0.67	-	10.3	2.9		-	-	-	-	-	-
3	1811.5	Sublitharenite	56.3	9.4	-	-	2.0	2.0	1.7	0.33	0.67	1.0	-	10.4	3.0		-	-	-	-	-	-
4	1814	Sublitharenite	46.7	14.3	-	-	2.3	0.33	0.67	0.67	0.33	4.0	-	14.3	95.0		-	-	-	-	-	-
5	1821	Sublitharenite	51.7	11.7	-	-	1.3	0.33	0.67	0.33	3.3	1.0	-	13.2	65.0		-	-	-	-	-	0.67
6	1824.5	Sublitharenite	45.7	12.7	-	-	-	0.33	2.3	0.33	1.3	1.3	-	7.3	n.m		-	-	-	-	-	0.33
7	1828	Sublitharenite	41.0	13.0	-	-	1.7	2.0	2.3	0.33	2.0	2.0	-	20.3	1.6		-	-	-	-	-	0.33
8	1833	Sublitharenite	44.0	14.0	-	-	1.7	3.0	2.0	0.33	1.7	2.0	-	10.0	1.6		-	-	-	-	-	0.33
9	1836	Sublitharenite	51.3	13.7	-	-	2.0	3.7	1.0	0.33	2.0	2.0	-	15.9	32.1		-	-	-	-	-	0.67
10	1841.5	Litharenite	32.0	12.3	-	-	2.3	19.7	1.0	0.33	4.7	0.67	-	16.6	189.0		-	-	-	5.7	-	-
11	1843	Sublitharenite	39.7	18.0	-	-	1.0	3.3	0.33	-	1.7	1.3	-	6.5	n.m		-	-	-	1.0	-	0.67

Table 2

Sample No.	Depth (m)	Rock Classification (Pettijohn, 1975)	Authigenic Components (%)																									Porosity %		
			Pore-Filling																Replacive											
			Bitumen	Non-Ferroan Calcite	Ferroan Calcite	Non-Ferroan Dolomite	PF Ferroan Dolomite	Siderite	Anhydrite	Anhydrite fracture	Barite	Halite	Quartz	Hematite	Pyrite	Illite	Grain-Rimming Illite	Grain-Rimming Chlorite	Kaolinite	Clay (indeterminate)	Non-Ferroan Dolomite	Ferroan Dolomite	Anhydrite	Illite	Chlorite	Kaolinite	Clay (indeterminate)	Intergranular	Oversized pore	Intragranular
1	1802.3	Sublitharenite	-	-	-	-	12.0	-	1.2	-	0.83	-	2.9	-	-	1.7	-	-	2.9	-	-	3.7	-	-	-	1.7	-	1.2	-	-
2	1809.5	Sublitharenite	-	-	-	-	2.7	-	-	-	0.33	-	5.7	-	-	1.3	-	-	2.3	-	-	3.3	-	-	-	3.0	-	5.3	-	2.0
3	1811.5	Sublitharenite	-	-	-	-	2.3	-	-	-	0.33	-	4.3	-	-	1.7	-	-	5.3	-	-	2.0	-	-	-	2.7	-	6.3	-	1.7
4	1814	Sublitharenite	-	-	-	-	1.3	1.7	-	-	-	-	5.3	-	-	3.0	-	-	7.3	-	-	0.67	-	-	-	1.0	-	8.0	-	2.3
5	1821	Sublitharenite	-	-	-	-	1.0	4.0	-	-	-	-	5.0	-	-	5.7	-	tr	4.0	-	-	0.67	-	-	-	3.3	-	3.7	-	1.7
6	1824.5	Sublitharenite	-	-	-	-	2.3	5.0	-	-	-	-	5.3	-	-	8.7	-	tr	6.7	-	-	1.0	-	-	-	1.7	-	4.0	-	0.67
7	1828	Sublitharenite	-	-	-	-	2.0	5.0	-	-	-	-	4.3	-	-	9.0	-	-	4.0	-	-	2.3	-	-	-	1.3	-	6.3	-	1.0
8	1833	Sublitharenite	-	-	-	-	0.67	3.7	-	-	-	-	4.7	-	-	7.3	-	-	3.7	-	-	1.0	-	-	-	2.0	-	6.7	-	1.3
9	1836	Sublitharenite	-	-	-	-	5.7	3.0	3.0	-	-	-	2.0	-	0.33	1.7	-	-	1.0	-	-	4.3	1.3	-	-	0.33	-	0.67	-	-
10	1841.5	Litharenite	-	-	-	-	-	-	-	-	-	-	1.3	-	0.67	11.0	-	tr	2.7	-	-	-	-	-	-	2.3	-	1.7	-	1.7
11	1843	Sublitharenite	-	-	-	-	4.3	6.3	-	-	-	-	5.3	-	1.7	2.0	-	-	4.3	-	-	4.3	-	-	-	3.0	-	1.0	-	0.67

Tr = Trace amounts. Not point-counted

Table 3

Sample	Depth (m)	Whole Rock Composition (%BW)														TOTAL % (Whole Rock)	Clay Fraction			TOTAL % (Clay Fraction)
		Quartz	Illite/Mica	Kaolinite/Chlorite	Microcline	Anhydrite	Albite	Calcite	Ferroan Dolomite	Dolomite	Halite	Pyrite	Barite	Siderite	Hematite		Illite	Chlorite	Kaolinite	
EVD-01_1802.3	1802.3	78	3	13	0	0	0	0	4	2	0	0	0	tr	0	100	23	0	77	100
EVD-01_1811.5	1811.5	81	1	15	0	0	0	0	2	1	0	0	0	0	0	100	7	0	93	100
EVD-01_1821	1821	68	4	26	0	0	0	0	1	1	0	0	0	tr	0	100	56	0	44	100
EVD-01_1833	1833	83	3	13	0	0	0	0	1	tr	0	0	0	tr	0	100	41	0	59	100
EVD-01_1841.5	1841.5	65	20	14	tr	0	tr	0	0	0	0	0	0	1	0	100	89	0	11	100
EVD-01_1824.5	1824.5	81	3	13	0	0	0	0	0	3	0	0	tr	tr	0	100	47	0	53	100

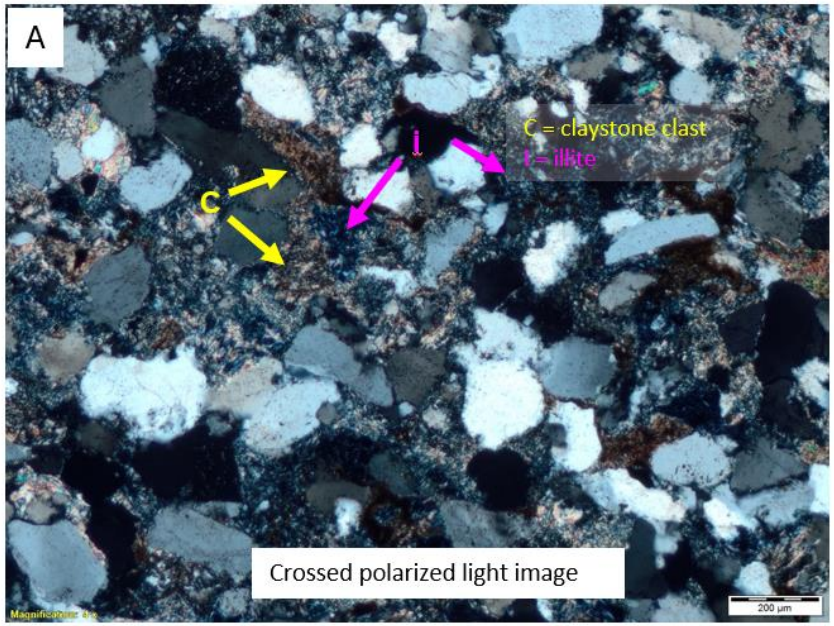

Figure 3-3 Illustrative summary of key observations in EVD-01, which suggests a potential mix-up of archived plug samples occurred, causing a discrepancy between porosity and permeability data, and petrographic observations for some samples Tables 1, 2 and 3 show the quantitative mineralogical data. A) The composition and texture of the highlighted sample in the tables is illustrated by this cross-polarized light image.

3.2.1 XRD Ambiguous/Contradictory Results

There are several wells where XRD results are ambiguous or contradictory when comparing them with point count data. In addition, the results of Whole Rock and Clay-fraction analysis may show significant differences in ratios of illite and kaolinite. It should be noted that XRD analysis is a semiquantitative mineralogical quantification method, the results of which may be influenced by several factors such as sample preparation, clay type and morphology (e.g., grain-coating *vs.* pore-filling), clay crystal size (e.g., kaolinite *vs.* dickite). An unequivocal explanation for the causes of these discrepancies is challenging.

In wells IJD-01, MKN-01, SLB-01, and Q14-02, the relative quantities of illite and kaolinite quantified in the whole rock analysis do not compare well with the ratios observed in the clay fraction data. Generally, kaolinite is more abundant than illite in the whole rock XRD and point count data. In contrast, illite is more abundant in the clay fraction data. This may be due to:

1) kaolinite may often present as tightly compacted, pore-filling aggregates, that may not have fully been disaggregated during sample preparation. The sample preparation for clay fraction analysis aims at separating the <2µm for the analysis by centrifuging an aqueous suspension. The remaining suspension is used for analysis. Consequently, these aggregates may settle out during the centrifuging stage rather than remaining in suspension with the other clay minerals.
2) kaolinite may be present as its polymorph dickite, which has a crystal size that is usually coarser than 2µm. The suspension may have lost its dickite together with the coarser particles during centrifuging.

In the XRD whole rock, ferroan and non-ferroan dolomite proportions may be reported separately (e.g., in well LNH-01). Sometimes, the two types of dolomite are specified individually (e.g., in well MKN-01). The main peaks for both varieties are closely spaced in the XRD diffractogram. When two distinct compositional varieties are present in a sample, it is often possible to quantify these. In the case where zoned crystals with gradually increasing or decreasing Fe-content are present, the peaks are more likely to amalgamate into a broader single peak, from which the ratios are difficult to ascertain (e.g. non-ferroan dolomite cores grade into a ferroan dolomite rim in well HST-02-S1).

3.2.2 Compactional Porosity Loss (COPL) *vs.* Cementational Porosity Loss (CEPL) Cross-Plot

It was determined that the conclusions that may be made from the data shown by the COPL vs. CEPL cross-plot do not always agree with other petrographic observations made in the thin-section analysis. Some examples are presented below:

Well SLD-03

The diagram of CEPL *vs.* COPL (see appendix 12) indicates that compaction was the most important factor in porosity reduction (COPL = 29.8 – 31.8%), with cementation being less important (CEPL = 8.4 – 11.1%). However, this does not agree with the characterization of rigid grain-to-grain contacts. Textural analysis shows predominantly point-to-long and even point-to-floating grain texture in one sample. This suggests relatively weak mechanical compaction. It may indicate a result of overpressure at the time of maximum burial. In addition, a porosity-grain density plot suggests that a heavy cement, likely ferroan dolomite, mainly affects the reservoir properties.

Well MKN-01

Secondary pores are the dominant pore type in the three investigated samples (mean values for relative proportions of pore types are shown in Table 2-4), suggesting that grain dissolution played an important role in partially reversing the effect of compaction on porosity development.

Sample No.	Depth (m)	Porosity %				Core Analysis			Compaction and Cementation (%)		
		Intergranular	Oversized pore	Intragranular	Total visible porosity	Helium Porosity (%)	Horizontal Permeability (mD)	Grain Density (g/cm^3)	Pore filling Cement	COPL	CEPL
1	1698.5	5.7	2.7	6.7	15.0	21.3	151	2.64	14.0	31.5	9.6
2	1702.3	6.0	3.0	7.3	16.3	21.3	40.1	2.66	16.3	29.2	11.6
3	1705.2	5.3	4.3	4.0	13.7	23.1	2971	2.66	14.3	31.5	9.8

Table 3-1 **Overview of relative amounts by point-counting of pore types and total pore-filling cements, and COPL and CEPL values and reservoir quality data in well MKN-01**

Point-counted percentages of different pore types and total visible macro-porosity are similar for all three samples as are the helium porosity values (cf. Table 3-1). However, the permeability values for samples 1 and 2 compared to sample 3 are very different. The strong permeability contrasts between the samples cannot be explained from the point-counted values.

4 Conclusions

Core Description

- The Slochteren Formation occurs in the study area as a continuous sandstone package locally exceeding 200m thickness. The sandstones are predominantly deposited in aeolian settings except for thin intervals of fluvial deposits that were mostly encountered at the base of several cores that reached or ended in close proximity to the base of the Slochteren Formation.
- The aeolian intervals were mostly deposited in Dry Aeolian Sandflat/Interdune, Aeolian Dune Base, and Aeolian Dune Slip-face sub-environments. They are characterized by fine, medium and coarse-grained sandstones that often exhibit bimodal grain-size lamination. Thin interbeds of wavy laminated Damp Aeolian Sandflat deposits were observed in a few wells only. The fluvial deposits consist of planar laminated to cross-bedded sandstones, pebbly sandstones, conglomerates and occasional intercalated mudstone interbeds. These intervals are interpreted to represent Braided Channel deposits
- At the core scale, a wide range of mainly cemented deformation features are observed, ranging from small-scale faults to anastomosing deformation bands and conjugate cemented fractures. Small-scale faults and cemented fractures are most abundant while deformation bands are occasionally present (e.g. wells HEW-01-S1 and WYH-01). No relationships between fracture type and density in response to depositional facies or mean porosity could be established.

Petrography & Diagenesis

- Most of the analysed samples are classified as sublitharenites. Detrital quartz is the dominant framework component, with sedimentary and metamorphic rock fragments variably occurring in subordinate amounts across wells. Feldspars have been recognized in some wells, being partially leached to almost completely dissolved and recognisable only by the shape of grain moulds and remnants aligned to former crystal planes.
- The complex and diverse burial histories across the study area affected diagenetic evolution to the extent that compaction, cementation, and grain dissolution triggered that reservoir properties that are highly varied texturally and compositionally.
- The degree of compaction was assessed from the nature of rigid grain-to-grain contacts and by applying the COPL-CEPL method (Lundegard, 1992), a point count-based approach to determine the relative contributions to intergranular porosity loss of compaction and cementation. The latter method shows that compaction was the most important factor. However, it does not show a good correlation with reservoir quality. Evaluation of the nature of grain contacts shows more distinct variations in compaction, from weak (point and long grain contacts) to strong (concavo-convex to sutured and occasionally stylolised) due to pressure solution. This method shows, with some exceptions, a moderately good correlation with reservoir quality.
- Ferroan dolomite and quartz cements, and to a lesser extent anhydrite and siderite cements are commonly occurring blocky cements, while the authigenic clay mineral assemblage may consist of kaolinite (at least two generations) and replacive and pore-filling illite (three habits). Wells with pore-filling/bridging illite or exhibiting well-developed illite grain-rims generally show impaired permeability.

Grain dissolution occurred at various times. Early grain dissolution led to the formation of secondary pores that were most often occluded by replacive illite, kaolinite, and/or blocky cements. Late grain dissolution has led to secondary pores that may have remained open or

were only partially occluded by subsequent authigenic minerals. Extensive grain dissolution is in a few wells associated with the presence of the authigenic mineral dawsonite, which is known to form under conditions of high CO_2 pressure.

Reservoir Quality

- Reservoir quality is highly variable throughout the study area. Legacy routine core analysis data (helium porosity and horizontal permeability) were available for 28 study wells. Mean values for both entities were calculated and cross-plotted with 95% confidence intervals. Mean values range from 3.4% and 0.01mD (i.e., well ERM-01-S1) for the well with the lowest reservoir quality to 26.7% and 1032mD (i.e., well LNH-01). It should be noted that many cores only sampled a small portion of the Slochteren Formation, so reservoir quality data may not be fully representative.
- The depositional environment exerts limited control on reservoir quality. Exceptions are noted in the individual well reports (e.g., well WGF-01). This likely reflects the limited variation in depositional settings dominated by “dry” aeolian processes. Generally thin, fluvial sandstones and conglomerates occur in a few wells in the eastern part of the study area. RCA measurements were available for one well only (8 samples). Although slightly lower in reservoir quality compared to samples from the overlying aeolian interval, reservoir quality was poor overall, so any differences appear to be irrelevant.
- Reservoir quality is governed by a range of diagenetic processes owing to the analysed samples' variable geological and tectonic histories. Amongst these, compaction, cementation and grain dissolution processes play a dominant role. Blocky cements have locally led to a significant reduction in pore space, while in other instances, pore-filling illite correlates with a horizontal permeability decline of 1.5 to 3 orders of magnitude, with limited impact on helium porosity values. Extensive late grain dissolution is likely responsible for enhancement of reservoir quality.
- Influence of the (Zechstein) transgression: The Weissliegend facies, occasionally observed at the top of the Slochteren Formation (10 - 50m) exhibits reduced reservoir quality. Due to limited sampling of Weissliegend intervals, no unique cause for reservoir impairment could be established. Grain-rimming dolomite and quartz cementation were observed in two wells, while anhydrite cementation was dominant in another well.
- Dawsonite: A key finding of this Legacy core project is the presence of dawsonite, an authigenic mineral rarely reported in the Dutch Rotliegend. The occurrence of dawsonite is associated with good reservoir quality due to enhanced grain dissolution and the creation of oversized pores, most likely related to elevated pore water acidity from CO_2 rich fluid migration
- A majority of wells located on the Friesland, Noord-Holland & Groningen Platforms and the Texel-IJsselmeer High and the northern edge of the Central Netherlands Basin exhibit good reservoir quality (porosity >18% and permeability >50mD) likely due to the lack of deep burial and/or secondary porosity generation. On the contrary, wells located in the West (WNB) and Central (CNB) Netherlands basins exhibit relatively low reservoir quality. Reservoir quality in the Central Netherlands Basin varies, but authigenic illite is noted to be the common negatively affecting diagenetic feature. Wells in the West Netherlands Basin consistently exhibit very low reservoir quality (less than 20mD) due to strong grain compaction.

5 References

Adams, A.E., MacKenzie, W.S., 1998. A Clour Atlas of Carbonate Sediments and Rocks Under the Microscope. Manson Publishing.

Fossen, H., Schultz, R.A., Shipton, Z.K., Mair, K., 2007. Deformation bands in sandstone: a review. J. Geol. Soc. Lond. 164, 753–769.

Fryberger, S.G., Knight, R., Hern, C., Moscariello, A., Kabel, S., 2011. Rotliegend Facies, Sedimentary Provinces, and Stratigraphy, Southern Permian Basin Uk and the Netherlands: A Review with New Observations, in: Grötsch, J., Gaupp, R. (Eds.), The Permian Rotliegend of the Netherlands. SEPM Society for Sedimentary Geology, p. 0. https://doi.org/10.2110/pec.11.98.0051

Gaupp, R., Okkerman, J., 2011. Diagenesis and Reservoir Quality of Rotliegend Sandstones in the Northern Netherlands—A Review, in: SEPM Special Publications. pp. 193–226. https://doi.org/10.2110/pec.11.98.0193

Goldberg, T., Koenen, M., Nelskamp, S., Vandeweijer, V., 2017. Conceptual diagenetic models for cementation in Rotliegend sandstones (No. 060.16733 (TEG0114003)).

Hellevang, H., Kvamme, B., Aagaard, P., 2004. Long term interactions between minerals and reactive fluids -- Stability of dawsonite. Proc. 4th Annu. Conf. Carbon Capture Storage Paper B.

Kombrink, H., Doornebal, J.C., Duin, E.J.T., Den Dulk, M., Van Gessel, S.F., Ten Veen, J.H., Witmans, N., 2012. New insights into the geological structure of the Netherlands; results of a detailed mapping project. Neth. J. Geosci. Geol. En Mijnb. 91, 419–446.

Lundegard, P.D., 1992. Sandstone Porosity Loss, A “Big Picture” view of the importance of compaction. J. Sediment. Petrol. 62.

Mijnlieff, H., van Ojik, K., Nortier, J., Okkerman, J., Gaupp, R., Grötsch, J., 2011. The Permian Rotliegend of the Netherlands: Appendix B Core Atlas., in: The Permian Rotliegend of the Netherlands, SEPM Special Publication 98. pp. 281–371.

Ojik, K. van, Böhm, A.R., Cremer, H., Geluk, M.C., Jong, M. de, Mijnlieff, H.F., Nio, S.D., 2011. The rationale for an integrated stratigraphic framework of the upper rotliegend II depositional system in The Netherlands.

Peacock, D.C.P., Nixon, C.W., Rotevatn, A., Sanderson, D.J., Zuluaga, L.F., 2016. Glossary of fault and other fracture networks. J. Struct. Geol. 92, 12–29. https://doi.org/10.1016/j.jsg.2016.09.008

Pettijohn, F.J., Potter, P.E., Siever, R., 1987. Sand and Sandstone. Springer-verlag.

Reijers, T.J.A., Mijnlieff, H.F., Pestman, P.W., Kouwe, H.F., 1993. Lithofacies and Their Interpretation: A Guide to Standardised Description of Sedimentary Deposits. Meded. Rijks Geol. Dienst 49, 1–55.

TNO, 2015. Integrated pressure information system for the onshore and offshore Netherlands (No. R10056).

Vincent, B., Waters, J., Witkowski, F., Daniau, G., Oxtoby, N., Crowley, S., Ellam, R., 2018. Diagenesis of Rotliegend sandstone reservoirs (offshore Netherlands): The origin and impact of dolomite cements. Sediment. Geol. 373, 272–291. https://doi.org/10.1016/j.sedgeo.2018.06.012

•

6 Methods

6.1 Core Description

Sedimentological core description was performed on the legacy cores at the core storage facilities of TNO in Zeist and NAM in Assen. The data were digitally recorded as a composite core/log data sheet using the Windows-based CoreCAD© module of the WellCAD™ application. The resulting descriptive data are presented as WellCAD™ panels at 1:20 scale[7], combined with selected wireline logs (Gamma-ray, Caliper, Bulk Density/Neutron Porosity or Sonic travel time, if available) and routine core analysis data. Core and core box intervals, core-to-log shift (if possible) and continuous core photographs (if present) are also included.

WellCAD panels are included in the individual well reports and available on NLOG as native WellCAD format files (*.wcl). The latter can be viewed and printed at different vertical scales using WellCAD Reader software (available at https://www.alt.lu/download/). Displaying the files at 1:5 or 1:10 scale provides a realistic rendering of the core photographs included in the panels.

6.1.1 WellCAD Panel Layout and Logged Parameters

A graphical example of the WellCAD panel header, including data column headers, is shown in Figure 6-1. The panels are in most cases plotted at 1:20 vertical scale and occasionally at 1:50 scale. The following parameters were recorded and included in the panels:

- Relevant wireline logs (if available)
- Graphical representation of routine core analysis data (He-porosity, permeability and grain density)
- Core and box number, core photos, and apparent dip (where relevant)
- Sedimentology: core condition, rock colour, grain-size (mode and maximum), main sedimentary structure, lithology, physical structures, lithological accessories, sorting, visual estimation of porosity, fractures and their intensity (when relevant), visible cements, and occurrence of pale intervals
- Lithofacies codes and interpreted depositional sub-environments
- Petrographic sample locations differentiated to specific type (thin-section, SEM/BSEM, XRD)
- Descriptive comments

Fracture types were not differentiated in a consistent manner. Where fractures were very common, a histogram-style intensity column was used.

The “pale intervals” column was inserted to express the intensity of the “patchy” bleaching of the sandstones, as it was expected to occur frequently. Ultimately, only a few wells exhibited this type of bleaching (e.g. well SLB-01).

[7] WellCAD panels for longer cores in individual well reports may have been supplied at 1:20 and 1:50 scale, or 1:50 scale only.

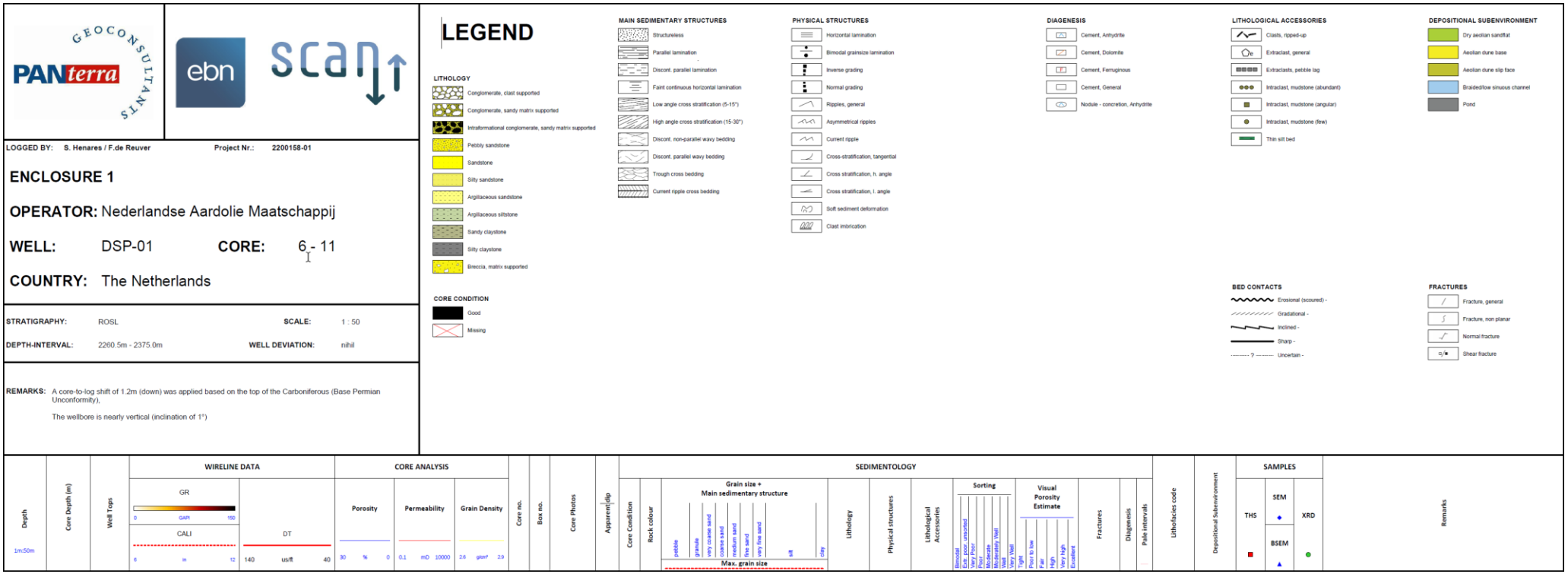

Figure 6-1 Layout of the WellCAD main header and data column headers.

6.1.2 Lithofacies and Depositional Sub-Environment

Lithofacies codes were assigned bed-by-bed based on the lithological composition, dominant grain-size, and main sedimentary feature. Chapter 6.1.3 provides a detailed explanation of the applied lithofacies classification scheme and an overview of the most commonly used lithofacies codes.

Lithofacies are interpreted in terms of the depositional process involved in their formation. The approach taken in this study is to link lithofacies directly to depositional sub-environments, which is similar to many other studies on Rotliegend deposits in the Dutch subsurface. It was also adopted in Appendix A of SEPM Special Publication 98, The Permian Rotliegend Of The Netherlands (Mijnlieff et al., 2011). A flowchart aiding in the interpretation of depositional sub-environments based on lithofacies characteristics is presented in Chapter 6.1.4, Figure 6-2.

6.1.3 Lithofacies Classification Scheme

The lithofacies coding scheme[8] used in this study is based on a classification scheme published by the Rijks Geologische Dienst (Lithofacies and their interpretation: a guide to standardised description of sedimentary deposits - (Reijers et al., 1993).

This publication emphasises that successful analysis of sedimentary deposits depends on easily comparable results. Therefore, ideally a sediment description should be:

- simple
- objective
- repeatable
- comprehensive
- independent of scale

The proposed (coded) lithofacies in its most extensive form contains the following descriptive parameters:

- lithology
- bedding
- sedimentary structures
- texture
- colour
- paragenesis of diagenetic products
- basic palaeontological data

A systematic definition of a sediment along above lines yields a "lithofacies". Lithofacies are the basic "building blocks" of sediment description.

In the current study, the lithofacies classification scheme is restricted to the first three descriptive parameters. It includes, in a few cases, information on lithological accessories if thought relevant for the interpretation. Lithofacies are coded in the following way: one or more descriptors (upper case letters) are used to describe the lithology of the facies, often accompanied by a number (e.g. 1-5) to indicate grain-size or clast size (see table below).

[8] Lithofacies codes comprise a lithology qualifier separated by a comma from a main sedimentary structure code. S stands for sandstone, while the numbers 1 through 5 indicate the modal grain-size ranging from very fine to very coarse. In the case of two lithology codes, a "." (period) used as a separator indicates admixed lithologies while "/" (forward slash) indicates interbedded lithologies, e.g. S2.S3 and S2/S4). Sedimentary structure code m = structureless, lp = planar laminated, xl = low-angle cross-laminated, xh = high-angle cross-laminated, w = wavy laminated. The "addition of a "b" indicates that the core exhibits bimodal grain-size lamination (e.g., lpb).

Lithology Code	Description
M	Claystone
J	Siltstone
S1	Very fine-grained sandstone (62.5-125µm)
S2	Fine-grained sandstone (125-250µm)
S3	Medium-grained sandstone (250-500µm)
S4	Coarse-grained sandstone (500µm-1mm)
S5	Very coarse grained sandstone (1-2mm)
CE	Extraclast conglomerate
CI	Intraclast conglomerate

In the case of admixed or interbedded lithologies, two (or more) lithology codes are separated by a "." (period) or "/" (forward slash) to indicate whether the second lithology respectively is admixed or interbedded. The second listed lithology is subordinate (20-50%). It is omitted from the code if it constitutes less than 20% of the composition. For conglomeratic deposits, a lower limit of 10% is used. Examples of mixed lithology codes are shown in the following table:

Lithology Code	Description
M.J	Claystone, admixed with silt
M/S1	Claystone interbedded with very fine grained sand
S1/S3	Very fine grained sand interbedded with medium grained sand (often used for bimodal grain-size lamination
S5.CE	Very coarse grained sandstone admixed with pebble extraclasts (10-50%)
CE.S4	Conglomerate with coarse sandy matrix (20-50%)

Sedimentary structures are added in lowercase letters, separated by a comma from the lithology code(s). If needed, two or more descriptors may be used. However, in this study a maximum of two descriptors were used. Commonly used codes are shown in the following table:

Structure	Description
m	Structureless
dc	Contorted/convolute lamination
w	Wavy lamination
wi	Irregular lamination
wnb	Non-parallel wavy lamination, with bimodal grain-size lamination
rc	Current ripples
l	Faintly laminated
lp	Parallel (horizontal) lamination
lpb	Parallel (horizontal) lamination, with bimodal grain-size lamination
xl	Low angle cross lamination (5-15°)
xlb	Low angle cross lamination (5-15°), with bimodal grain-size lamination
xh	High-angle cross-lamination (15-30°)
xf	Through (festoon) cross-lamination
xhf	High-angle trough (festoon) cross-lamination
xhb	High-angle cross-lamination (15-30°), with bimodal grain-size lamination
xt	Tangential cross-lamination
xht	Tangential high-angle cross-lamination
xhtb	Tangential high-angle cross-lamination, with bimodal grain-size lamination

Lastly, in a few cases, a code for lithological accessories was added where it was thought relevant for the sedimentological interpretation. These codes are (separated by a comma from the preceding codes) Gim and Gic. The latter code was erroneously used and should be exchanged with Gim, representing "mudstone intraclasts". Examples of full descriptive lithofacies codes are:

S3,xh	High-angle cross-laminated, medium-grained sandstone
S2/S4,xlb	Low-angle cross-laminated, fine – coarse grained sandstone, bimodal lamination
S4,xf,Gim	Trough cross-laminated sandstone, with mudstone intraclasts

6.1.4 Interpretation of Sub-Environments

As described in Chapter 6.1.2, lithofacies are interpreted in terms of the depositional process involved in their formation. The approach taken in this study is to link lithofacies directly to depositional sub-environments. A flowchart (Figure 6-2), developed in-house by PanTerra, was used to aid in interpreting sub-environments based on the sedimentary characteristics of individual beds (lithofacies). An intermediate step applied in earlier studies was to combine lithofacies with common characteristics, excluding grain-size into lithofacies groups. The lithofacies group codes would be displayed in a separate column in the core description log. This intermediate step was not applied in this study. Consequently, the associated lithofacies group acronyms are greyed out in Figure 6-2.

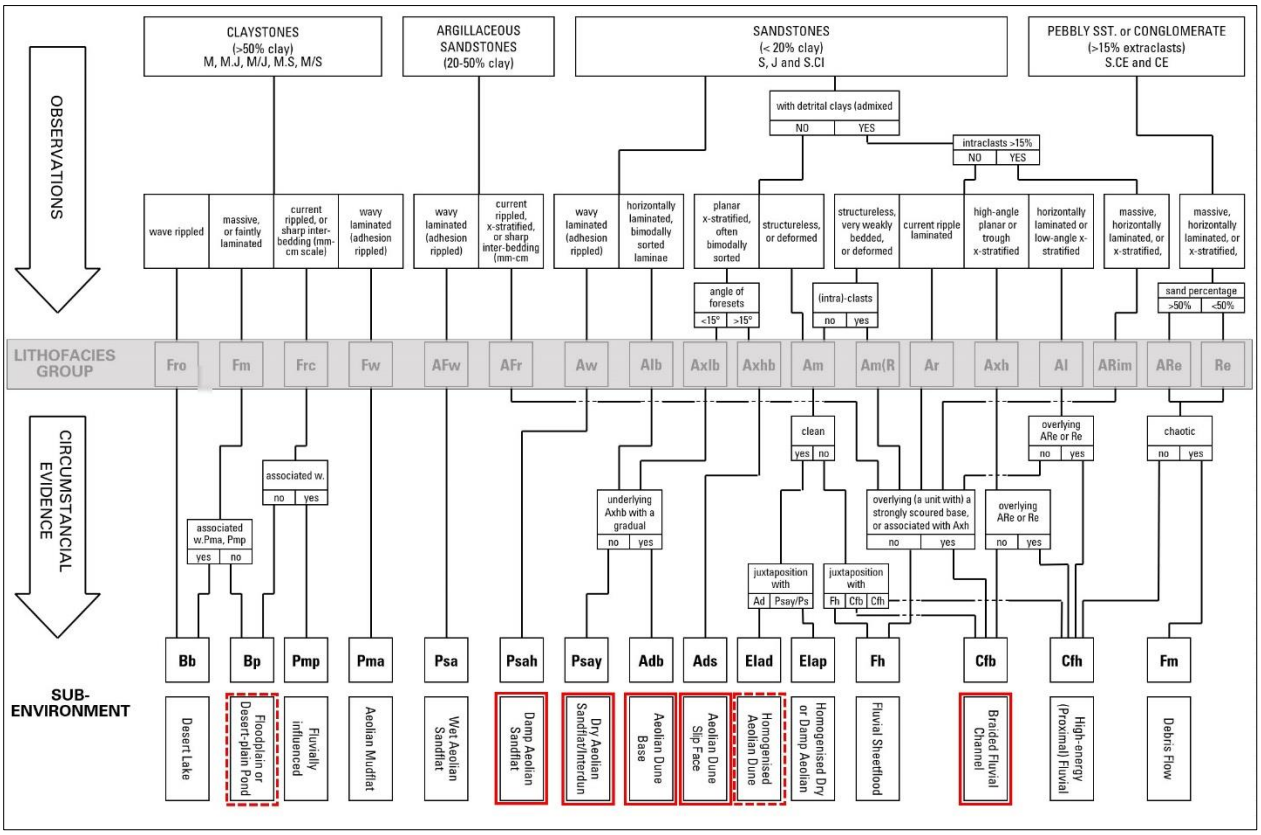

Figure 6-2 Flowchart to aid in the interpretation of depositional sub-environments based on lithofacies characteristics. Sub-environments encountered in the studied cores are outlined with red rectangles (dashed rectangles represent minor occurrences). The intermediate step of identifying lithofacies groups (greyed-out in diagram) was not applied in this study.

6.1.5 Limitations of the Grain-size Descriptive Attribute

Grain-size is recorded as a sedimentary attribute. Determining the modal grain-size is a challenging task. The core description in aeolian Rotliegend deposits is generally performed on a bed-by-bed basis, where beds may be defined by a single cross-bed set that may vary in height from 10cm up to 6m or more (large-scale aeolian dune bedforms). Grain sizes within these bedforms often vary on millimetre to decimetre scale with random frequency. It is, therefore, difficult to make an objective (in terms of bed resolution) and repeatable subdivision based on grain-size variations within these bedforms.

Similarly, in the case of bimodal grain-size lamination, it is difficult to determine the modal grain-size. Within a bed, the dominant grain-size may, for example, vary within short distances from very fine-grained interlaminated with coarse-grained sand to dominantly medium-grained and interlaminated with fine- or very fine-grained sand. Unlike water-laid sands, where grain-size is generally more uniform within a bed

due to more uniform energy conditions in the formation of specific bedforms, this may not be the case in aeolian depositional processes where wind velocities can vary considerably at different time scales, influencing the ability to transport sand with different grain sizes.

For intervals with bimodal grain-size lamination, the grain size for the coarser laminae is represented in the WellCAD core description panel by the maximum grain-size curve (red dashed curve). The grain-size for the finer-grained laminae is represented by the modal grain-size curve (black curve bounding the sedimentary structure column). The finer of the two grain sizes is listed first. The order is not indicative for the relative dominance of either grain-size class.

6.1.6 Modelling of Apparent Dips of Sedimentary Surfaces in Cores from Deviated Wells

Interpretation of apparent dip angles in core slabs from wells with inclined wellbores at coring depth is challenging in continuous sandstone sections without shale/mudstone breaks or other reliable surfaces that were horizontal at the time of deposition. Consider as an example, a bedding plane (i.e. its projection on the slabbed core surface) showing an apparent dip[9] of 15° in the core from a wellbore with a 15° inclination. A plane that is horizontal in the subsurface, would exhibit an apparent dip of 15° in the core, but so would a plane that is dipping at 30° in the opposite direction of the well bore deviation. It can be imagined that in cross-bedded sandstones with variable foreset dip directions, it will be very difficult to orient the slabbing surface in such a way that it aligns with a single plane in the subsurface. Without having a clear understanding on which bedding planes represent planes that were initially horizontal at the time of deposition, it becomes quite difficult to interpret the in-situ (subsurface) orientation of other sedimentary surfaces. In certain situations, however, it is possible to constrain the range of possibilities. The section below presents an example from well Jutphaas-1 (JUT-01). Similar considerations apply to other deviated wells, such as MID-103-S1, WAS-23-S2 and HST-02-S1. These are discussed in the individual well reports. Determination of the original primary dip angles from apparent dips was not always possible (e.g. well MID-103-S1), while in two other wells, dipmeter data were used in support (WAS-23-S2, HST-02-S1).

Jutphaas-1 Apparent Dips

The core slabs of JUT-01 contain several bedding planes that must represent initially horizontal planes at the time of deposition (mudstone bedding planes). The well is deviated at 17°/007° (inclination/azimuth). A structural dip 25/185 is inferred from dipmeter data in a section overlying the Slochteren Formation. Modelling is stereonet projection software indicates that with these orientations of the wellbore and structural dip, initially horizontal bedding planes are expected to show an apparent dip of 8°, whereas the observed apparent dip angle in core is 17° (see Figure 6-3, B).

Apparent dip angles of intervals interpreted as high-angle cross-laminated are up to 30°, thus only showing a difference of up to 13° relative to the apparent dip of initially horizontal beds (argillaceous siltstones). This difference may not necessarily be the maximum dip-angle between horizontal lamination and cross-lamination. The dip direction of the planes with high-angle apparent dips in the core may not (and likely do not) have the same azimuth as the structural dip.

[9] Generally, when cores are slabbed, they are oriented relative to the saw blade in a way that maximises the apparent dip angle in the slabbed surface.

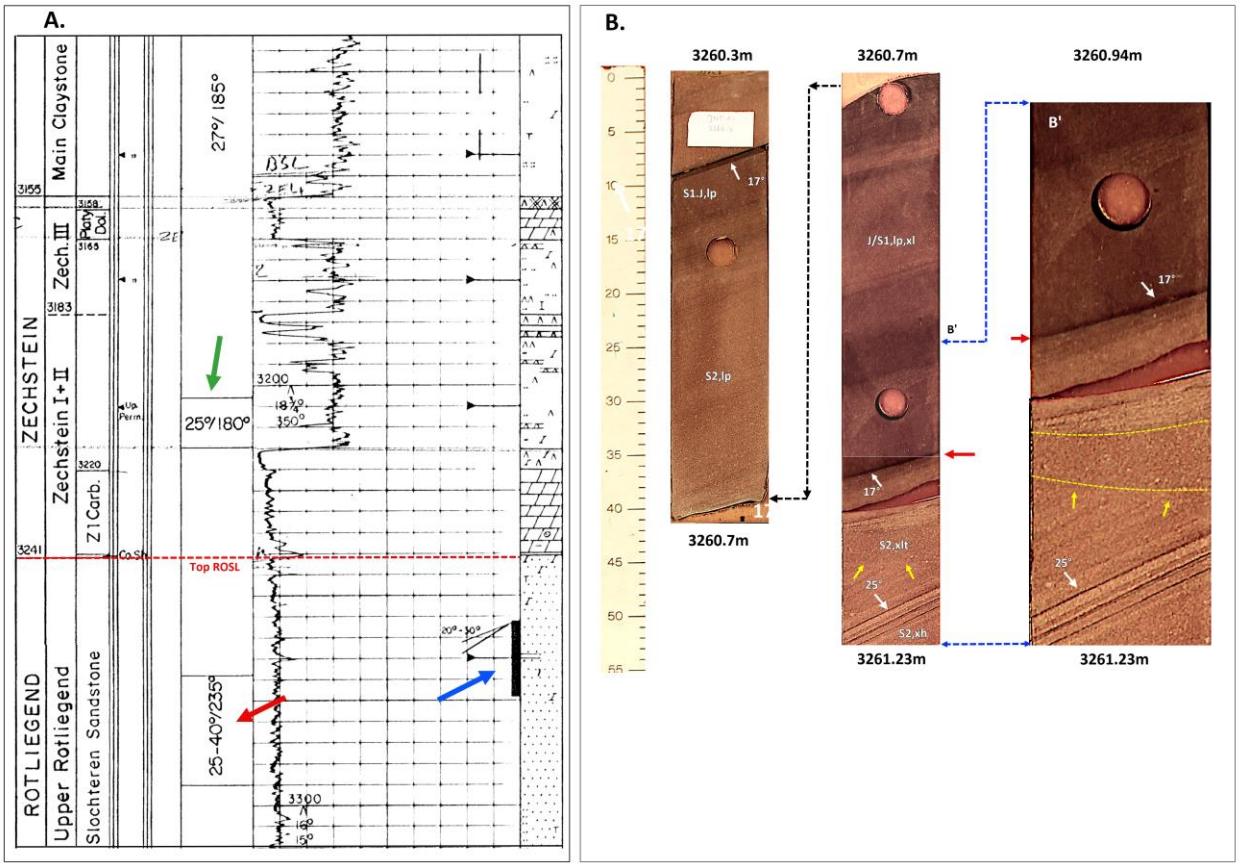

Figure 6-3 **Composite well log, with dipmeter results (A.) and core photos of very fine-grained argillaceous silt/sandstones (B.). In a configuration where the structural dip-angle is 25°/180° (indicated by the green arrow) and the borehole is oriented at 17°/007°, beds that were originally deposited horizontally should show an apparent dip of just 8° in the core. However, a dip of 17° is actually observed.**

For the modelling exercise, it is assumed that the argillaceous siltstone beds in the core were originally deposited in a horizontal orientation. Therefore, the true dip and azimuth of these beds should reflect the current structural dip of the Slochteren Formation near well JUT-01. Since the apparent dip of these beds in the core is 17°—the same as what would be observed in a wellbore deviated at 17° that intersects beds that are currently horizontal—it may be tempting to conclude that these argillaceous siltstone beds are indeed flat-lying. However, a structural tilt of 34° to the north could also produce apparent dips of 17° in core. In fact, the structural dip could have various orientations, as long as the angle with the wellbore axis is 73°.

To determine the orientation of planes that produce apparent dips of 30° in the core, it is essential to know the structural dip direction. Several known parameters can be used, such as the apparent dip angle produced in the core by laminations aligned with the structural dip and the 30° apparent dips observed for sedimentary laminations. Additionally, it can reasonably be inferred that the 30° inclined laminations represent cross-bedding, as these laminae are sharply truncated by an erosive event (at 3261.0m – see Figure 6-3, B), likely of fluvial origin. The thick section of uninterrupted, primary-inclined laminations in the core's lower part is interpreted as part of a large-scale aeolian dune. Given that the dominant aeolian transport direction during the Upper Permian was towards the southwest (with winds coming from the northeast), a primary dip direction for the laminations that produced these apparent dips that would significantly differ from the southwest would be unlikely.

The dominant aeolian transport direction in the Upper Permian was towards the SW (NE wind direction). Considering the scale of the aeolian dune interval, a dip direction that would be significantly different from being southwest-oriented would be illogical.

The modelling exercise was started by testing four cases with different structural dip directions, approximately 90° apart and with a constant 17° dip, assuming that the apparent dip of horizontal lamination observed in the core represents the structural dip-angle.

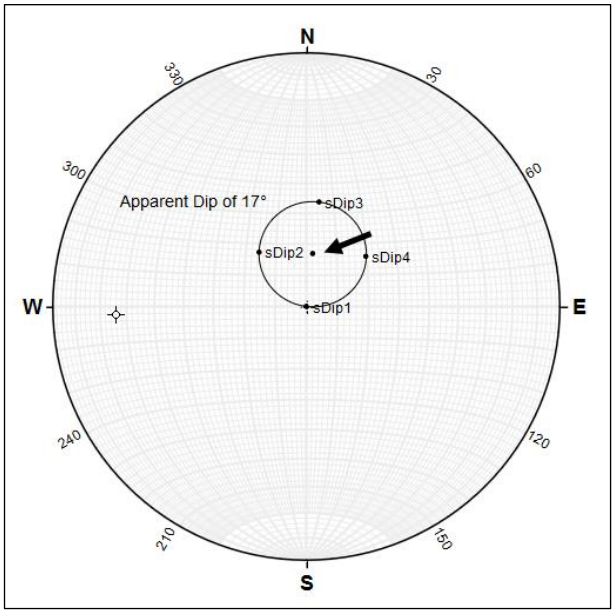

Figure 6-4 This figure shows four poles on a small circle with a width of 17°. The planes associated with these poles represent different structural dip planes that would produce apparent dips of 17° in a core in well JUT-01.

1) A small circle with a width of 17° is drawn in a stereonet centring around the point representing the wellbore (black arrow in diagram 1). Any pole on this small circle would represent a plane intersecting the wellbore at an angle of 73° (90° minus 17°) and produce an apparent dip of 17° in the core. Four poles were plotted on this small circle distributed at 90° relative to each other on the small circle. These poles represent four random structural dip planes with different azimuths. One of these poles plots right in the centre of the stereonet diagram since a horizontal plane in the subsurface would exhibit an apparent dip of 17° in the core. Another pole may be plotted 17° north of the point representing the wellbore and would represent a plane with a dip of 34° (17° wellbore deviation plus 17° structural dip). The orientations of the structural dip planes associated with these four poles are (formatted dip- angle/dip direction) 0/000 (horizontal), 23/139, 35/187 and 25/230. Three of these planes have structural dips between 0° and 25°. The fourth has a dip-angle of 34°, which is an unrealistic value for the structural dip in the area of well JUT-01.

Small circles with a width of 25° degrees were drawn around the poles associated with these three remaining structural dip planes. This angle is an assumed primary dip-angle of aeolian foreset laminations. Any poles plotted on these circles would represent planes dipping at 25° relative to the plane of the structural dip. Figure 6-5, A illustrates the case of a structural dip plane oriented 25/230, with the small circle centring around the pole associated with this plane.

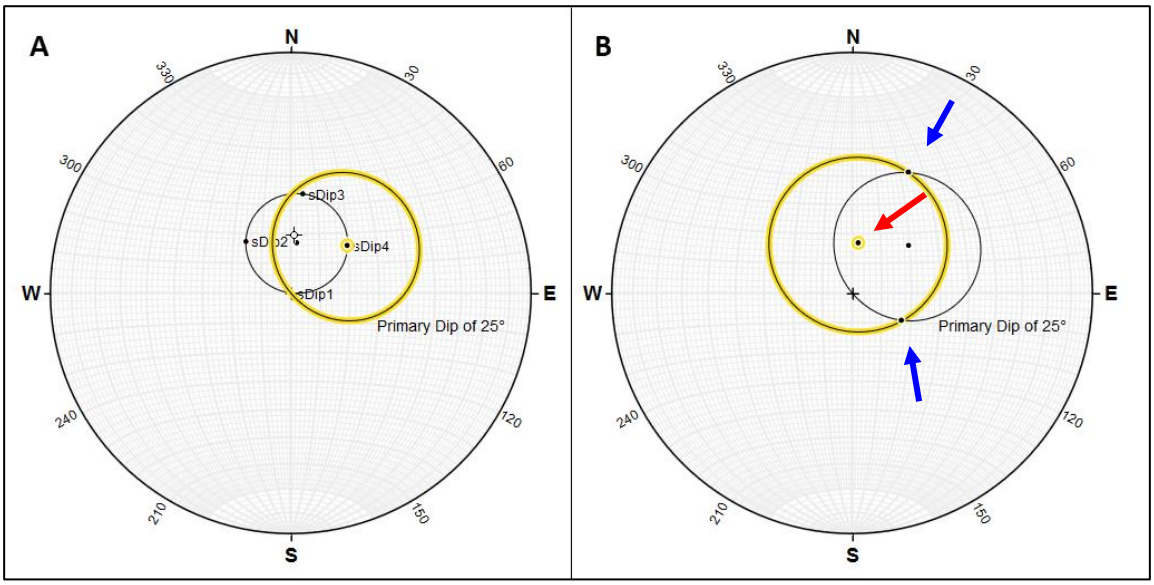

Figure 6-5 **Diagram A shows a small circle (yellow highlighted) on which poles to all theoretical sedimentary planes would plot, which have primary dips of 25° at a structural dip of 25/230 (dip/azimuth). Diagram B shows a highlighted small circle with a width of 30°. The poles of theoretical planes producing apparent dips of 30° in core would plot on this circle (see explanation in paragraph 30).**

2) The next step is to draw a small circle with a width of 30° centring around the point in the diagram that represents the wellbore. This angle is the highest apparent dip-angle observed in the core. Any pole positioned on this small circle would represent a plane intersecting the wellbore at an angle of 60° and producing an apparent dip angle of 30° in core. The two small circles have two intersection points. The poles through these points represent planes that exhibit an apparent dip in the core of 30° **and** have a dip-angle of 25° relative to the structural dip. These poles are the only two solutions that satisfy both requirements for the case of a structural dip of 25/230.

3) The final step is to rotate these poles in order to remove the structural dip. We should then obtain the azimuths of two potential planes representing cross-lamination in their initial orientation at the time of deposition. After rotation using a value for the structural dip of 25/230, the two planes have orientations of 25.5/183 and 25/004 , i.e. south and north-oriented cross-lamination planes. These are unlikely orientations for aeolian dune foresets, hence this solution is rejected.

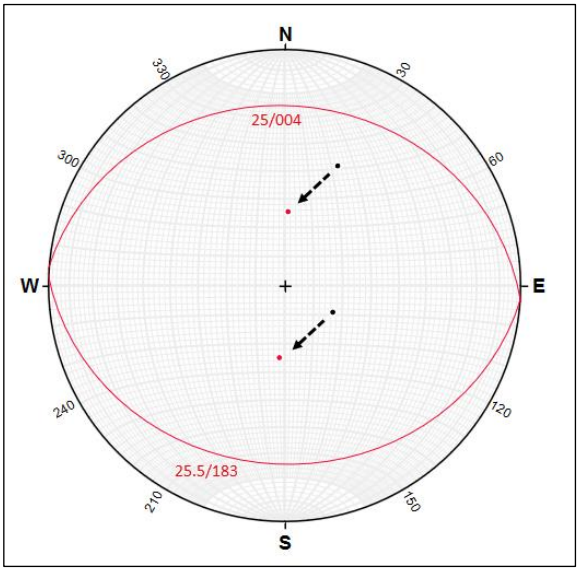

Figure 6-6 Position of poles after rotation to correct for structural dip of potential planes representing cross-bed lamination. Two planes with orientations 25.5/183 and 25/004 are unlikely solutions.

4) Modelling of other scenarios (i.e. with different values for the structural dip) resulted in two values for structural dips that obtained credible results for the orientation of cross-bedding foresets in the well. The results of using a structural dip of 11/258 is shown in Figure 6-7. This orientation lies somewhere between horizontal and a dip of 25/230 (as shown in Figure 6-5 and Figure 6-6). This scenario yields primary dips for cross-bedding with orientations for 26/061 and 24/241 (see). The first solution is rejected as this is an unlikely orientation in the Slochteren Formation. Solution 2, however, fits very well with the established dominant paleo-wind direction during Slochteren times.

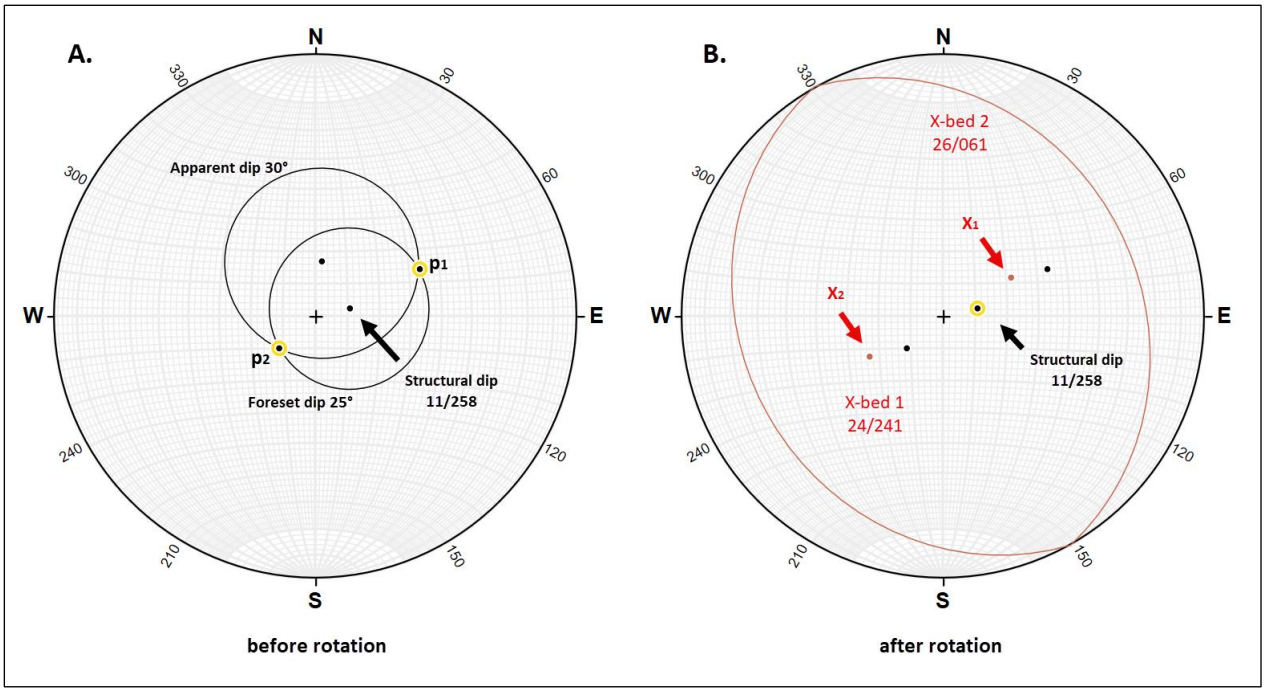

Figure 6-7 A. Configuration of small circles and intersection points resulting in two possible solutions for poles to cross-lamination planes in present-day orientation. B. Poles p1 and p2 after correction for structural dip.

The results from the tests (simulations) with 4 initial structural dip cases are shown in Table 6-1. This table also shows the outcomes of two additional structural dip cases.

Case	Structural dip	Solution 1 Uncorrected	Solution 1 Struct. dip corrected	Solution 2 Uncorrected	Solution 2 Struct. dip corrected
1	0/000	25/278	25/278	25/097	25/097
2	23/139	16/060	25/359	45/162	25/180
3	35/187	42/148	25/097	41/227	25/210
4	25/230	46/204	25/183	19/299	25/004
5	11/258	25/048	25/061	36/246	25/241
6	17/247	41/229	24/218	23/001	25/038

Table 6-1 **Results of apparent modelling (data format is dip/dip direction). Cases 1 – 4 are based on the randomly chosen structural dips described in step 1). Each scenario yields two valid poles that, after rotation for the structural dip assumed in each case, yield values for possible initial primary dips for cross-bed laminae. Accepted solutions are yellow-shaded. Rejected solutions are shaded in grey.**

Case 3 is rejected as the structural dip-angle of 35° is considered unrealistic. The three other structural cases 1, 2 and 4 use structural dips of 25° or less. Case 1 (structural dip of 0°) yields one solution that would fit within an acceptable margin to a SW-oriented paleo-transport direction, which is a plane a plane dipping at 25° to 278°. The other solution, a plane dipping at 25° to 097° is rejected.

The modelling was extended by adding two more structural dip configurations, one with a dip of 11/258 and a second with a dip of 17/247 (Cases 5 and 6). Both also yield acceptable solutions for cross-bed orientations. The three acceptable solutions are highlighted in yellow. At these structural dips yielding the 30° apparent dip-angles observed in core may represent cross-bedding planes with orientations between southwest and slightly north of west (between 218°and 278°). Other solutions are rejected as they have orientations that do not conform to the commonly observed orientations of cross-bed laminae in the Slochteren Formation.

The proposed range of structural dips that result in plausible cross-bedding orientations meets several criteria:

1. Cross-bedding planes with dip directions between 277° and 218° are in agreement with the known SW-oriented aeolian transport direction during deposition of the Slochteren Formation.
2. A depth map of the Base Slochteren, generated with the DGMdiep v5.0 subsurface model (TNO DINOloket website) shows a roughly NW/SE strike in the area of well JUT-01 with SW dip direction.
3. The three proposed solutions do not require unrealistic structural dip-angles (i.e. they do not exceed 17°).

Some uncertainty remains where azimuths of aeolian cross-bed foresets have azimuths not aligning with south-westerly directions.

6.2 Petrographic Sample Preparation

The sampling strategy for thin sections follows to represent every lithofacies described per well. (B)SEM and XRD subsets samples were selected after the inspection of the thin sections at the microscope. From the greater group, some samples were selected to ensure the highly detailed characterization of important aspects regarding reservoir quality. EBN criteria were also included when selecting the samples. When doubt about the certain time of occurrence of any mineral phase, question mark was added.

For optical microscopy: rock samples were impregnated with blue-dyed epoxy resin to aid the identification of porosity. Thin sections were half stained with Alizarin Red S/potassium ferricyanide for carbonate discrimination.

Adams and MacKenzie (1998) give the following staining results:

Mineral	**Stain color with Alizarin Red S**	**Stain color with Potassium ferricyanide**	**Combined Result**
Non-ferroan calcite	pink to red-brown	none	pink to red-brown
Ferroan calcite	pink to red-brown	pale to deep blue depending on iron content	mauve to blue
Non-ferroan dolomite	none	none	unstained
Ferroan dolomite	none	very pale blue	very pale blue (appears turquoise or greenish in thin-section

Table 6-2: Effects of staining methods on carbonate minerals.

For Scanning Electron Microscopy (SEM): selected samples were prepared from rough cubes of core plug trim material (approximately 125 mm^3), and were glued onto aluminium stubs. The mounted stubs were then coated with gold using a JEOL Cressington JFC-1200 Fine Coater. The samples were examined using a JEOL 6010LV Scanning Electron Microscope with Oxford Instruments AztecOne EDS system for mineral identification.

For Backscattered Scanning Electron Microscopy (BSEM): the block from which the thin-section was made of the selected samples were double polished in order to obtain an even and smooth surface. Then the polished blocks were coated with carbon using a JEOL JEC-530 Auto Carbon Coater, to ensure electron conductivity.

For the whole rock X-ray Diffraction (XRD): a portion of each selected sample was ground to a powder in a mill (using acetone to minimize structural grinding damage). The resulting slurry was dried and the powder packed firmly into a back-loading powder mount.

For the clay fraction X-ray Diffraction (XRD): each sample was lightly crushed and mixed with a small amount of distilled water and a 1 ml peptisation solution ($Na_7P_2O_7$ + Na_2CO_3). The samples were placed in an ultrasonic bath for 20 minutes to release the maximum amount of clay into suspension. After settling of the larger than 4 µm fraction, the clay suspension was decanted off and then centrifuged to deposit the entire smaller than 2 µm fraction. This fraction was once again washed three times with distilled water by centrifugation and decanting. The cleaned clay fraction was then mixed with a small amount of distilled water to make a thick slurry and applied onto a glass tile. The glass tile was then left to dry at room temperature for a minimum of 16 hours.

6.3 Paragenetic Sequence Diagram

The diagenetic history of each well is shown in a diagram that reads as follows: from left to right, the time is relatively indicated (from early to late). This intends to cover from eodiagenesis to mesodiagenesis (possible effects of telodiagenesis have not been unequivocally identified in this study). Colours indicate the negative influence on reservoir quality: Green = minor, Yellow = moderate, Red = significant.

6.4 Qualitative Description of Thin-section Samples

Descriptive terms used throughout this study are listed below.

Mineralogy (%)		Porosity (%)		Permeability (mD)	
tr	Very rare	tr	Very poor	<0.01	Very poor
<1	Rare	<1	Poor	0.01 - 0.1	Poor
1-2	Very sparse	1-2	Very low	0.1 - 1	Very low
2-5	Sparse	2-5	Low	1 - 10	Low
5-10	Common	5-10	Fair	10 - 100	Fair
10-20	Abundant	10-20	High	100 - 1000	Good
20-50	Very abundant	20-30	Very high	1000-5000	Very good
>50	Dominant	>30	Extremely high	>5000	Extremely good

Table 6-3: Thin-section description terminology.

Crystal-Size Terminology (after Folk, 1962)	
Extremely coarsely crystalline	>4mm
Very coarsely crystalline	1-4mm
Coarsely crystalline	250-1000µm
Medium crystalline	62-250µm
Finely crystalline	16-62µm
Very finely crystalline	4-16µm
Aphanocrystalline or cryptocrystalline	1-4µm

Table 6-4 Crystal-size terminology.

Pore Connectivity	
No pore interconnections observed	very poor
Some pores are interconnected	poor
Pores commonly show interconnections	moderate
Most pores show interconnections	good
Most pores show several interconnections	very good

Table 6-5: Pore connectivity terminology.

6.5 Quantitative Petrographic Analysis by Point Counting

Quantifying the mineralogical composition is achieved by counting 300 points using a mechanical interval displacer connected to a counting machine. The interval displacer is screwed to the rotating stage of the microscope, and the thin-section is clamped into the displacer. By pressing a master key, the thin-section is moved a given distance along a transverse and the spot under the cross-hair is identified and counted. These distances are adjusted according to the grain-size of the sample. Based on their modal detrital composition quantified by point counting, the siliciclastic samples with <75% detrital matrix (<30µm) are

classified using the sandstone classification scheme of Pettijohn (1975) shown in Figure 6-8. Most samples are arenitic (i.e. <15% detrital matrix).

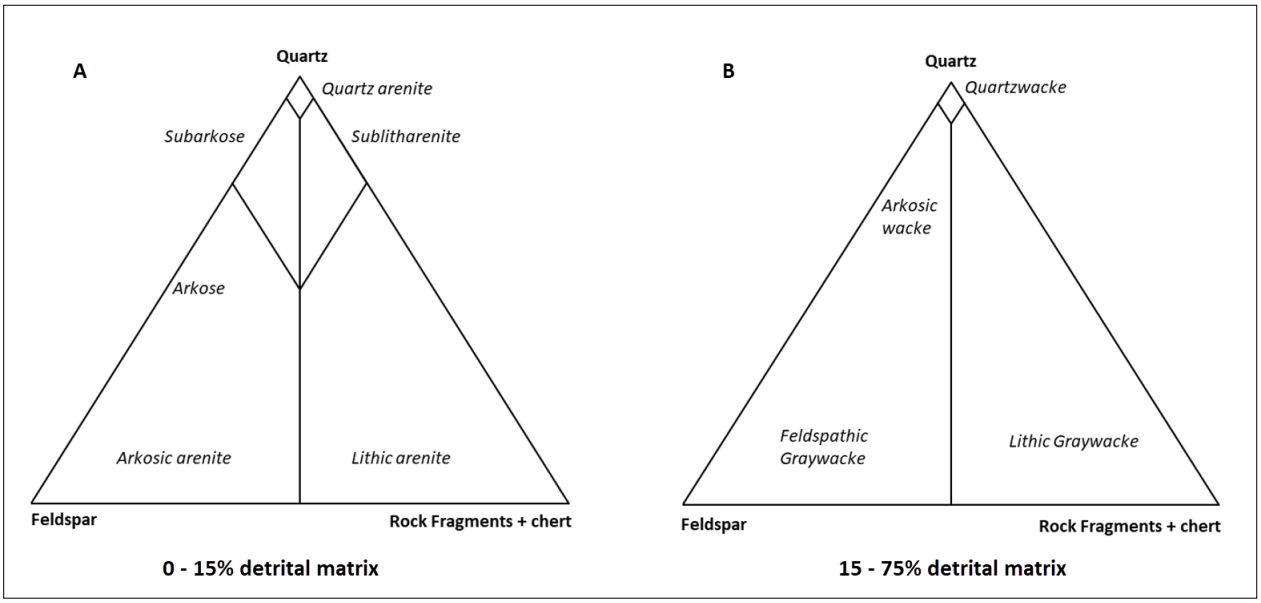

Figure 6-8 Sandstone classification after Pettijohn (1975) for sandstone with < 15% detrital matrix (A) and 15 – 75% detrital matrix (B).

6.5.1 Compactional Porosity Loss (COPL) versus Cementational Porosity Loss (CEPL)

PanTerra Geoconsultants uses a method to calculate porosity loss attributable to compaction and cementation based on a method proposed by Lundergard (1992). In his method, the relative contributions from compaction and cementation to porosity loss are calculated from the initial, or depositional, porosity (P_i,) and two petrographically determined parameters, total optical porosity (P_o), and volume-percent pore-filling cement (PF). The sum of P_o and PF is equal to the so-called minus-cement porosity (P_{mc}) or intergranular volume. This method accounts for the reduction in sediment bulk volume by compaction.

The COPL and CEPL indices are cross-plotted in a diagram showing the relative contributions of compaction and cementation and the remaining pore space. The formula proposed to calculate the COPL is:

$$COPL = P_i - (((100-P_i)*P_{mc})/(100 - P_{mc}))$$

where P_i is the depositional or original porosity. In Lundegard (1992), it is assumed to be 45%. P_{mc} stands for the intergranular volume, which in this case equals the remaining intergranular porosity (P_o) plus the sum of all cements (PF) occupying intergranular (primary) pores.

Cementational porosity loss or CEPL is calculated as:

$$CEPL = (P_i - COPL)*(PF/P_{mc})$$

where PF stands for the sum of all cements occupying intergranular pores.

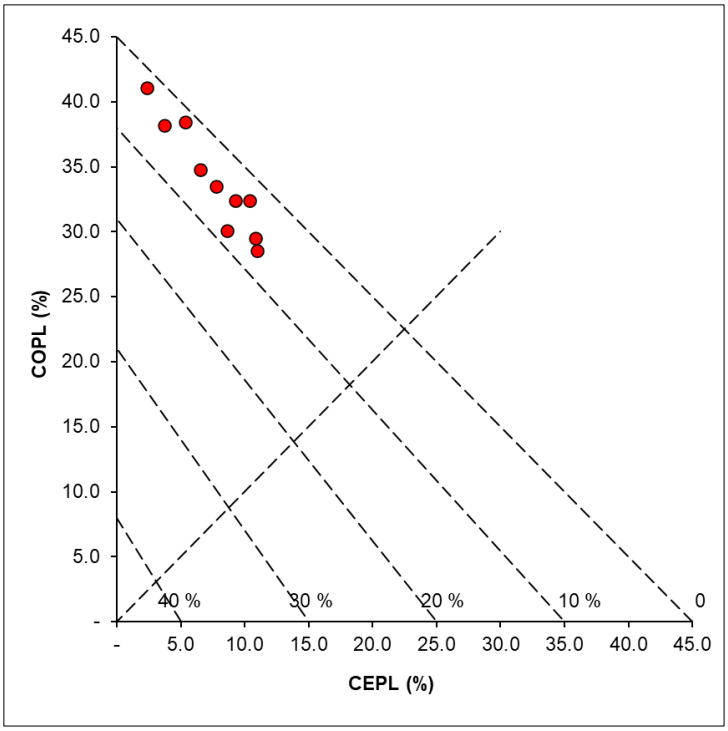

Figure 6-9 **Example of a COPL-CEPL cross plot from Well HEW-01. It shows that the initial (intergranular) porosity of 45% was reduced by absolute values between ca. 28% and 41% (mean 33.9%) by compaction alone. Cementation of intergranular pores was responsible for intergranular porosity reduction of 3% to 11% (mean 7.6%). The diagonal lines show the remaining intergranular porosity, which varies between 2.7% and 9%. Total visible porosity is higher when secondary pores are present.**

This approach is generally accepted as a good indicator of the main post-depositional processes ruling reservoir properties, although several caveats are posed regarding the original assumptions/clauses:

Lundegard (1992) lists several factors that may influence the results:

- The initial pore volume of sand is generally uncertain. If the assumed value is too high, the compactional porosity loss will also be too high by an amount roughly equal to the error in the assumed value. Lundegard (1992) reports values from studies by several authors ranging between 39% to 49%, depending on the depositional settings (e.g., river, beach, dune).
- Compactional porosity loss will be underestimated if grain volume is not constant during diagenesis. Inconstancy of grain volume can occur through net porosity enhancement by grain dissolution or by grain dissolution and local re-precipitation of cement. Lundegard (1992) states that the analysis provides a conservative estimate of compactional porosity loss in sandstones.
- The database used is weighted towards sandstones of Cenozoic age. However, because sandstone compaction is irreversible, some conclusions will be applicable to older sandstones. For example, the conclusions should still apply to the first cycle of burial of older sandstones.
- Grain dissolution, whether resulting in local porosity enhancement by export in solution of former grain mass or local precipitation of authigenic cement, will cause an underestimation of the significance of compaction. PanTerra addresses this by only including point-counted intergranular cements and intergranular pores in the calculation of “minus cement porosity” (Pmc).
- Distinction between pore-filling cement and replacive authigenic minerals (i.e., authigenic minerals that precipitated in secondary pores that initially represented detrital grains) may be challenging when

both are pervasive. Under- or overestimating will directly impact the calculation of the intergranular volume and, consequently, compactional porosity loss.

- Porosity determination by point-counting generally overlooks micro-pores that are too small to be recognized under the microscope. This may underestimate the amount of intergranular volume (P_{mc}), so it overestimates the effect of COPL.

The effects of these uncertainties on the calculations of compactional versus cementational porosity loss on samples from the Slochteren Formation could not be fully evaluated. The calculated COPL values range from 22% to 36% and correlate poorly with measured porosity and permeability. This may be related to the complex burial history, uncertainty about the mass transfer of mineral phases in and out of the Slochteren Formation, and challenges in correctly identifying whether cements are pore-filling or replacive. To some extent, the same holds for discriminating between primary and secondary pores, especially where oversized pores are involved (i.e., pores that originate from the amalgamation of intergranular pores with secondary pores).

6.6 Scanning Electron Microscopy (SEM/BSEM)

SEM: The secondary electrons (SE) that are scattered back from the surface are used to visualize in 3D the morphology and textural relationship of minerals (detrital and diagenetic) and pores in the sample.

BSEM: The samples were examined using a JEOL 6010LV Scanning Electron Microscope fitted with an Oxford Instruments AztecOne EDS system for element and mineral identification within the sample. For BSEM analysis, the brightness of a mineral is directly proportional to the mean atomic number (or Z-value). The variation in grey scales between minerals in a BSEM image can thus be used for mineral distinction based on image analyses. The higher the atomic numbers of the mineral, the brighter it will be in the image. It also allows to visualize the textural relationship of minerals (detrital and diagenetic) and pores in the sample in 2D.

6.7 X-ray Diffraction (XRD)

The samples were scanned on a PANalytical CubixPro automated X-ray diffractometer using Ni-filtered CuKa radiation. The powder samples were scanned at a rate of 4 seconds per 0.02° step width, using 0.2mm slits from 5 to 70° 2 ϑ.

The qualitative XRD analysis of a mineral composition is based on the identification of the main or primary peaks of the relevant mineral. Every mineral is characterized by a specific pattern of peaks (primary, secondary, and peaks of higher order) in an XRD spectrum, which allows the identification and differentiation from other components of the sample. Generally, primary peaks are the strongest peaks in a XRD spectrum and are used to identify and quantify minerals.

The quantification of a specific mineral is based on the integration of the area below of its characteristic peaks. The resulting value is multiplied by a calibration factor, the so-called Reference Intensity Ratio (= RIR factor). This calibration factor is mineral-dependant and is usually determined by preparing a 50:50 mixture of the pure mineral with a reference mineral (PanTerra uses corundum as reference mineral). The RIR factor is then the ratio of the main peak of the mineral phase and the main peak of corundum. This approach allows the quantification of (crystalline) mineral phases of a sample. The RIR factors for each identified mineral are applied to the peak areas of each identified mineral. The numbers so derived can be considered as the (normalized) relative contributions of each mineral to the XRD spectrum. By summing up of these relative contributions and dividing each contribution by the sum of the total contribution, the

relative quantity of each mineral (by weight) is calculated as a fraction of 1 (in percentages). In some cases, the quantification may not be reliable due to: an unknown RIR value (e.g., dawsonite); impossibility of effective separation of some mineral phases (e.g., dickite in the clay fraction). Minerals present in less than 0.5% weight are reported as traces (Tr).

6.8 Analysis of Reservoir Quality from Legacy Routine Core Analysis Data

Legacy routine core analysis data (RCA) comprising helium porosity, horizontal permeability and grain density results measured on core plug samples were analysed for most wells. A total of 2200 measurements from 28 wells were available. For each well report, the data were cross-plotted (He-porosity vs horizontal permeability and He-porosity vs grain density) and summarised in a table listing sample count and mean values for porosity, permeability and grain density. The geometric mean (Kh_{mean}) was calculated for permeability, while the other two entities were arithmetically averaged. The Kh_{mean} is obtained by calculating the mean of the log2 values of all permeabilities in a data set. This value is subsequently squared. Likewise, the standard deviation (St.Dev[10]) was calculated on the log2 permeability values and added and subtracted from mean of log2 permeabilities. The two resulting values were then squared. The permeability data (Kh) for well SLB-01 are given as an example below:

Well SLB-01	Log2 Kh	Kh (mD)
Mean	7.12	139
St.Dev	1.71	-
Mean - St.Dev	5.41	42.5
Mean + St.Dev	8.83	453

In addition to cross-plots, depth plots of porosity, permeability and grain density were created for several wells to illustrate vertical trends in reservoir quality data. Figure 6-10 shows an example of a depth plot included in the well report for SLD-03.

[10] Note: The standard deviation was not calculated for data populations with less than 10 samples

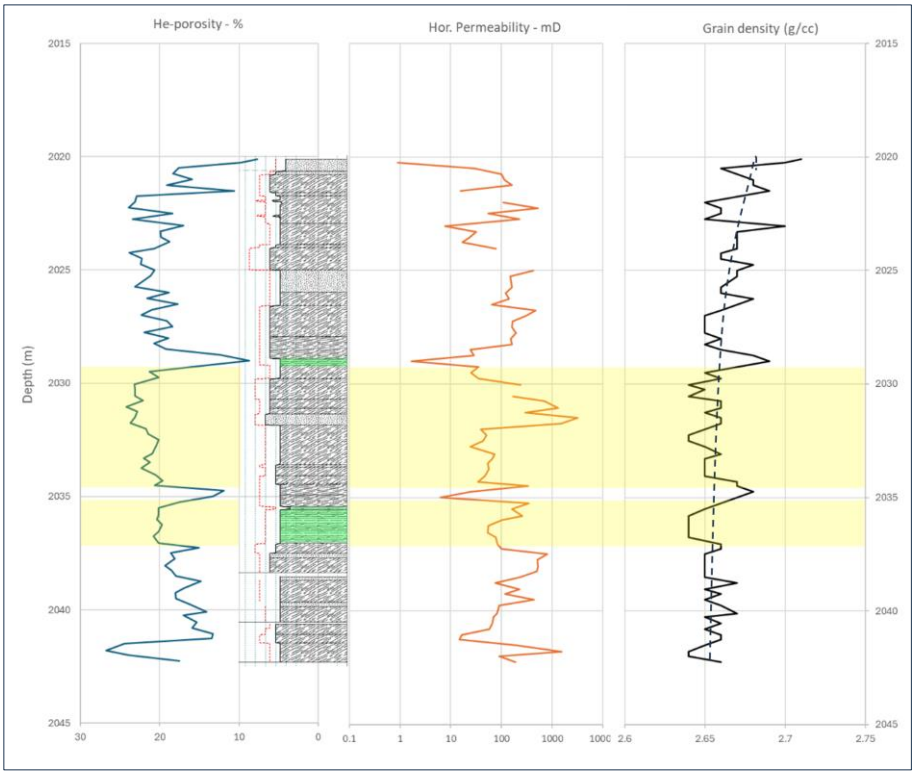

Figure 6-10 **Porosity, permeability and grain density plotted against legacy RCA plug depths in well SLD-03. A diagram of the core description is inserted between the He-porosity and horizontal permeability curves, showing intervals with horizontal lamination (light green) and low to high-angle cross-lamination (not coloured). The yellow shaded bands represent intervals with relatively uniform porosity values, but more variable permeabilities. Grain densities gradually increase up-section, possibly representing the influence of the overlying Zechstein Formation on diagenesis.**

7 Appendices

7.1 List of single well reports

To be found on TNO NLOG web site: https://www.nlog.nl/datacenter/brh-overview

page: Datacenter/Gegevenstypen/Boringen NLOG website under the tab “Documenten”

1.	ZEW-01 final report & WellCAD panel.pdf
2.	BLA-01-S1 final report & WellCAD panel.pdf
3.	WEP-01 final report & WellCAD panel.pdf
4.	JPE-01 final report & WellCAD panel.pdf
5.	WSP-01 final report & WellCAD panel.pdf
6.	WRV-01 final report & WellCAD panel.pdf
7.	DRO-01 final report & WellCAD panel.pdf
8.	EMO-01 final report & WellCAD panel.pdf
9.	WGF-01 final report & WellCAD panel.pdf
10.	KAM-01-S1 final report & WellCAD panel.pdf
11.	EPE-01 final report & WellCAD panel.pdf
12.	SLD-03 final report & WellCAD panel.pdf
13.	IJD-01 final report & WellCAD panel.pdf
14.	BNV-01-S1 final report & WellCAD panel.pdf
15.	LSM-01 final report & WellCAD panel.pdf
16.	OZN-01 final report & WellCAD panel.pdf
17.	EVD-01 final report & WellCAD panel.pdf
18.	JUT-01 final report & WellCAD panel.pdf
19.	ZWK-01 final report & WellCAD panel.pdf
20.	HEW-01-S1 final report & WellCAD panel.pdf
21.	MID-302.1 final report & WellCAD panel.pdf
22.	MID-103-S1 final report & WellCAD panel.pdf
23.	HES-01 final report & WellCAD panel.pdf
24.	WYH-01 final report & WellCAD panel.pdf
25.	LNH-01 final report & WellCAD panel.pdf
26.	HLE-01 final report & WellCAD panel.pdf
27.	MKN-01 final report & WellCAD panel.pdf
28.	SLB-01 final report & WellCAD panel.pdf
29.	ERM-01-S1 final report & WellCAD panel.pdf
30.	DSP-02 final report & WellCAD panel.pdf
31.	Q14-02 final report & WellCAD panel.pdf
32.	HST-02-S1 final report & WellCAD panel.pdf
33.	WAS-23-S2 final report & WellCAD panel.pdf
34.	DSP-01 final report & WellCAD panel.pdf

7.2 List of petrographic analyses performed

Order	Well	Depth (m)	THS	SEM	BSEM	XRD
1	ZEW-01	1624.75	X	-	-	-
2	ZEW-01	1627.95	X	-	-	-
3	ZEW-01	1631.40	X	n.p.	X	-
4	ZEW-01	1635.95	X	-	-	-
5	BLA-01-S1	1511.11	X	-	-	-
6	BLA-01-S1	1516.55	X	n.p.	X	-
7	BLA-01-S1	1519.02	X	-	-	-
8	WEP-01	1544.49	X	-	-	-
9	WEP-01	1547.55	X	-	X	-
10	WEP-01	1592.36	X	X	-	X
11	WEP-01	1595.15	X	-	-	-
12	JPE-01	901.50	X	-	-	X
13	JPE-01	904.70	X	-	X	-
14	JPE-01	908.45	X	-	-	-
15	JPE-01	911.82	X	-	-	X
16	JPE-01	915.15	X	X	-	-
17	WSP-01	2193.50	X	-	X	-
18	WRV-01	2347.95	X	X	X	X
19	DRO-01	2191.95	X	-	-	-
20	DRO-01	2199.40	X	-	-	-
21	DRO-01	2200.45	X	-	-	-
22	DRO-01	2209.45	X	-	-	X
23	DRO-01	2214.50	X	X	-	-
24	DRO-01	2220.00	X	-	X	-
25	DRO-01	2225.95	X	-	-	-
26	DRO-01	2228.30	X	-	-	X
27	DRO-01	2235.85	X	-	-	-
28	EMO-01	1680.40	X	-	-	-
29	EMO-01	1683.80	X	-	X	-
30	EMO-01	1685.50	X	-	-	-
31	EMO-01	1691.50	X	-	-	-
32	EMO-01	1694.25	X	-	-	X
33	EMO-01	1702.20	X	X	-	-
34	EMO-01	1706.90	X	-	-	X
35	WGF-01	2267.20	X	-	-	-
36	WGF-01	2270.75	X	-	-	X
37	WGF-01	2272.75	X	-	-	-
38	WGF-01	2274.65	X	X	-	-
39	WGF-01	2276.60	X	-	X	-
40	WGF-01	2277.80	X	-	-	X
41	KAM-01-S1	1812.40	X	-	-	X
42	KAM-01-S1	1815.24	X	X	-	-
43	KAM-01-S1	1819.25	X	-	X	-
44	KAM-01-S1	1822.05	X	-	-	-

Order	Well	Depth (m)	THS	SEM	BSEM	XRD
45	KAM-01-S1	1826.40	X	-	-	X
46	EPE-01	1814.70	X	X	X	X
47	SLD-03	2020.50	X	-	X	X
48	SLD-03	2030.20	X	X	-	X
49	SLD-03	2034.60	X	-	-	-
50	IJD-01	2269.60	X	X	X	-
51	IJD-01	2271.65	X	-	-	X
52	IJD-01	2274.30	X	-	-	-
53	IJD-01	2279.35	X	-	-	-
54	IJD-01	2281.75	X	-	-	-
55	IJD-01	2284.05	X	-	-	X
56	BNV-01-S1	3039.30	X	-	X	-
57	LSM-01	1497.60	X	X	X	X
58	LSM-01	1509.30	X	-	-	-
59	OZN-01	1311.77	X	-	-	X
60	OZN-01	1313.65	X	X	-	-
61	OZN-01	1315.72	X	-	-	-
62	OZN-01	1365.30	X	-	-	X
63	OZN-01	1370.38	X	-	-	-
64	EVD-01	1802.30	X	-	-	X
65	EVD-01	1809.50	X	-	X	-
66	EVD-01	1811.50	X	-	-	X
67	EVD-01	1814.00	X	X	-	-
68	EVD-01	1821.00	X	-	-	X
69	EVD-01	1824.50	X	X	-	X
70	EVD-01	1828.00	X	-	-	-
71	EVD-01	1833.00	X	X	-	X
72	EVD-01	1836.00	X	-	-	-
73	EVD-01	1841.50	X	-	X	X
74	EVD-01	1843.00	X	-	-	-
75	JUT-01	3259.00	X	-	-	X
76	JUT-01	3260.80	X	-	-	-
77	JUT-01	3266.50	X	-	-	X
78	JUT-01	3268.00	X	X	-	-
79	JUT-01	3273.60	X	-	-	X
80	ZWK-01	3181.30	X	-	-	X
81	ZWK-01	3190.30	X	-	-	-
82	ZWK-01	3191.70	X	-	-	-
83	ZWK-01	3194.30	X	-	-	-
84	ZWK-01	3197.30	X	X	-	-
85	HEW-01-S1	2009.50	X	-	-	-
86	HEW-01-S1	2036.60	X	-	-	-
87	HEW-01-S1	2050.10	X	-	-	X
88	HEW-01-S1	2063.40	X	-	-	-
89	HEW-01-S1	2068.40	X	X	-	X
90	HEW-01-S1	2078.20	X	-	-	-
91	HEW-01-S1	2111.50	X	-	-	-

Order	Well	Depth (m)	THS	SEM	BSEM	XRD
92	HEW-01-S1	2119.50	X	-	-	X
93	HEW-01-S1	2147.00	X	-	-	-
94	HEW-01-S1	2171.00	X	-	-	-
95	MID-302	3502.35	X	-	-	-
96	MID-302	3610.05	X	-	-	-
97	MID-302	3613.70	X	-	-	-
98	MID-302	3615.40	X	X	-	X
99	MID-103-S1	2577.40	X	-	-	-
100	MID-103-S1	2607.40	X	-	-	-
101	MID-103-S1	2623.60	X	X	-	-
102	MID-103-S1	2628.40	X	-	-	X
103	MID-103-S1	2646.40	X	X	-	-
104	MID-103-S1	2655.50	X	-	-	-
105	MID-103-S1	2664.80	X	-	-	X
106	MID-103-S1	2666.30	X	-	-	-
107	HES-01	2103.50	X	X	-	X
108	WYH-01	1723.30	X	-	-	-
109	WYH-01	1724.50	X	-	-	X
110	WYH-01	1728.10	X	-	-	-
111	WYH-01	1735.50	X	-	-	-
112	WYH-01	1739.70	X	X	-	X
113	WYH-01	1743.60	X	-	-	-
114	WYH-01	1748.40	X	-	-	X
115	WYH-01	1752.00	X	-	-	-
116	WYH-01	1754.50	X	X	-	X
117	WYH-01	1755.90	X	-	-	-
118	WYH-01	1758.90	X	-	-	-
119	WYH-01	1759.70	X	-	-	-
120	WYH-01	1762.40	X	-	-	X
121	LNH-01	2296.90	X	X	-	X
122	LNH-01	2299.00	X	-	X	-
123	LNH-01	2306.00	X	-	-	X
124	HLE-01	1420.80	X	-	-	X
125	HLE-01	1424.40	X	-	-	-
126	HLE-01	1428.50	X	X	-	X
127	HLE-01	1431.30	X	-	-	-
128	HLE-01	1431.60	X	-	-	-
129	HLE-01	1432.40	X	X	-	X
130	MKN-01	1698.50	X	X	-	X
131	MKN-01	1702.30	X	-	X	X
132	MKN-01	1705.20	X	-	-	-
133	SLB-01	2011.20	X	X	-	X
134	SLB-01	2016.00	X	-	-	-
135	SLB-01	2017.80	X	-	-	-
136	SLB-01	2021.70	X	-	-	X
137	ERM-01-S1	2641.70	X	-	-	-
138	ERM-01-S1	2644.10	X	X	-	X

Order	Well	Depth (m)	THS	SEM	BSEM	XRD
139	DSP-02	n/a	-	-	-	-
140	Q14-02	2933.75	X	X	-	-
141	Q14-02	2946.75	X	-	X	X
142	Q14-02	2952.00	X	-	-	X
143	HST-02-S1	2393.20	X	-	-	-
144	HST-02-S1	2398.30	X	-	-	-
145	HST-02-S1	2401.00	X	-	-	X
146	HST-02-S1	2402.80	X	-	-	-
147	WAS-23-S2	3012.30	X	-	-	-
148	WAS-23-S2	3019.22	X	-	-	-
149	WAS-23-S2	3023.05	X	-	-	-
150	WAS-23-S2	3035.62	X	-	-	-
151	WAS-23-S2	3041.96	X	X	-	-
152	WAS-23-S2	3047.60	X	-	-	-
153	WAS-23-S2	3050.30	X	-	-	X
154	DSP-01	2271.20	X	-	-	-
155	DSP-01	2282.40	X	-	-	-
156	DSP-01	2305.30	X	-	-	X
157	DSP-01	2310.80	X	-	-	-
158	DSP-01	2317.30	X	-	-	-
159	DSP-01	2325.80	X	-	-	-
160	DSP-01	2339.30	X	-	-	-
161	DSP-01	2348.60	X	-	-	-
162	DSP-01	2358.50	X	-	-	X
163	DSP-01	2362.40	X	X	-	-